2-2013

Pattern Formation in Floating Sheets

Hunter King
University of Massachusetts Amherst, avcikral@gmail.com

PATTERN FORMATION IN FLOATING SHEETS

A Dissertation Presented

by

HUNTER KING

Submitted to the Graduate School of the
University of Massachusetts Amherst in partial fulfillment
of the requirements for the degree of

DOCTOR OF PHILOSOPHY

February, 2013

Physics

PATTERN FORMATION IN FLOATING SHEETS

A Dissertation Presented

by

HUNTER KING

Approved as to style and content by:

N. Menon, Chair

B. Davidovitch, Member

A. D. Dinsmore, Member

T. P. Russell, Member

D. Candela, Department Chair
Physics

ACKNOWLEDGMENTS

There are too many people to thank in the local, cooperative scientific community that I have lived in for the past few years.

I have received crucial help with experimental and computational techniques from Bugra Toga, Peiwen Zhang, Jiangshui Huang, Greg Farrell and Dominique Cambou. For constant inspiring science conversation I should thank Jiansheng Feng, Colm Kelleher, and Don Blair. I would like to thank Lee Walsh, Sereres Johnston, Craig Versek, and Nesrin Senbil for supporting the active and cooperative student community that has kept me engaged and motivated.

Input from Robert Schroll and Prof. Davidovitch has given much form and direction to the main project in this thesis. Without their theoretical support, this work would be much less interesting. I would also like to thank the rest of the committee, Prof. Dinsmore and Prof. Russell, for their attention and for providing useful feedback.

Most importantly, I should thank Prof. Menon for the thoughtful guidance in research, patience, valuable mentoring, and being a good role model.

In a broader sense, I thank my father for giving me confidence, my mother for teaching perseverance by example, and my wife for putting up with me on a daily basis.

ABSTRACT

PATTERN FORMATION IN FLOATING SHEETS

FEBRUARY, 2013

HUNTER KING

B.Sc., UNIVERSITY OF MASSACHUSETTS AMHERST

M.Sc., BOGAZICI UNIVERSITY

Ph.D., UNIVERSITY OF MASSACHUSETTS AMHERST

Directed by: Professor N. Menon

This thesis presents a study of two basic modes of deformation of a thin sheet: wrinkling and crumpling, viewed primarily in the context of an elastic sheet confined by capillary forces on a drop of liquid.

First, it provides a brief conceptual background in the relevant physics of thin sheet mechanics and capillarity and introduces the general principles of wrinkling and crumpling.

The problem of confining a circular sheet on an increasingly curved spherical drop is presented as a vehicle to explore these principles. At finite curvature, the sheet is seen to wrinkle around its outer edge. At large confinement, characteristic features of crumpling gradually dominate the pattern. The experimental observations in both regimes are analyzed separately.

Analysis of images of the sheet in the wrinkled regime yield data for the number and length of the wrinkled zone, as a function of the experimental control parameter, the pressure. The length of the wrinkles is correctly described by a far-from-threshold theory, which describes a limiting regime in thin-sheet mechanics, distinguished by high 'bendability'. The validity of this theory is verified by the data for highly bendable, ultrathin sheets for the first time. The theory is based on the assumption that the wrinkles completely relax compressive stresses and therefore preserve the cylindrical symmetry of the stress field.

The emergence of crumpling from the wrinkled shape is explored via evolution of visible features in the sheet as well as gaussian curvature measurements obtained by analyzing height maps from optical profilometry. The emergence of several length scales, increasing asymmetry in curvature distribution, the failure of wrinkle extent prediction and formation of d-cones associated with crumpling are all measured to locate the transition to a crumpled state. The value of gaussian curvature at the center of the sheet appears to follow the cylindrically symmetric prediction over the whole range of the experiment, suggesting that the onset of crumpling events does not affect the global shape of the sheet.

Finally, analogous wrinkling and crumpling behavior of particle-laden interfaces is discussed. The spontaneous formation of conical defects in a curved 2D crystal is compared to the crumpling of a sheet on a drop, and insight from thin sheet mechanics is applied to the mysterious wrinkling of particle rafts. Some future directions for measuring wrinkling of sheets on negative curvature surfaces and deformations of fluid interfaces are proposed.

TABLE OF CONTENTS

LIST OF FIGURES

Figure **Page**

INTRODUCTION

It doesn't take long to get from first principles in continuum mechanics and geometry to problems that display richness and diversity while confounding intuition. Systems composed of more than one material component, in pitting basic driving forces of their constituents against each other, can create situations where even the qualitative behavior is unexpected, and sometimes pretty. Presented in this thesis are a couple of examples of such systems which display common themes of geometric frustration and pattern formation driven by the physical forces of elasticity and capillarity.

The subject of focus is an elastic sheet which is subjected to the capillary forces of a liquid drop and undergoes two independent buckling transitions between three distinct states: axisymmetric, wrinkled, and crumpled. These are studied experimentally and compared to theoretical predictions, leading to important general conclusions regarding post-buckling analysis and stress focusing of thin sheets. This thesis will try to express an understanding of how a thin sheet chooses to assume one or another shape in response to external confinement. To this end, we will first review the basic physical principles of thin-sheet mechanics and capillarity, such that the student or non-expert can understand at least conceptually without outside reference. Then, we will present the ubiquitous concepts of buckling, wrinkling and crumpling in more specific terms so as to address them individually and unambiguously when our experiment and results are discussed. Additionally, the basic themes will be revisited with reference to a related and interesting physical system: the particle-laden interface.

CHAPTER 1

BACKGROUND

1.1 Elasticity of Thin Sheets

A solid body is characterized by its tendency to resist changing its shapes under external forcing. All solids respond elastically when small forces are applied, meaning that the initial shape is exactly recovered when the external force is removed, like an ideal spring. In this regime of reversible deformation, elasticity theory begins with the assumption that solids pay an energetic price for moving their material elements with respect to each other in changing their shape. Each material element has a reference location (collectively a metric), defined with respect to its neighbors. Deformation from the reference metric is represented as a strain tensor ϵ, with elements u_{ij}:

$$u_{ij} = \frac{1}{2}\left(\frac{\partial u_i}{\partial x_j} + \frac{\partial u_j}{\partial x_i}\right) \tag{1.1}$$

in terms of the displacement vector u, which points from the initial to deformed position of a material element[1]. The derivatives express the fact that strain cares about *relative* displacement in the material, and not translation. The strain is also invariant to rigid rotations for the same reason.

The most general quadratic form to express energy per unit volume, U, a scalar, resulting from a tensor (while respecting the symmetries of a homogeneous, isotropic

[1]The strain also contains a non-linear term $\frac{\partial u_l}{\partial x_i}\frac{\partial u_l}{\partial x_j}$, which is neglected due to its higher order in small-strain linear elasticity.

material) is by the squared sum of its diagonal components and the sum of the squares of all its components [24]:

$$U = \frac{1}{2}\lambda Tr(\epsilon)^2 + \mu Tr(\epsilon^2) \tag{1.2}$$

where λ and μ are the "Lamé" coefficients. It is important to note that exactly two terms appear in the general expression. This means that the two Lamé coefficients convey all of the material properties in this model, dividing energy into separate shear and compression components. Just as the strain tensor indicates the local displacement of a material element with respect to its neighboring elements, the stress tensor, σ indicates the corresponding force (per area) on the surfaces of the element due to interaction with neighboring elements. Its diagonal terms are pressures and off-diagonal terms are shears.

Redefining material terms without gaining or losing information:

$$2\mu + \lambda - \frac{\lambda^2}{\mu + \lambda} \equiv E \tag{1.3}$$

$$\frac{\lambda}{2(\mu + \lambda)} \equiv \nu \tag{1.4}$$

slightly changes the energy expression:

$$U = \frac{E}{2(1+\nu)}\left(u_{ij}^2 + \frac{\nu}{1-2\nu}u_{ll}^2\right) \tag{1.5}$$

but the new material parameters: Young's modulus, E, and Poisson ratio, ν, take on another useful physical meaning, exemplified by the situation in Fig. 1.1. Here, a block of elastic material of length L and width w is compressed between two plates by a uniaxial, uniform pressure P. As a result, it is compressed a distance Δx, and squishes out perpendicularly an amount Δy. E plays the part of a linear spring constant,

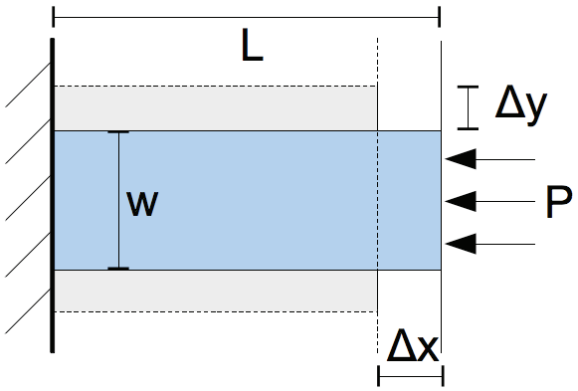

Figure 1.1. Compressed elastic cylinder

determining the compression u_{xx}. ν indicates how well the material preserves its volume, predicting the subsequent perpendicular expansion u_{yy}:

$$u_{xx} = -\frac{\Delta x}{L} = P/E \tag{1.6}$$
$$u_{yy} = \frac{2\Delta y}{w} = -\nu u_{xx} = \nu P/E$$

When a material is thin in one dimension, it is convenient to describe its shape as a 2D surface in 3D space. In this case, in-plane stresses and strains are put on a different footing than those out-of-plane, and the effective elastic moduli are redefined. A 2D Young's modulus, or 'stretching modulus', Y is found by integrating over the thickness, t:

$$Y = Et \tag{1.7}$$

which gives rise to a stretching energy (when pulled or compressed uniformly in one direction by u_{xx}):

$$U_S = \frac{1}{2} Y u_{xx}^2 \tag{1.8}$$

The bending modulus, B, which attributes energy to local curvature, depends on thickness in a more complicated way, as illustrated in Fig. 1.2. The dashed line in the cross section of the thin sheet represents its '2D' position. In order to bend (along

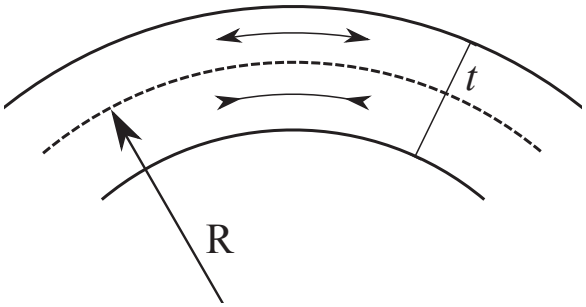

Figure 1.2. Cross-section of a bent sheet

one axis) with the radius R, the material in the top half necessarily stretches and the material in the bottom half necessarily compresses. By integrating the energy of deformation through the thickness of the sheet in this geometry, the coefficient in front of the curvature $\kappa = 1/R$:

$$U_B = \frac{1}{2} B \kappa^2 \tag{1.9}$$

defines a bending modulus, which turns out to be:

$$B = \frac{Et^3}{12(1-\nu^2)} \tag{1.10}$$

for a thin sheet with a radius of curvature $R = \frac{1}{\kappa}$. As before, there are exactly two parameters which express the elastic material properties. The energy expression for a thin sheet is commonly expressed as a functional of in-plane strain u and out-of-plane curvature κ:

$$U = \int (U_B(\kappa) + U_S(\epsilon)) dA \tag{1.11}$$

Two crucial points follow. The first regards the differing dependence on thickness of the two thin-sheet moduli. The consequences are apparent in a simple example of "Euler buckling", to be addressed next. The second concerns a fundamental geometric principle that couples one type of curvature with in-plane stretching, which will be discussed after that.

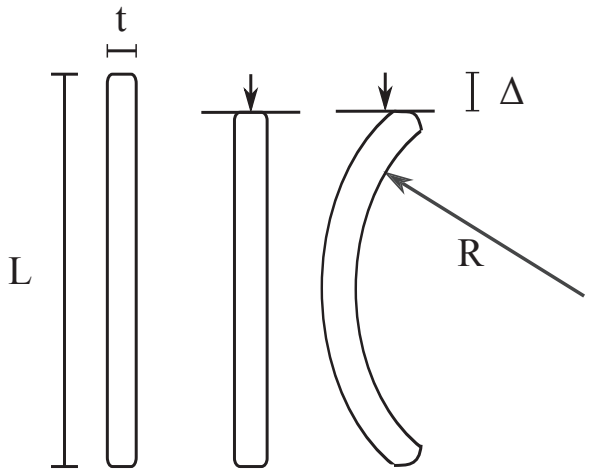

Figure 1.3. A thin sheet confined in one direction, allowed to choose between storing energy by compressing in-plane (middle), or by bending out-of-plane (right).

1.1.1 Buckling

The stretching modulus, Y, is proportional to sheet thickness, t. The bending modulus, B, is proportional to t^3. We should then expect that if the sheet is given the option to bend or to stretch, it will show an increasing preference to bend the thinner it is. To see this quantitatively, consider the case in which a thin sheet is uniaxially compressed a distance Δ as in Fig. 1.3. Assume that the ends can rotate but not translate. The extent of the sheet normal to the page, w, plays no role, except for a multiplicative constant in the energies.

If the sheet responds by simply compressing along its slender axis, it will store an energy (per length w):

$$\frac{U_S}{w} = \frac{1}{2} Y u_{xx}^2 = \frac{1}{2} Y \left(\frac{\Delta}{L} \right)^2 \tag{1.12}$$

The sheet also has the option of relieving compression by bending out of plane. The shape of least bending energy is an arc of constant curvature, $1/R$. In the 'inextensible' limit where no in-plane strain remains, the total length L lives on that arc. Assuming $L \ll R$ and expanding to third order in this limit, $R \approx \sqrt{\frac{L^3}{24\Delta}}$. This makes the bending energy:

$$\frac{U_B}{w} = \frac{1}{2}B\kappa^2 = \frac{1}{2}B\left(\frac{1}{R}\right)^2 \approx \frac{1}{2}B\left(\frac{24\Delta}{L^3}\right) \tag{1.13}$$

We can already see from the relative powers of Δ that for very small compression, $U_S \ll U_B$, but that stretching energy quickly dominates at larger compressions. Approaching the crossover of preferred shape solutions from the side of small compression, one should find that the axisymmetric sheet becomes unstable to out-of-plane perturbations, eventually popping out spontaneously to the right or left to minimize its energy. The critical strain can be found by setting equal the bending and stretching energies, giving:

$$u^*_{xx} = \frac{\Delta_c}{L} = \frac{B}{Y}\left(\frac{24}{L^2}\right) \tag{1.14}$$

Buckling occurs above this threshold strain when bending becomes preferable to compressing. Very near threshold, appreciable energy is stored in both forms. Far above the threshold, bending is overwhelmingly preferable, so any stretching can be ignored, and the sheet is 'inextensible' in the compression direction. A similar quantity which expresses nearness to this threshold will be called 'bendability' later. Putting back the thickness dependence for an isotropic material:

$$u^*_{xx} \propto \frac{t^2}{L^2} \tag{1.15}$$

we see explicitly how slenderness leads to a tendency to buckle, as it prefers to bend than compress (or stretch).

1.1.2 Curvature and Strain

Above, we drew pictures of *pure* bending out-of-plane and *pure* stretching in-plane. We can consider these deformations to be geometrically independent. This is not true for bending and stretching in general. Before rethinking this more carefully, it is useful to generally express the local curvature as a tensor in terms of derivatives of the surface $\mathbf{R}$ along the material coordinates s_x, s_y:

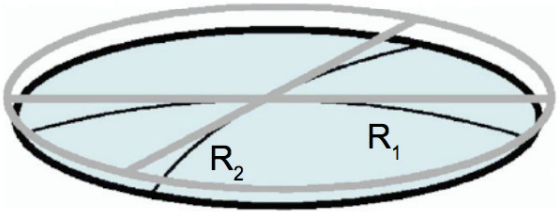

Figure 1.4. A circle on a sheet with gaussian curvature [40]

$$C = \begin{pmatrix} \frac{d^2\mathbf{R}}{ds_x^2} & \frac{d^2\mathbf{R}}{ds_y ds_x} \\ \frac{d^2\mathbf{R}}{ds_y ds_x} & \frac{d^2\mathbf{R}}{ds_y^2} \end{pmatrix} \rightarrow \begin{pmatrix} \kappa_1 = \frac{1}{R_1} & 0 \\ 0 & \kappa_2 = \frac{1}{R_2} \end{pmatrix} \tag{1.16}$$

Diagonalizing this tensor rotates the coordinate system so that the diagonal terms are the orthogonal 'principal curvatures' κ_1 and κ_2, which are maximum and minimum values. The curvature can be generally characterized by its trace and determinant:

$$\kappa = \frac{1}{2} TrC = \frac{1}{2}\left(\frac{1}{R_1} + \frac{1}{R_2}\right) \tag{1.17}$$

$$\kappa_G = detC = \frac{1}{R_1 R_2} \tag{1.18}$$

where κ is called the 'mean curvature' and κ_G the "Gaussian curvature".

Consider the situation depicted in Fig. 1.4, where a surface is bent in two orthogonal directions, with radii R_1 and R_2. Diameter and circumference lines drawn on the material before deformation can be compared to those after deformation.

We can see intuitively that the new curved shape cannot be obtained without changing the lengths of either the diameter lines or circumference lines. Doing so means that the material is strained *in-plane*, radially and/or azimuthally. This was not the case before, when the surface was flat in one direction.

This situation demonstrates Gauss' "theorema egregium"[29], which establishes a relationship between in-plane strains and the Gaussian curvature defined above. It says that the Gaussian curvature can be determined without reference to the embed-

ding, or configuration of the sheet in space, but by measuring angles and distances along the surface. Measuring the circumference $< \pi \times (diameter)$ along material coordinates in the above example indicates $G > 0$ and therefore the presence of in-plane strains. A surface is called 'developable' if it is deformed without changing its Gaussian curvature. A sheet deformed by pure bending has only one non-zero principle curvature, so $G = 0$, and it is not required to stretch. It may still do so, as stretching does not conversely require curvature.

Combining two points from above, we see the logical strategy for a thin sheet to accommodate confinement: In order to minimize energy, it will buckle rather than stretch, and in buckling, it will try to avoid Gaussian curvature by remaining locally flat in one direction. This lesson should be intuitive, as it is often applied when eating pizza: to prevent the tip from succumbing to gravity, one bends the slice along the crust. The thin sheet easily buckles in that direction, but in doing so, becomes more resistant to bending in the additional downward direction, because that would, via theorema egregium, require the more costly stretching. The same argument pertains to the bending stiffness of tape measures, corrugated sheet metal, etc.

At this point, it is possible to introduce in specific terms what we will mean by 'wrinkling' and 'crumpling'.

1.1.3 What we will mean by 'wrinkling'

The formation of smooth rippled patterns we call wrinkles begins when a sheet is loaded along one of its slender directions. The first response of the sheet under compression was already discussed in Sec. 1.1.1. Assuming the load is significantly greater than the buckling threshold, we expect the sheet to store energy in bending only and minimize it by choosing the largest wavelength available, just as in the picture on the right of Fig. 1.3. The important additional element that leads to wrinkling is that another restoring force in the system interferes with this choice of wavelength.

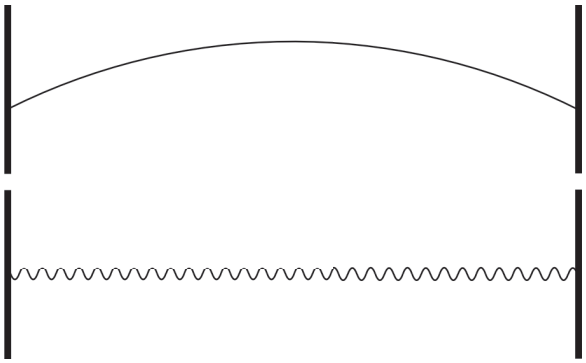

Figure 1.5. Inextensibility requires the horizontal displacement to be completely compensated by out-of-plane deformation. Top: Largest wavelength preferred by bending stiffness. Bottom: Small wavelength preferred by substrate or tension to minimize overall displacement.

This can occur when the sheet is *supported* by a soft substrate, or when it is *under tension* in its perpendicular slender direction. Typically, the restoring force will oppose displacement out of plane (as we will see in the following examples), with the implication that it prefers the smallest possible wavelength. The compromise reached by the substrate and sheet is the wrinkle pattern, characterized by an intermediate, material-dependent wavelength.

A simple example involves an ultrathin polystyrene sheet floating on water, which is viewed from above in Fig. 1.6. Two hard walls confine the sheet to a horizontal extent less than its initial width. It buckles out of plane to relieve compressive stress. Assuming compression is well beyond the buckling threshold, the inextensibility condition constrains the solution to preserve the total length along the compressed direction. Once again, bending prefers a large wavelength to reduce curvature, but now it is forced to compete with the gravitational energy of the water that is displaced under the wrinkle. Gravitational energy is indifferent to curvature, but forbids large vertical displacements. The contrasting solutions are shown in Fig. 1.5. The total energy (per unit area) for small amplitude displacement becomes:

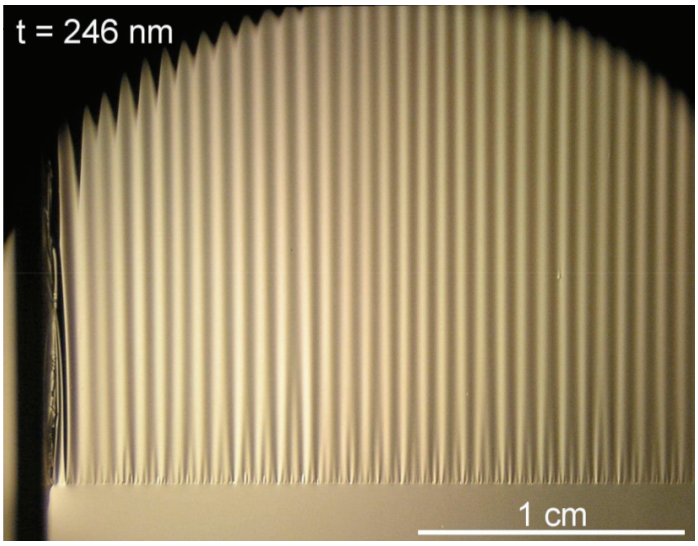

Figure 1.6. Compression of a floating sheet induces a uniform wrinkle pattern.[15]

$$\mathcal{U} = \frac{1}{2}\left(B\left(\frac{\partial^2 h}{\partial y^2}\right)^2 + \rho g h^2\right) \tag{1.19}$$

where h is the height function. Assuming a sinusoidal form for h under the inextensibility condition (that the energetic cost of in-plane compression forbids the length to change) allows us to minimization with respect to wavelength. The result is a compromise of gravity and bending stiffness [15]:

$$\lambda = 2\pi\left(\frac{B}{\rho g}\right)^{1/4} \tag{1.20}$$

Data over a wide range of thicknesses agrees with this predicted wavelength, seen in Fig. 1.7.

An example of tension-induced wrinkling is that of a free polyethylene sheet of length L, clamped on either side with uniform tension, T, in one direction, as shown in Fig. 1.8. Upon stretching, the poisson effect causes the sides to contract. Near the clamps, the sheet is held flat. Toward the center, the sheet experiences a compressive stress perpendicular to the tension. After some critical extension, the sheet buckles,

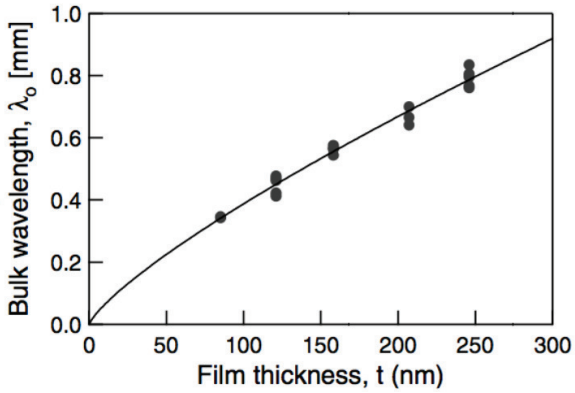

Figure 1.7. Wrinkle wavelength is predicted by (1.20).[15]

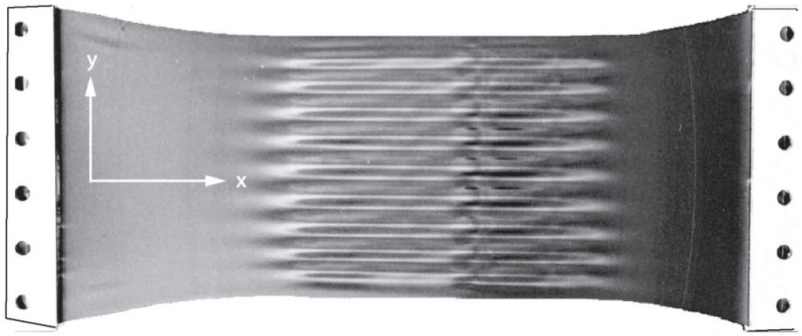

Figure 1.8. Horizontal tension on a free sheet creates compression in the vertical direction by the Poisson effect. Wrinkles are induced perpendicular to the compression.[6]

and wrinkles appear, as shown in Fig. 1.8. The bending energy is minimized by the largest wavelength, but a consequence of this would be a large amplitude wave, which would cost more stretching energy in the direction that is already under tension. The resulting wavelength involves a ratio of the bending modulus and tension [6]:

$$\lambda = 2\sqrt{\pi}\left(\frac{B}{T}\right)^{1/4} L^{1/2} \tag{1.21}$$

In either case, wrinkles extend throughout the sheet, and the pattern is described completely by its wavelength.

1.1.4 What we will mean by 'crumpling'

Figure 1.9. Familiar crumpled objects with pointy features.[4]

Fig. 1.9 shows what naturally comes to mind when one thinks of crumpling: large sheets packed into small balls. Packing fraction and particular confining shape aside, another conspicuous feature is visible in the image. That is the non-uniform distribution of sharpness and flatness in the crumpled balls. The conical points and edges that connect them were not prescribed in the process of crumpling the sheets. They could easily have been formed by soft, uniform hands: boundaries which wouldn't obviously induce pointiness. Somehow, the sheets respond to spherical confinement by concentrating curvature in small regions. It is this process of spontaneous, non-uniform redistribution of curvature and stresses due to external confinement that we will associate with the word 'crumpling'.

One (perhaps fundamentally) simple path toward such focusing occurs when boundary conditions insist that the overall shape possess gaussian curvature. A demonstration calls for a circular thin sheet and a cup. If one pushes at the center very gently (or uses a very soft or thick sheet), it may smoothly bow into the cup axisymmetrically.

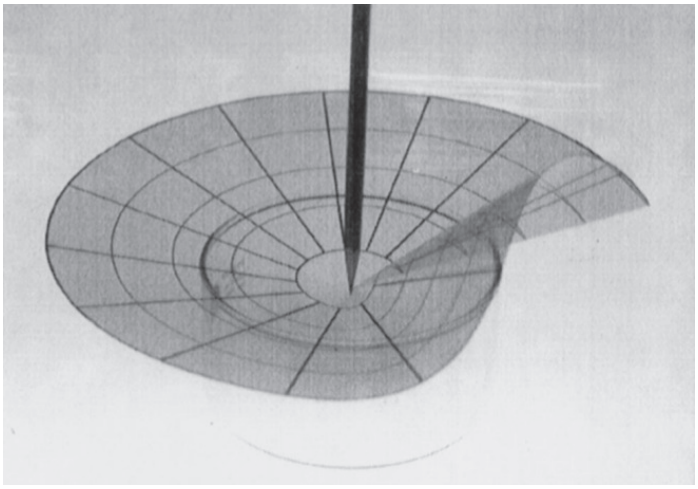

Figure 1.10. Pointiness of the d-cone results from spontaneous stress focusing, not the pointiness of the pencil. [5]

In doing so, stretching energy accumulates as in-plane stresses distribute throughout the sheet and it resembles an upside-down Fig. 1.4. Push further, and the sheet adopts the shape depicted in Fig. 1.10. Here, the azimuthal symmetry is broken, and the sheet lifts off of the cup on one side. One can confirm that the radial lines drawn on the sheet are, in fact, straight, except for a small region near the center. This means that the gaussian curvature, and therefore the stretching energy is focused at the center. Because the majority of the shape is flat one direction, it is known as a developable cone, or 'd-cone'[2]. The tip of the cone, where all the gaussian curvature lives is shaped like a crescent pointing in the direction where the cone lifted from the boundary. The presence of a d-cone indicates that the in-plane stress field no longer smoothly varies. In this case, the axisymmetry was broken in both the shape of the sheet and in its stress field. Careful observation of 'crumpled' sheets will generally reveal d-cones and other stress-focused structures.

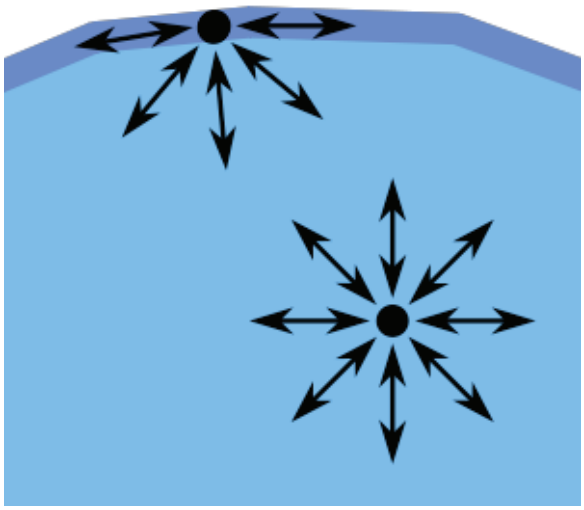

Figure 1.11. Origin of surface tension [public domain image from wikipedia]

1.2 Capillarity

In the next chapter, the 'capillary forces' deriving from the surface tension of a drop of water will play the role of deformer of a thin sheet. A complete conceptual understanding of these forces requires only a little background so it is worth starting from the beginning.

A characteristic property of fluids is that they can flow. This means that they must not have a reference metric, and they do not pay an energetic price for shear strains. Static fluid elements only experience hydrostatic pressure. A fluid can take the shape of a solid container, but what happens at free surfaces? There, cohesive forces between liquid molecules become important. Fig. 1.11 shows a surface between a liquid and air. Arrows on a sample molecule in the bulk indicate the number of bonds it shares with its neighbors. For water, these are hydrogen bonds. For oils, they come from van der Waals interactions. In any case, they lower the energy of the system. The sample molecule on the surface has fewer bonds, as it doesn't enjoy the same bonds with the available air molecules on that side. If a molecule would pay an

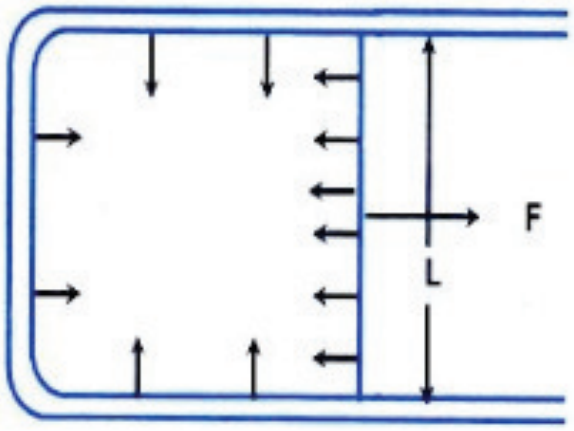

Figure 1.12. Surface tension exerts a force on a wall. [9]

energy U_0 to break all the bonds and leave the bulk, then it would pay half that to sit on the surface [9]. Therefore, exposing more area by putting more molecules on the surface costs energy. Ignoring, for now, the entropy difference between bulk and surface, the interfacial energy, γ, would be:

$$\gamma = \frac{1}{2}\frac{U_0}{a^2} \tag{1.22}$$

where a^2 is the area one molecule occupies on the surface. In general, γ can be defined thermodynamically as:

$$dU = \gamma dA + PdV + TdS + ... \rightarrow \gamma \equiv \frac{\delta U}{\delta A} \tag{1.23}$$

where U is the free energy of the system.

One physical consequence of the surface energy is that a line tension, γ, is formed on the surface. In Fig. 1.12, a liquid film extends between three fixed walls and one movable wall of length L. The surface tension pulls perpendicular to the wall from

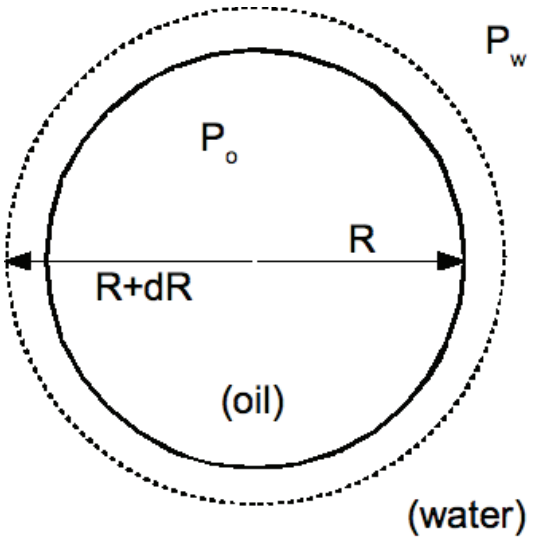

Figure 1.13. Origin of Laplace pressure in an oil drop [9]

front and back of the film, in trying to minimize the energy. The resulting force required to prevent the wall from sliding to the left is simply:

$$F = 2\gamma L \tag{1.24}$$

A free liquid body will pull its surface to the smallest shape able to contain its volume: a spherical droplet. As demonstrated above, a line tension exists along its surface. When the surface is curved, this line tension creates another physical consequence, known as the Laplace pressure. Fig. 1.13 depicts a spherical oil-water interface with pressures P_o on the inside and P_w on the outside. The differential free energy for which only the radius is allowed to vary is:

$$\begin{aligned} dU &= -P_o dV_o - P_w dV_w + \gamma dA \\ &= 4\pi R^2 dR(P_o - P_w) + 8\gamma\pi R dR \end{aligned} \tag{1.25}$$

At mechanical equilibrium, $dU = 0$, which gives the Laplace pressure:

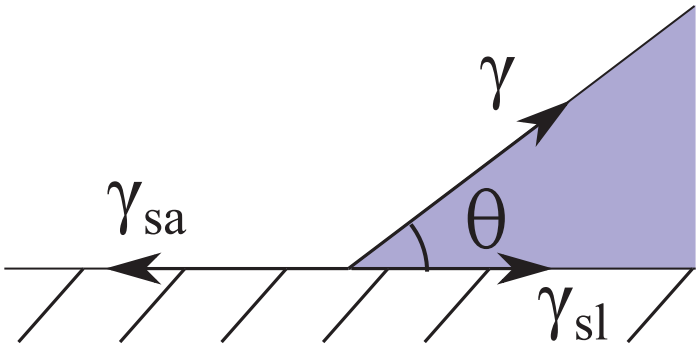

Figure 1.14. Contact line between 3 phases.

$$P_o - P_w = \Delta P = \frac{2\gamma}{R} \tag{1.26}$$

The Laplace pressure pushes uniformly outward, normal to every point on the surface.

It is worth noting that the above ideas of surface energies, in principle, also apply to solids. However, elastic energies dominate the larger-scale deformations that we are typically interested in.

1.3 Solids Meet Liquids

A liquid drop will conform to the shape of a solid to the extent that it is energetically favorable. In 'wetting' a solid surface, an area of liquid-air interface and an area of solid-air interface is replaced with an area of solid-liquid interface. Evaluating this trade-off in energies gives us the familiar Young-Laplace equation:

$$\gamma cos\theta = \gamma_{sa} - \gamma_{sl} \tag{1.27}$$

where γ, γ_{sa}, and γ_{sl} are the liquid-air, solid-air, and liquid-solid interfacial energies, and θ is the three-phase contact angle, as seen in Fig. 1.14.

However, even in this simple case, the solid must conform to some extent to the droplet by deforming at the contact line. The vertical component of γ that doesn't

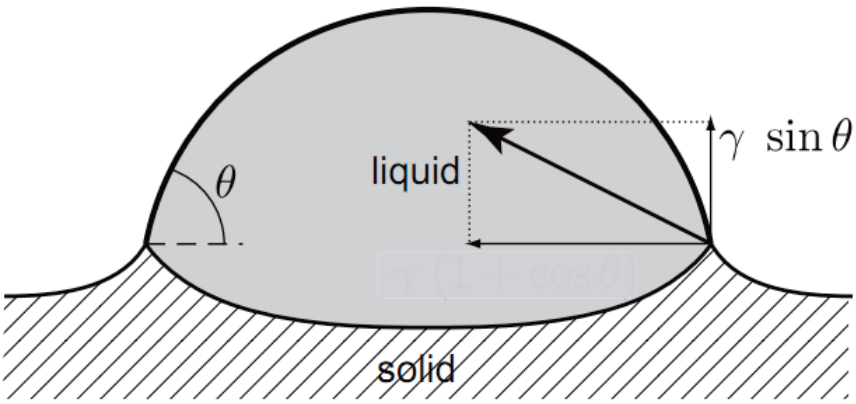

Figure 1.15. Surface tension deforms a soft substrate on the contact line.[7]

appear in the Young-Laplace equation does exactly that, as originally predicted by Ref. [34], recently reported by Ref. [20, 7] and illustrated in Fig. 1.15. Here, elastic stresses resist deformation in the substrate as the liquid pulls upward at the contact line, trying to cover its exposed surface.

If the elastic substrate is thin and has nearby free edges, it can be coerced into bending around the drop (Fig. 1.16). The competition between bending and surface tension gives rise to a characteristic 'elastocapillary length'[30]:

$$l_{ec} = \left(\frac{B}{\gamma}\right)^{1/2} \tag{1.28}$$

which sets the regime where this 'origami' is possible ($l_{ec} << size$). Shown is a $\approx 50\mu m$ thick, $\approx$1mm wide square sheet of PDMS, for which surface tension is just enough to access the bending energy in forcing it to buckle. The sheet is still too thick, however, to allow appreciable stretching.

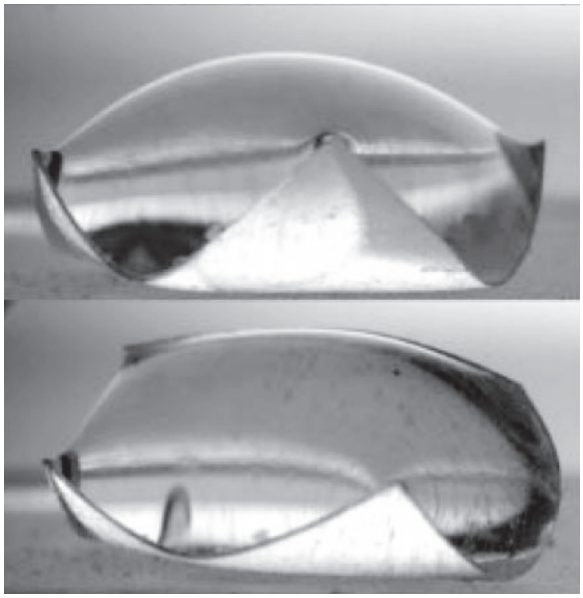

Figure 1.16. Interfacial energy of a drop is minimized by covering its surface with relatively low energy interfaces of the sheet. In doing so, the sheet is compelled to bend. Competition between bending resistance and capillarity, characterized by the 'elastocapillary length', determine the the shape shown here[30].

CHAPTER 2

WRINKLING OF A SHEET ON A DROP

2.1 Introduction

This chapter describes an experiment conducted by H. King and N. Menon and the related theoretical work by R. Schroll and B. Davidovitch [22].

The basic question that motivated the sheet-on-a-drop project was: how does a flat sheet respond to applied gaussian curvature? In the previous chapter, some answers were already offered. We know that gaussian curvature induces in-plane stresses. We know that stresses can be relieved by either buckling into a wrinkle pattern or by focusing them into sharp cones, but not necessarily how much of which to expect in response to a quantifiable amount of confinement. In the examples from Figs. 1.6,1.10, the choice between these solutions and their extent were strongly encouraged by the boundaries. There haven't previously been any examples in which one type of pattern could be transformed to the other. We thought it would be revealing to force the system to break its own symmetries and choose its own mechanisms of dealing with geometric frustration. To realize this goal we studied the shapes assumed by a thin, circular sheet of polystyrene floating on a spherical droplet of water.

Fig. 2.1 illustrates the basic problem of wrapping a circular sheet around a spherical object. This brings to mind the 'map-maker's problem', in which one cannot preserve both the size and shape of features on the globe when representing them on flat paper (another way of thinking of the theorema eggregium). For two experiments in which a sheet is forced to lie on the surface of a rigid sphere, see Ref. [17, 18].

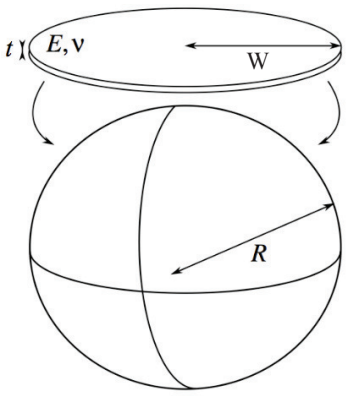

Figure 2.1. Frustration should be caused by incompatible shapes.[17]

For the sheet to lie on the surface of a spherical *liquid* drop, one or both must compromise their natural shape. Deformation of the sheet is characterized in terms of bending or stretching, and each cost energy. Deformation of the drop costs energy to the extent that the exposed area is larger than its original area. It is worth noting that the drop pays no price for deformations away from its relaxed shape (as a fluid, it has no reference metric), unless the deformations change the area of the surface.

We can imagine the trivial shapes that correspond to certain limiting cases of these three energies. If the interfacial energy is taken to be negligible compared to those of bending and stretching ($\gamma \to 0$), the sheet will simply be flat, and the drop round where it is not touching the sheet. If the stretching modulus is too large to allow stretching, but the bending resistance is not ($Y \to \infty$), we should see a situation like that of Fig. 1.16, in which the sheet bends around the drop and the drop covers some of its surface area. Alternatively, if the interfacial energy dominates ($\gamma \to \infty$), then the elastic response of the sheet becomes unimportant and the sheet is smoothly stretched over the whole surface.

In contrast with Ref. [30] (Fig. 1.16), we use 'ultrathin' ($t \approx 100nm$) sheets, like the one in Fig. 1.6, where we expect bending resistance ($B \propto t^3$) to be unable to

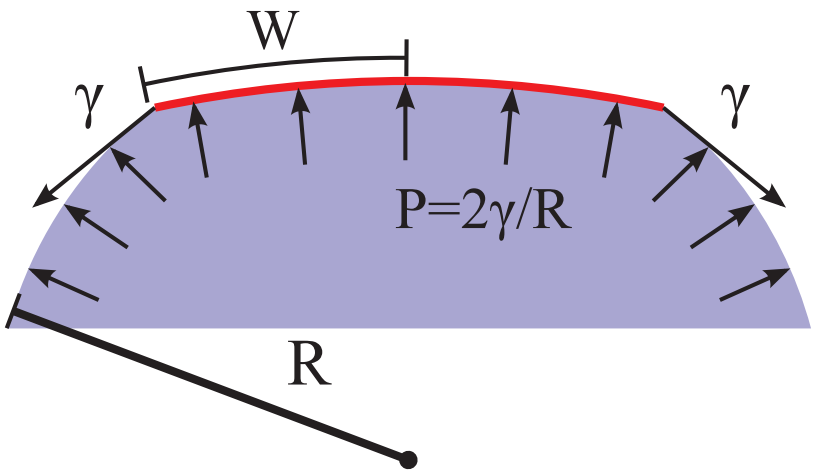

Figure 2.2. Schematic side view of the drop and sheet.

balance capillary forces. This means stretching must serve this purpose and play an important role.

Fig. 2.2 is a schematic of the system. The circular red disk is completely wetted on one surface which it shares with the liquid drop.

Exactly equivalent to the qualitative energetic statements above, it is useful to consider the forces. The sheet experiences a tension at its edge, as the liquid tries to cover its expensive interface with the air with as much of the energetically cheaper sheet as possible. Meanwhile, the curvature in the drop's free surface creates a Laplace pressure (1.26), which is exerted uniformly on the bottom of the sheet.

In terms of the forces acting on the sheet, the problem is conceptually similar to trying to make a round balloon out of two flat sheets of mylar. The result of this endeavor is not very spherical, as can be seen in Fig. 2.3. Confined by tension along its surface and constant pressure from inside, a patch on this balloon lives similar to a sheet on a drop, though the constraints on the outer boundary are very different.

Figure 2.3. Side view of inflated mylar balloon shows that uniform normal pressure and in-plane tension on an initially flat sheet make a rounded, but not spherical shape.

2.2 Qualitative Observation of 2 Transitions

Having designed a setup to control the curvature of the drop and view small surface features from top view images (to be described in detail later), we found the three, qualitatively different types of shapes shown in Fig. 2.4. We saw the initial axisymmetry in shape was broken at some non-zero value of curvature, and then again in a different way at a different value of the same quantity. Loosely speaking (at this point) there appeared to be sequential smooth-to-wrinkle and then wrinkle-to-crumple transitions induced by changing the pressure in the drop. In this chapter we focus first on the smooth-to-wrinkled transition alone; specifically the onset, extent, and wavelength of the wrinkle pattern. We had the luxury of measuring the properties experimentally while theoretical predictions were being formed by R. Schroll and B. Davidovitch.

2.3 Parameterization

When wrinkling was introduced in Sec. 1.1.3, the examples given had uniaxial confinement and patterns which spanned the system. The wrinkles in Fig. 1.6 extend

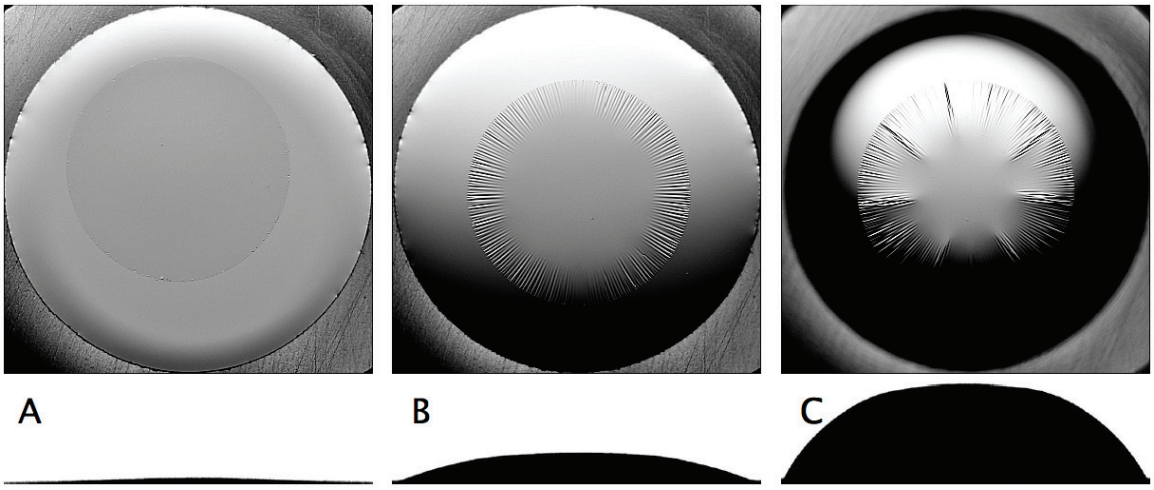

Figure 2.4. Top and side views of a sheet on a drop with progressively increasing curvature show the sequence: (A) sheet curved into smooth cap, (B) 'wrinkled' sheet, (C) 'crumpled' sheet

normal to the compressive strain directly imposed by hard walls. In Fig. 2.4, we see wrinkles extending a finite distance radially inward from the edge. This should tell us that there is a compressive stress in the azimuthal direction toward the edge, but not in the middle. We should recognize this behavior by now: even from Fig. 1.4, we saw that to the extent the sheet accepts gaussian curvature, either the radial lines need to stretch or circumference lines need to contract. Because the sheet is under tension radially, it is reasonable to assume the compressive hoop stresses are at least partly relaxed by stretching. The radial extent of the observed wrinkle pattern is a quantity, then, which depends on mechanical as well as geometric parameters. It should tell us where in the sheet there is sufficient compressive stress to induce buckling. How much compressive stress can be induced by the drop and how it compares with the buckling threshold are the two parameters which have to be quantified in order to make best use of the experimental data.

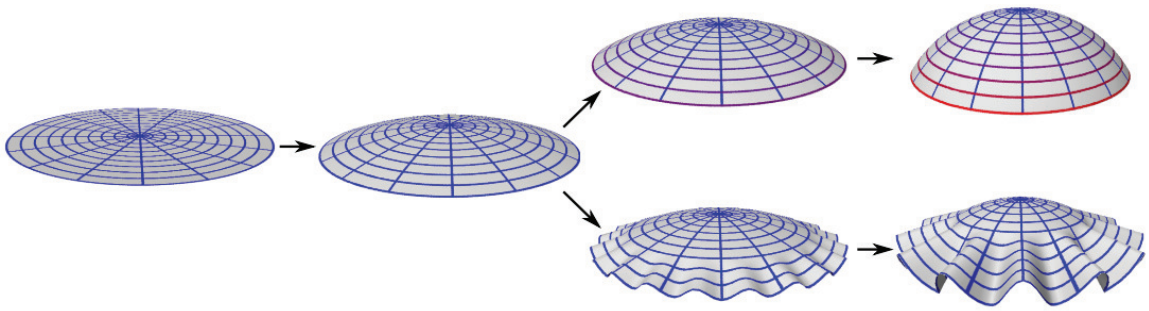

Figure 2.5. Schematic plots that mimic the radial and hoop strains upon imposing a spherical shape on a circular sheet. The confinement increases from left to right. Blue represents small strains (tensile or compressive), and red represents large compressive strains. Upper path: Increasing confinement on a sheet that is required to maintain an axisymmetric shape. Lower path: Increasing confinement on a sheet that is allowed to release compression by wrinkling.

The first quantity we will call 'confinement'. Its dependence on available quantities can be determined by considering the two types of axisymmetric solutions suggested above:

(i) If the sheet is small compared to the radius of curvature of the drop ($W/R \to 0$) or the exerted tension is strong compared to the stretching modulus ($Y/\gamma \to 0$), the stress will be tensile everywhere in the sheet in both radial and azimuthal directions. This case, where the drop is only slightly deformed, is similar to radial stretching of an unsupported sheet, and the drop's curvature has only a small effect. Such a purely tensile state is stable against buckling.

(ii) However, if the sheet is sufficiently large or the tension sufficiently weak, the drop resists its deformation and the hoop stress of the axisymmetric state becomes compressive in an annulus $W - L < r < W$ close to its outer edge, signifying a wrinkling instability of the axisymmetric state as shown in Fig. 2.5C. Here, the drop's curvature has an effect similar to projecting a flat sheet onto an undeformable sphere, where the confinement of circular latitudes increases with their radius.

This qualitative discussion suggests that the onset and extent of compressive azimuthal stress in the sheet on a drop is determined by the 'confinement' parameter α. When formally derived as the one governing parameter in the 'membrane limit' of the Föppl–von Kármán (FvK) equations (see Sec. 2.5),

$$\text{confinement:} \quad \alpha \equiv \frac{Y}{\gamma}\left(\frac{W}{R}\right)^2 . \tag{2.1}$$

which agrees with the expectation from the qualitative argument.

As discussed in Sec. 1.1.1, a thin sheet will buckle, and in doing so relax compressive stresses, only after it has been pushed beyond its threshold. If α indicates the compressive loading of the would-be wrinkle pattern, another parameter must indicate its characteristic bucklability or *bendability* [8] under that loading:

$$\text{bendability:} \quad \epsilon^{-1} \equiv \gamma W^2/B \ . \tag{2.2}$$

This quantity should look like the inverse of the critical strain in Eq. 1.14, except that the stretching modulus has been replaced by surface tension. The point is that this quantity measures the ability for a characteristic applied force (here, surface tension) to push the system over the threshold. A sheet with bending stiffness B and length W will reach its threshold strain when the compressive force per unit length (here, γ) is of the order Y. Two limiting cases can be distinguished by the value of bendability:

(i) $\epsilon^{-1} \approx 1$ Near threshold: Though the shape symmetry is broken and the sheet is forced out of plane, the effect on the compressive stresses is considered negligible. In other words, the bending response of the slightly buckled sheet is approximately enough to carry the load that caused it to buckle.

(ii) $\epsilon^{-1} \ll 1$ Far-from-threshold: The bending resistance of the buckled sheet is negligibly small, such that it cannot support any compressive stress.

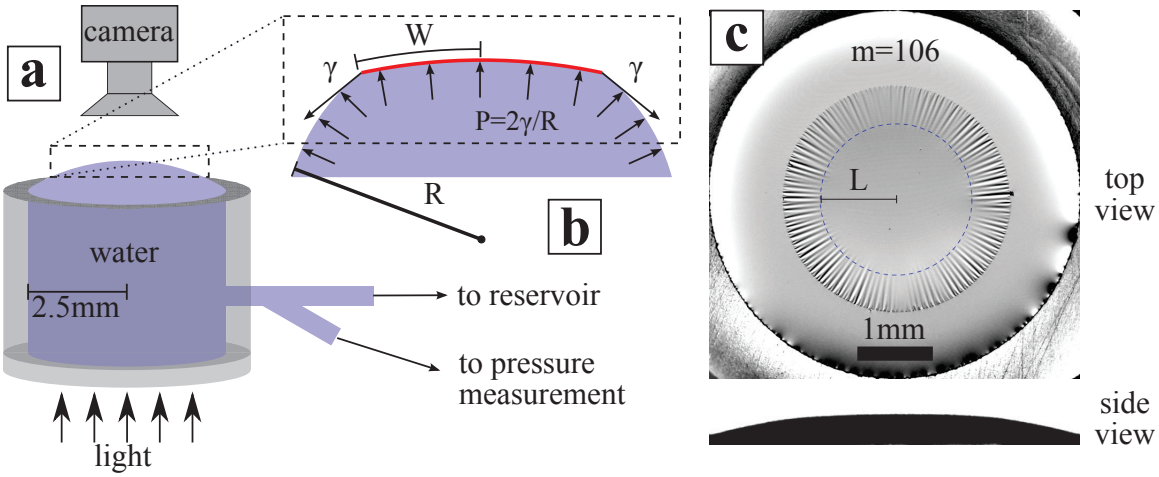

Figure 2.6. (A) Experimental set-up indicating the radius W of the sheet, and the radius of curvature R of the exposed part of the fluid drop beneath. (B) Schematic side view of the drop and sheet. (C) Top and side views of the wrinkled sheet on the drop. The length, L, and the number m of wrinkles are computed by analysis of the top view image.

In the following experiment, configurations of the film are measured as functions of variable α, all data falling within a narrow range in the small ϵ ($2\text{x}10^{-7} - 5\text{x}10^{-6}$), highly bendable regime.

Fig. 2.6 shows the basic setup of the experiment. A meniscus on an overfilled tube served as the drop, as seen in (A). Increasing the amount of water in the meniscus amounted to decreasing the radius of curvature of the portion of spherical drop that protruded from the tube. Photographs taken from the side indicated the amount of confinement while photographs taken from above revealed the resulting features in the film. The feature to be considered here first is the wrinkle pattern that radiates inward from the edges in (C). The pattern was quantified by the wrinkle number, m, or wrinkle angle $\theta = 2\pi/m$, and the wrinkle length, L, both measured from the top view images.

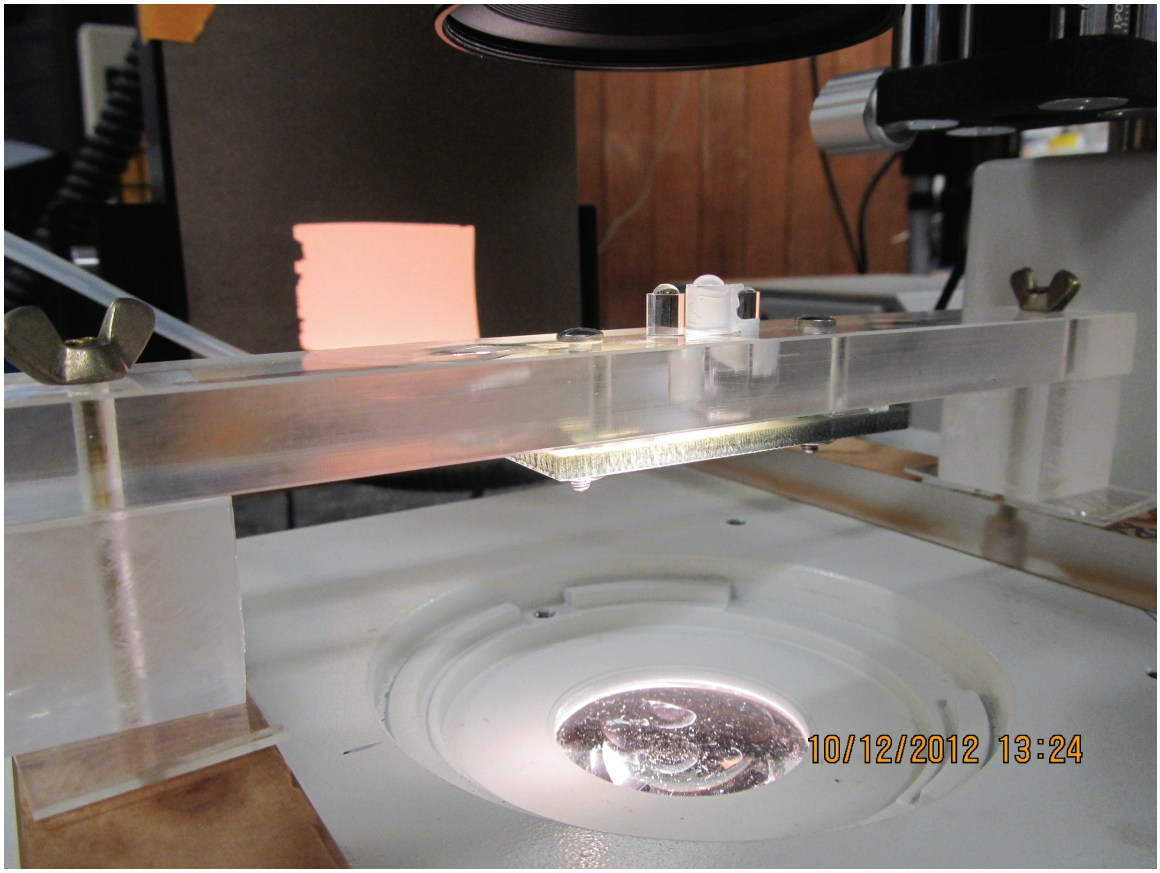

Figure 2.7. Three hydrophobic tubes (inner diameters 5,6,7mm) are set in holes in an acrylic base, and sealed with teflon tape. In order to allow for an optical path from the lighting below through the middle meniscus, the middle hole passes through the base and is sealed from below with a piece of microscope slide, which is pushed against the acrylic base and teflon-tape gasket by a plastic plate. The plastic plate is held against the slide by screws and has a hole to allow light to pass through. The holes supporting the tubes on either side tilt inward to join the center hole so that pressure can equilibrate across all menisci.

2.4 Experimental Procedure

2.4.1 Making the Drop

The 5mm (inner diameter) tube depicted in Fig. 2.6(A) and shown in Fig. 2.7 was set in a hole through an acrylic base. The hole was sealed on the bottom by a glass slide to keep the setup watertight and transparent to allow for illumination from the microscope base beneath. The surface of the tube was silanized in order to pin the contact line at the inner diameter of its top edge. Also fixed in the base on either side of the 5mm tube were 4mm and 3mm (inner diameter) silanized glass tubes, set at two different heights, both lower than the center tube. A tunnel in the acrylic base allowed water to freely pass between the tubes, and connected them to a reservoir set on an vertically adjustable stage. Upon raising or lowering the reservoir, the drops on all three tubes grew or shrunk in unison.

2.4.2 Making the Sheet

Films were spin coated from a dilute solution of polystyrene in toluene onto a clean glass microscope slide.

Polystyrene (atactic, number-average molecular weight Mn=91 K, weight-average molecular weight Mw=95 K) (Polymer Source Inc.) was dissolved in toluene at 1, 1.5, or 2 % concentrations by weight. After combining the two ingredients, it was set aside for 1 day to for the polystyrene to fully dissolve. Then the solution was forced by syringe through a Whatman PVDF $0.45\mu m$ pore filter (which connects by luer lock to the syringe) into a clean vial. It is important that the filter housing and membrane are not soluble in toluene, as is, for instance, polypropylene.

A clean slide from a package of (Fisherbrand) plain glass microscope slides was chosen upon inspecting by eye for imperfections such as scratches or dirt. (About 1 in 5 slides was deemed clean enough to use for spin-coating.) Dust was removed with pressurized air. The slide was then cut with a glass cutter into thirds, which were

Table 2.1. Spin Coating Recipes

Concentration:	Speed	Thickness
1%	800 RPM	67 ± 2 nm
1%	2000 RPM	46 ± 2nm
1.5%	800 RPM	77 ± 2nm
2%	800 RPM	136 ± 10nm
2%	2000 RPM	94nm ± 2nm

approximately square, avoiding touching the side intended for the film to come in contact with any tiny glass fragments, as they can damage the surface. The portion of slide was brought to the spin coater. This simple device holds the glass slide from below with a vacuum seal and spins horizontally at constant speed. We use it to deposit the ultrathin film of polystyrene from a dilute solution because it is simple and provides uniform thicknesses.

Then, the slide was rinsed with acetone while sitting on the spin coater. The acetone was spun off (at whichever speed was being used at the time) for one minute. A large bead of polystyrene-toluene solution was pipetted on the surface. Then, the slide was spun (between 800 and 2000 RPM) for 60 seconds. In this time, the excess material is spun away and all remaining toluene evaporates, leaving a uniform thickness polystyrene film [13, 42]. Different film thicknesses were obtained by varying spin speed and/or using a solution of different concentration. A few typical recipes are listed in Table 2.1.

A white-light interferometer was used to measure the thickness of a given film. A portion of film near the sample to be used in the experiment was cut, floated on water (described below) and caught on the surface of a silicon wafer. The interferometer (Filmetrics Inc., F20-UV thin film measurement system) used a regulated deuterium and tungsten-halogen high power UV-vis fiber light source (Hamamatsu Inc.). The interferometer, calibrated to the reflectivity of silicon, determined the thickness of the film by shining light (with broad wavelength range 200 to 1100nm) normal to the

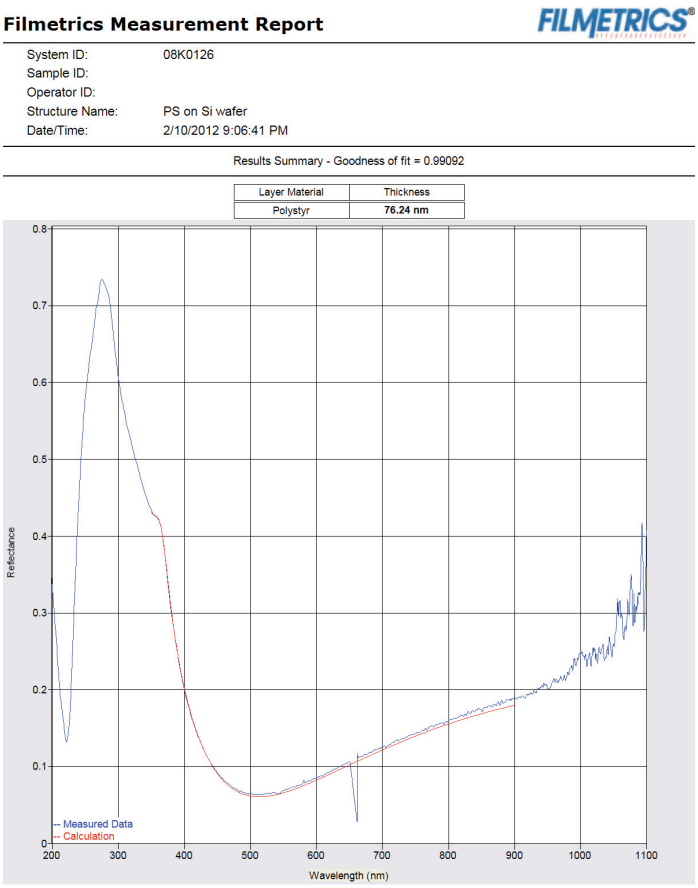

Figure 2.8. Screen shot of interferometer data analyzing software calculating the best fit to the reflected spectrum, corresponding to a 76nm thick polystyrene film on silicon.

film on the silicon substrate, and analyzing the spectrum as it reflected back to the sensor. The analysis program takes the indices of refraction of PS and Si to calculate the amount of expected interference for each wavelength between 350 and 900nm, as shown in Fig. 2.8. Based on the relative intensities in the reflected spectrum, the program produces a best fit film thickness. The incident beam is small enough ($2mm$) that different locations on a sample film can be measured. The error in Table 2.1 is the standard deviation in several measurements across the surface of a roughly 15x15mm sheet. The average values were used for our calculations. Sample

measurements by x-ray reflectometer (PANalytical X'Pert X-ray diffractometer) and optical profilometer (Zygo NewView 7300) were found to be consistent.

Next, a circular portion of the sheet had to be removed from the glass. An aluminum die was placed on the surface of the slide. A cylindrical carbide bit with

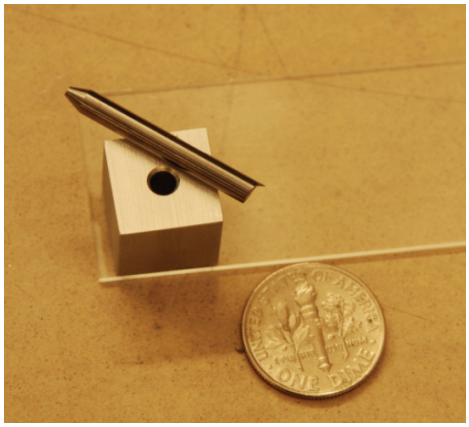

Figure 2.9. Cutter and die.

a burr on one corner was inserted snugly into the die (see Fig. 2.9) until the burr lightly touched the polystyrene surface. Rotating the bit by hand produced a clean, uniformly circular cut in the polystyrene film. Because carbide is harder than glass, it was easy to allow the bit to sink into the surface of the slide while cutting. Doing so sent glass fragments into the film around it, and produced jagged edges. Imperfections in the cut edge strongly affected the reproducibility of the results, so the cutting was done delicately as possible.

The slide was then slowly submerged in a deep dish of water. The encroaching water-air interface peeled the cut portion of film from the glass, holding it taut on the surface of the water.

Next, it was necessary to transfer the delicate film to the experimental setup without causing damage. A glass tube with the same diameter as the fixed 5mm tube in the setup was dipped into the water just surrounding the polystyrene disk such

that the inner diameter of the tube was wetted. Upon lifting the tube, a small amount of water plus the film was extracted from the large dish. This tube with the water and film covering its bottom surface, was placed on top of the fixed tube (depicted in Fig. 2.6), in which water already was filled to the top edge, so that the water in each tube joined. Backing off the water from the reservoir, the transfer-tube could be removed, thus leaving the circular film on the meniscus of the fixed tube. Due to the sensitivity of the sheet to damage and self-adhesion, it is important that the whole process be performed without having directly touched it with a solid object.

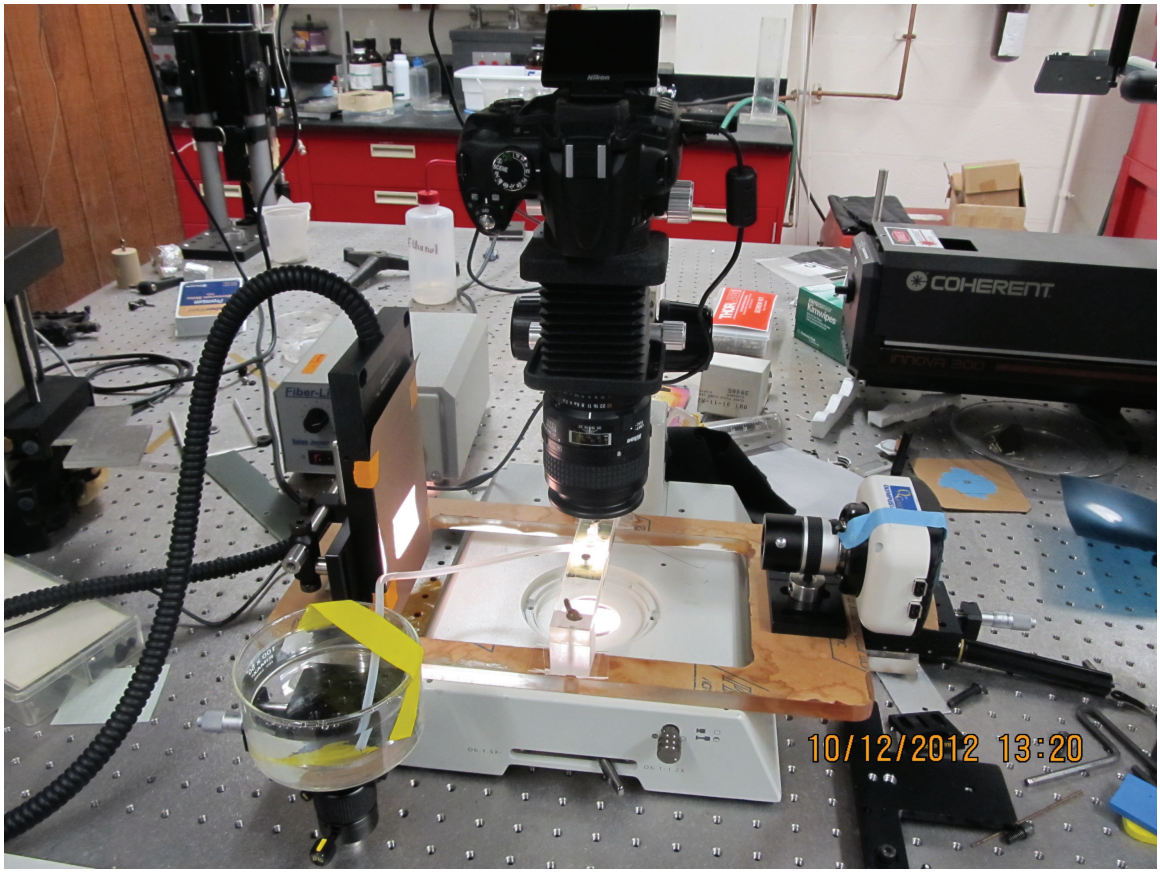

Figure 2.10. The complete experimental setup. The camera and bellows operate in place of a stereomicroscope, on whose base the whole apparatus sits. The side view camera and its backlighting source are fixed to the large acrylic platform to which the tubes in Fig. 2.7 are also firmly attached. The external reservoir (bottom left) rests on a vertical stage to give variable pressure to the three menisci through the tube which enters the acrylic base through a hole in its side.

2.4.3 Measurement and Analysis

The confinement parameter α was extracted from the side view images. Wrinkle length and wrinkle number were extracted from the top-view images. That procedure is described in this section. Accompanying each top view image, a side view camera obtained silhouettes of the drops, illuminated by a distant, uniform source, as shown in Fig. 2.11. The film rested on the raised center drop. A circular least squares fit gave

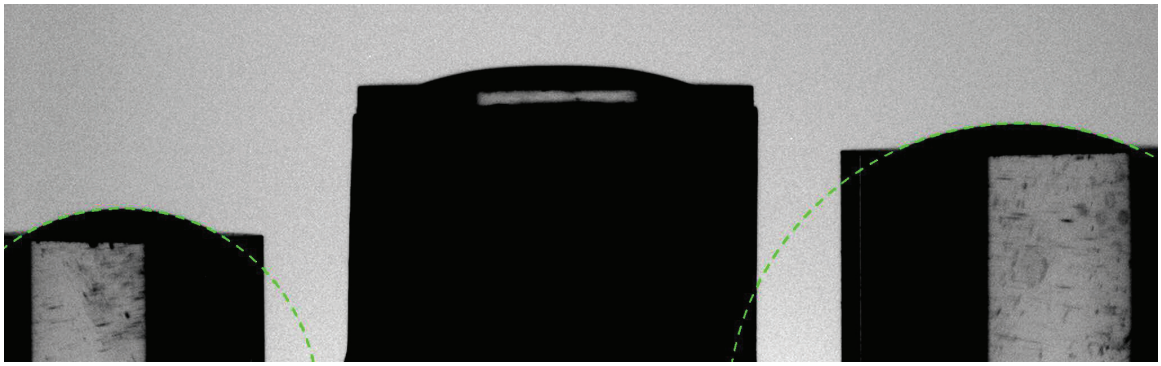

Figure 2.11. Side view of the three tubes. Circular fits to the menisci on the two lower tubes is used to calculate the pressure underneath the center drop holding the film, whose shape is no longer spherical.

the radius of curvature R' of either of the two exposed drops, used in calculating the Laplace pressure and the drops volume V. This information, along with the height difference from the center tube, was used to calculate the pressure under the film:

$$P = \frac{2\gamma}{R'} + \frac{\rho g V(R', a)}{\pi a^2} + \rho g(h - h_0) \tag{2.3}$$

where a is the inner radius of the corresponding tube, h and h_0 the heights of the given side tube and center tube, respectively. The duplicate calculation from the second tube was used as a self-check, and the average of the two was used to calculate α:

$$\alpha \equiv \frac{Y}{2\gamma}\left(\frac{W}{R}\right)^2 \approx \frac{YW^2P^2}{8\gamma^3} \tag{2.4}$$

Typical disagreement between the two values was approximately 1Pa at low α, where

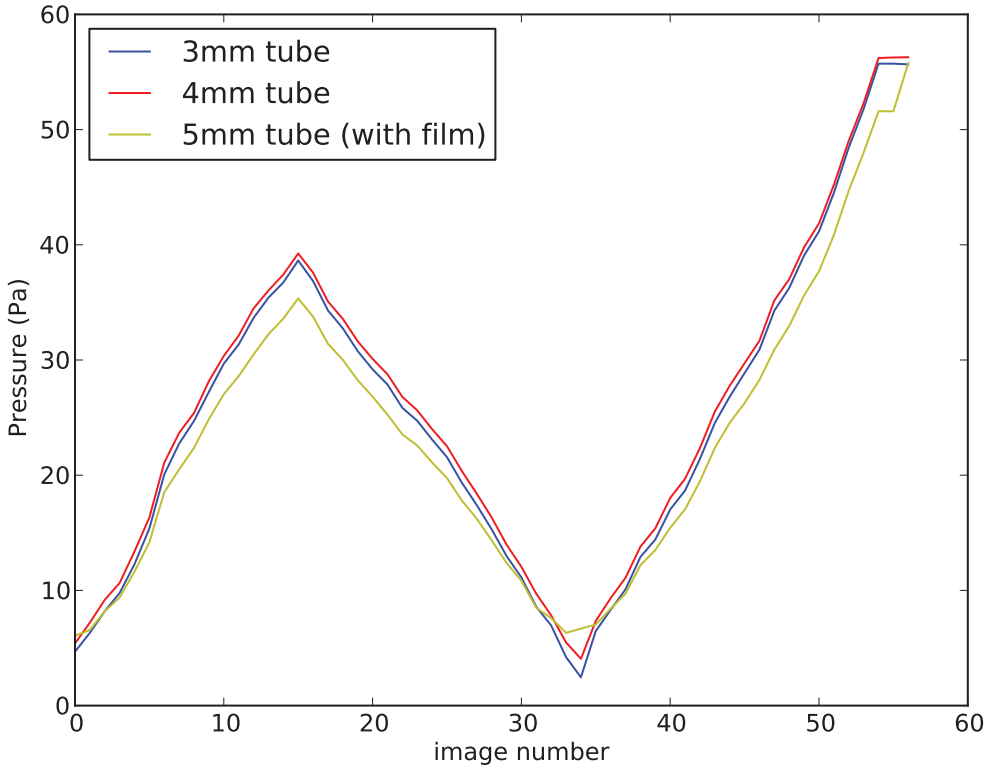

Figure 2.12. Pressure measurements from the 3mm and 4mm tubes were used to calculate α in Fig. 2.16. The program also fits a circle to the film+drop profile on the 5mm tube, giving an inconsistent measurement (which isn't used). Before the last picture was taken, the film was removed from the drop, which is why the points converge at the very end.

the error was greatest, presumably due to contact line irregularities. The estimated uncertainty based on this disagreement is displayed as error bars on Fig. 2.16. Because the side tubes were set lower than the center tube, their menisci were large enough to be measured even when the top meniscus was flat. This allowed us to obtain very small pressure values with good accuracy.

Imaging the nanoscopically thin, transparent film depended on refraction of the backlighting (white light from a stereomicroscope base) through the top surface. The local slope of either exposed drop or film determined whether light would be refracted away or continue upward into the camera lens. Darkness in the images, then, repre-

sent steeper slopes. To enhance the contrast of small slope features, an internal mirror slightly tilted the incident light from vertical. The desired magnification, depth of field, and on-axis optical path was obtained by removing the optical components of a stereomicroscope and replacing them with a Nikon D-5000 digital camera equipped with a Nikon PB-4 bellows (for close-up photography), as shown in Fig. 2.10. The camera height could then be manipulated by hand to focus the image without changing the magnification. Extracting a data point from a top-view image was a mostly automated, several step process.

First, the radius and center were determined by manually fitting a circle to the film circumference with Imagej[1]. A user plugin was employed to extract pixel value around circles at each distance from the center, as a series of arrays, one for each distance from the center. An element was recorded every 1/1000 radians, to approximately match the resolution at the film edge. At smaller radii, individual pixels could be counted more than once. Further analysis was done on these arrays in Python[31]. Because of the tilted backlighting, an unwanted vertical intensity gradient appears in all the raw data. This was removed by high-pass filtering each array with a 2 radian cutoff.

Fig. 2.13A shows a portion of the original image. The dashed blue line shows the source of the sample filtered array in Fig. 2.13B. The autocorrelation function of that array is shown in Fig. 2.13C. The presence of wrinkles at a given length was identified by the magnitude of the standard deviation of the array corresponding to that length. The wrinkles were defined to end where the standard deviation dropped below a threshold value, chosen once for a complete data set, such that it gave a result consistent with an estimate by eye. (The problem with simply measuring all data by eye is that it is very difficult to consistently judge the location of a blurry edge.)

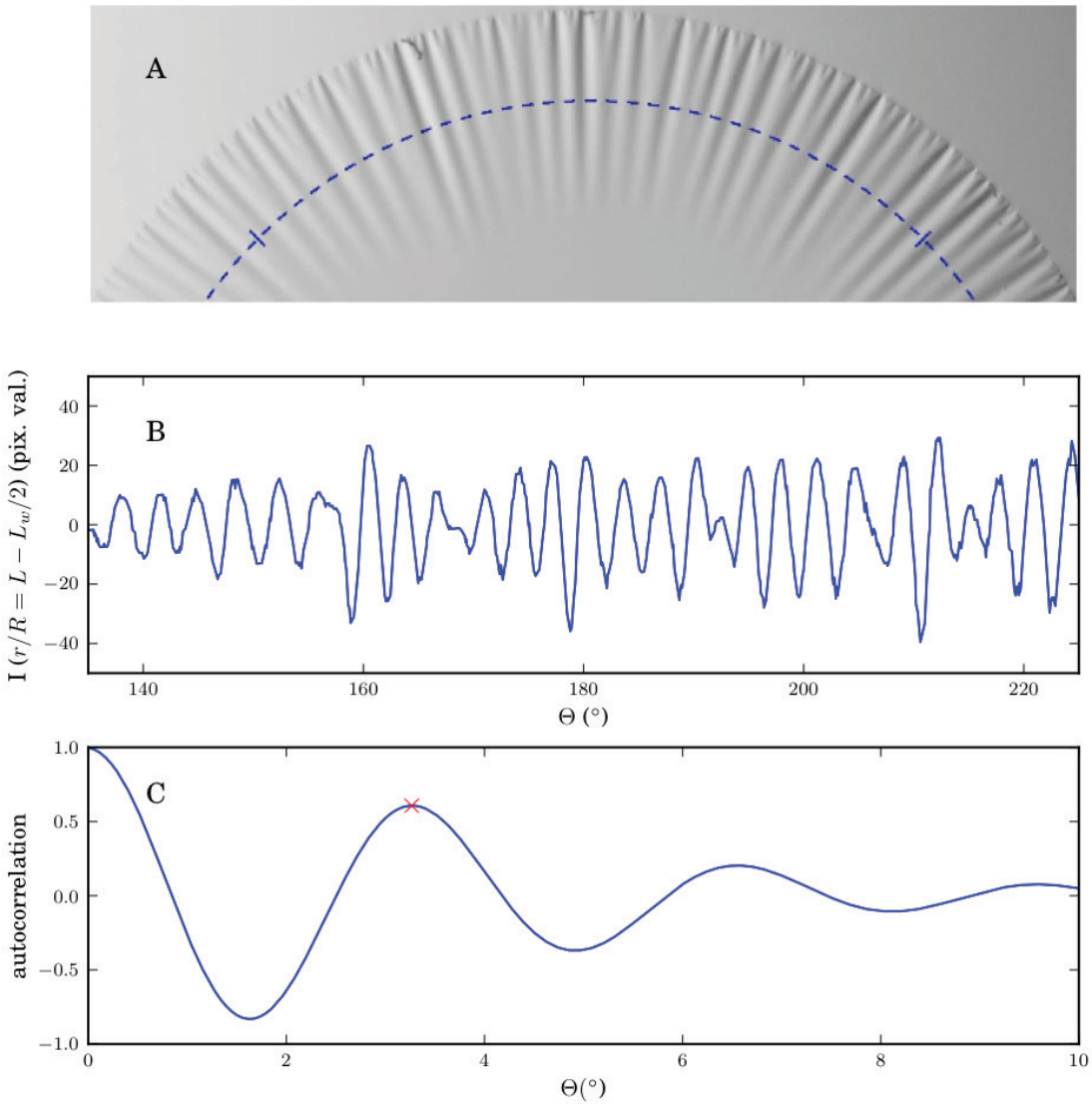

Figure 2.13. (A) Close-up of edge, indicating the axial slice analyzed to produce wrinkle number data. (B) Intensity in 8-bit pixel value, $I(\theta, r/R)$, over the range shown above. (C) Autocorrelation function in θ. The first peak in the autocorrelation function is interpreted as the wrinkle angle $=2\pi/m$

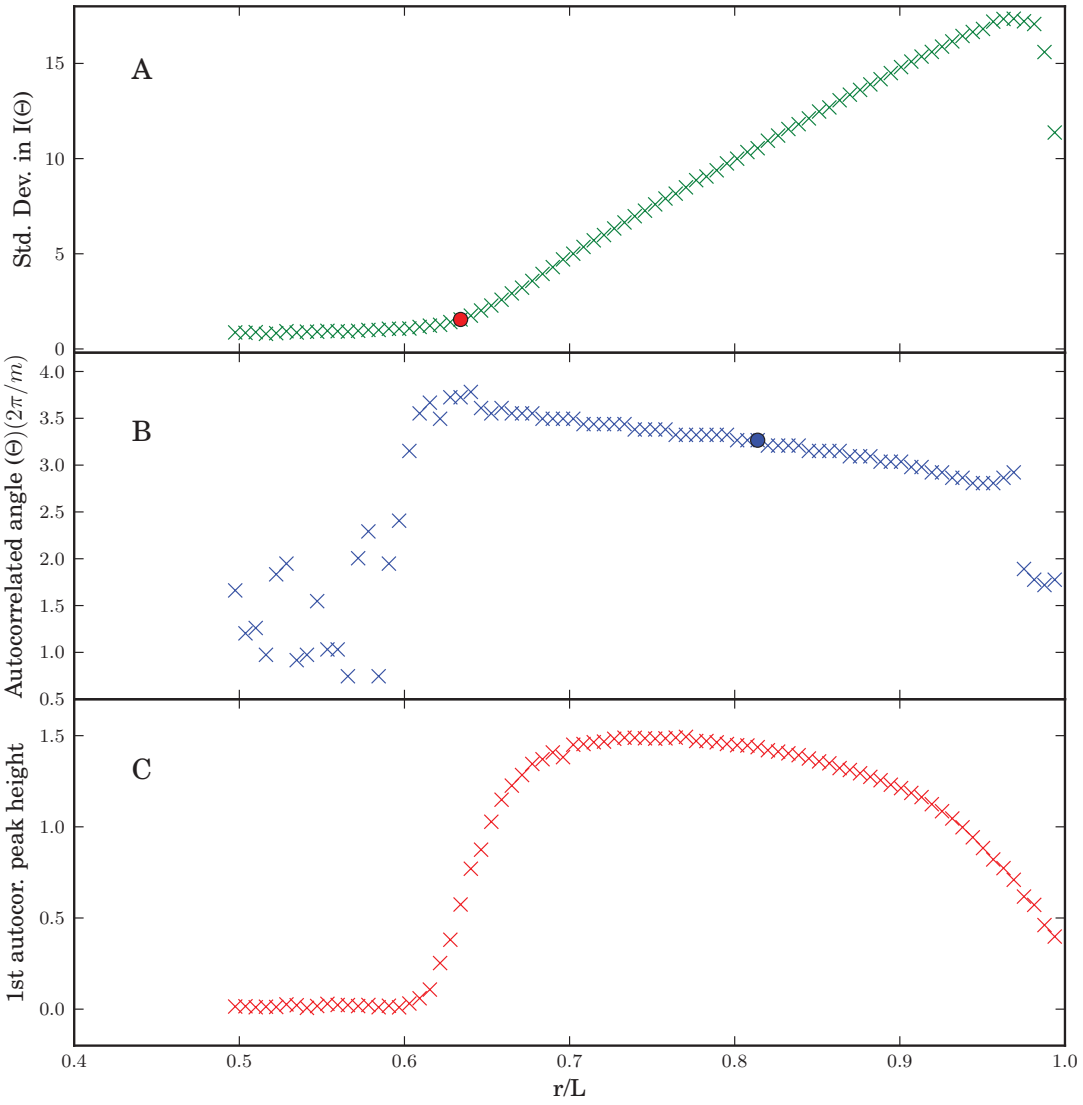

Figure 2.14. (A) Standard deviation of the pixel value arrays as a function of the radius at which they were measured. The red dot marks the wrinkle length L: where the value fell below the threshold (here=3). (B) Autocorrelation peak position θ (^{o}), for each array. The blue dot marks the measured wrinkle angle ($2\pi/m$): first autocorrelation peak at $L/2$. (C) Magnitude of the autocorrelation peak, which disappears toward L

Fig. 2.14A shows the standard deviation of arrays at different radii, and the measured wrinkle length for this sample. Tiny imperfections in the cut edge of the film

were also picked up by the program, such that L deviated slightly from 1 even below the wrinkling transition, apparent in Fig. 2.16 and Fig. 2.20. Wrinkle number m was calculated from the location of the peak in the autocorrelation function calculated at $L/2$. The value for this sample is indicated in Fig. 2.13C and Fig. 2.14B. Clearly, the value is not constant over the whole pattern. Surface tension at the edge of the film pulls the amplitude of the wrinkle down, subsequently increasing the wrinkle number. $L/2$ was chosen for consistency and to largely avoid edge effects [15].

2.5 Theoretical Approaches and Predictions

Analytical and numerical work described in this section was done by R. Schroll and B. Davidovitch.

Prediction of the wrinkle extent comes from the calculated stress profile in the azimuthal (hoop) direction, $\sigma_{\theta\theta}(r)$. Qualitatively, we expect the stress to be tensile at the center of the sheet, but decrease and potentially cross zero as we approach the edge. We expect the radius at which the hoop stress reaches zero to predict the 'wrinkle length': $\sigma_{\theta\theta}(r = L) = 0$ (to compare with the radius of the dotted line in Fig. 2.6).

Calculation of the stress profile first requires analysis of the Föppl–von Kármán (FvK) equations, which balance bending moments out-of-plane and stresses in-plane, respectively:

$$B\nabla^2\kappa + \sigma \cdot C = F_N \tag{2.5}$$

$$\nabla \cdot \sigma = 0 \tag{2.6}$$

where κ is the mean curvature, C the curvature tensor, and F_N is an external pressure.

In polar coordinates, the strain can be expressed in terms of the in-plane displacement $\mathbf{u}(r,\theta) = u_r(r,\theta)\hat{r} + u_\theta(r,\theta)\hat{\theta}$ and normal displacement $\zeta(r,\theta)$:

$$
\begin{aligned}
u_{rr} &= \partial_r u_r + \frac{1}{2}\left(\partial_r \zeta\right)^2, \\
u_{\theta\theta} &= \frac{1}{r}\partial_\theta u_\theta + \frac{1}{r} u_r + \frac{1}{2r^2}\left(\partial_\theta \zeta\right)^2, \\
u_{r\theta} = u_{\theta r} &= \frac{1}{2}\left(\frac{1}{r}\partial_\theta u_r + \partial_r u_\theta + \frac{1}{r}\partial_r \zeta \partial_\theta \zeta\right).
\end{aligned}
$$

Using the stress-strain relationship:

$$
\begin{aligned}
\sigma_{rr} &= \frac{Y}{1-\nu^2}\left(u_{rr} + \nu u_{\theta\theta}\right), \\
\sigma_{\theta\theta} &= \frac{Y}{1-\nu^2}\left(u_{\theta\theta} + \nu u_{rr}\right), \\
\sigma_{r\theta} &= \frac{Y}{1+\nu} u_{r\theta},
\end{aligned}
$$

equation (2.5) (out-of-plane force balance) becomes:

$$
B\Delta^2 \zeta - \sigma_{rr}\partial_r^2 \zeta - \frac{2}{r}\sigma_{r\theta}\left(\partial_r - \frac{1}{r}\right)\partial_\theta \zeta - \frac{1}{r^2}\sigma_{\theta\theta}\left(\partial_\theta^2 \zeta + r\partial_r \zeta\right) = F_N \tag{2.7}
$$

and equation (2.6) (in-plane force balance) becomes:

$$
\hat{r}: \ \partial_r \sigma_{rr} + \frac{1}{r}\left(\partial_\theta \sigma_{r\theta} + \sigma_{rr} - \sigma_{\theta\theta}\right) = 0, \tag{2.8}
$$

$$
\hat{\theta}: \ \partial_r \sigma_{r\theta} + \frac{1}{r}\left(\partial_\theta \sigma_{\theta\theta} + 2\sigma_{r\theta}\right) = 0, \tag{2.9}
$$

At this point, it is very convenient to consider the axisymmetric case, and throw away all terms with ∂_θ, which includes all the shear stresses and strains. This leaves:

$$
\text{force balance in } \hat{r}: \ \left(\partial_r + \frac{1}{r}\right)\sigma_{rr} = \frac{1}{r}\sigma_{\theta\theta} \tag{2.10}
$$

$$
\text{force balance in } \hat{z}: \ B\Delta^2 \zeta_0 - \sigma_{rr}\zeta_0'' - \frac{1}{r}\sigma_{\theta\theta}\zeta_0' = P \tag{2.11}
$$

where $P = 2\gamma/R$ is the laplace pressure under the drop of radius R, and primes indicate derivatives with respect to r.

The next important assumption is that the bending term in Eq. (2.10) is negligible. (As we have already limited our focus to the axisymmetric state, this statement does not refer to the role of bending in the wrinkle pattern, but insists that bending over the symmetric cap is easy.) Now we further assume small slopes ($|\zeta'(r)| \ll 1$) and the boundary conditions:

$$\sigma_{rr}(W) = \gamma$$
$$\zeta_0'(0) = 0$$
$$\sigma_{rr}(0) = \sigma_{\theta\theta}(0)$$

which impose force balance where the sheet meets the fluid interface, ensure smoothness of the shape and keep stresses well-behaved at the center, respectively. Further manipulation and integration gives a pair of ordinary differential equations for the stress profiles:

$$\partial_{\tilde{r}}\tilde{\sigma}_{rr} = \frac{1}{\tilde{r}}\left(-\tilde{\sigma}_{rr} + \tilde{\sigma}_{\theta\theta}\right), \tag{2.12}$$
$$\partial_{\tilde{r}}\tilde{\sigma}_{\theta\theta} = \frac{1}{\tilde{r}}\left(\tilde{\sigma}_{rr} - \tilde{\sigma}_{\theta\theta}\right) - \alpha\tilde{r}\tilde{\sigma}_{rr}^{-2}, \tag{2.13}$$

in terms of dimensionless variables $\tilde{\sigma} = \sigma/\gamma, \tilde{r} = r/W$. These equations can be numerically solved to predict the stress in radial and hoop directions, as a function of only one parameter, $\alpha = \frac{Y}{2\gamma}\left(\frac{W}{R}\right)^2$, which we had called the confinement. For some range of small α, the stresses are tensile everywhere, as we see in Fig. 2.15(a). At $\alpha = \bar{\alpha}_c \approx 5.16$, $\sigma_{\theta\theta}(W)$ crosses the x-axis and compression is induced at the perimeter.

While the axisymmetric solution predicts the shape and stress profile of the unbuckled ($\alpha < \bar{\alpha}_c$) state, a traditional post-buckling study [36] also uses it as an approximate solution for the wrinkled state, about which linear stability analysis is

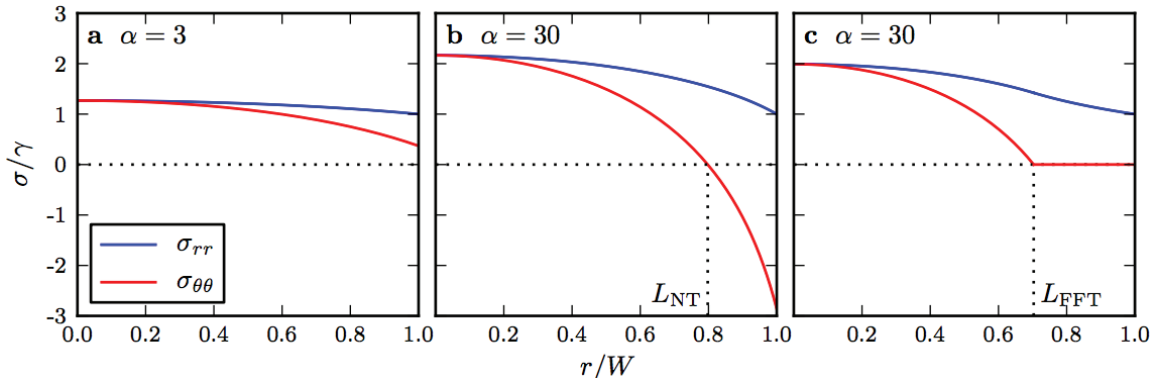

Figure 2.15. Hoop stress and radial stress of the axisymmetric state for both NT and FFT as a function of radius, at $\alpha = 30$. The radius at which the hoop stress $\sigma_{\theta\theta}$ drops to zero is the theoretically predicted wrinkle length L/W.

done. The assumption is that the buckled state still bears the compressive stress that it did before buckling; that the stress field is indifferent to the presence of wrinkles. In the absence of other limiting factors, it should be accurate in the low bendability ($\epsilon^{-1} \approx 1$), near-threshold regime. Fig. 2.15(b) shows a sample unbuckled stress profile for $\alpha = 30$. The radius at which the hoop stress goes negative (compressive) is the NT prediction for the wrinkle length L_{NT}. The numerical prediction as function of confinement ($L_{NT}(\alpha)$) is plotted in Fig. 2.20.

The alternative limit in this analysis supposes that the post-buckled wrinkle pattern can support no compressive stresses whatsoever, in contrast with the NT result). Here, the bending response is seen as a perturbation around the 'membrane limit' of a sheet with no bending modulus [35, 26]. The far-from threshold (FFT) approach [8] proceeds by breaking the sheet into two regions: an unbuckled cap ($r < L_{FFT}$), where the previous solution applies (with some adjustments to the confinement parameter and boundaries), and a wrinkled annulus ($L_{FFT} < r < W$) with completely relaxed hoop stress ($\sigma_{\theta\theta} \geq 0$). Upon finding the radial shape of both portions, the dominant energy terms (from the interface and stretching) for each region are calculated. L_{FFT} is then found by minimizing the total energy with respect to it. The

overall stress profile from the composite solution is shown in Fig. 2.15(c). The wrinkle length prediction, L_{FFT} is noticeably different in the figure, and its dependence on confinement:

$$L(\alpha) = \sqrt[5]{(\bar{\alpha}_c/\alpha)} \tag{2.14}$$

can easily be contrasted with the NT prediction. The FFT predictions should be relevant for the high bendability ($\epsilon^{-1} \ll 1$) limit.

The two approaches also differ in their scaling prediction for wrinkle number, notably in the dependence on thickness through the bendability parameter ϵ^{-1}:

$$\text{NT: } m \sim \epsilon^{-3/8} \tag{2.15}$$

$$\text{FFT: } m \approx k(\alpha)\ \epsilon^{-1/4} \tag{2.16}$$

2.6 Results

Figure 2.16 shows a set of images (I-IV) that from left to right indicate the patterns obtained upon increasing the pressure of the droplet. As the pressure is increased, the sheet first smoothly stretches (I), and then starts wrinkling at the edge (II). The wrinkles grow toward the centre of the sheet and increase modestly in number (III). Further in the progression, some of the wrinkles develop sharper cusp-like features, but the extent of the pattern is still well-defined (IV).

This progression is quantitatively characterized by L/W, the fractional extent of the unwrinkled zone in the interior of the sheet, and $2\pi/m$, the average angle between wrinkles. Both are plotted as functions of the confinement α for a representative sheet with thickness $t = 77$ nm. Figure 2.16 shows that wrinkles emerge at a sharply defined value, α_c. The wrinkles grow inward for $\alpha > \alpha_c$ in excellent agreement with the power law $L/W \sim \alpha^{-1/5}$ from the FFT analysis, over about 1.5 decades in α. Over the same range, the number of wrinkles increases slightly as shown in the lower panel.

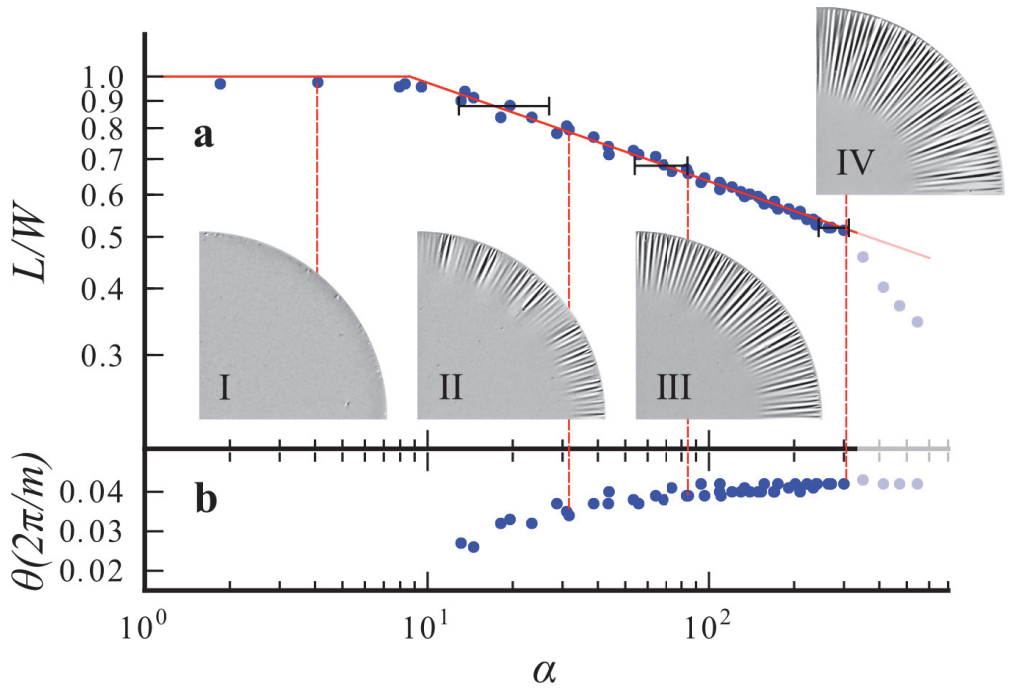

Figure 2.16. (a) Radius of the unwrinkled region, scaled by the radius of the sheet L/W and (b) wrinkle angle θ, for a sheet of thickness $t = 77nm$ and radius $W = 1.5mm$. Consecutive data points are taken by increasing and decreasing the curvature R^{-1} of the drop but the $x-$axis is plotted in terms of the confinement parameter $\alpha \equiv YW^2/\gamma R^2$. A top view of the sheet is shown at several representative values of α. For small α, the sheet stretches to accommodate the curvature. Wrinkles appear beyond a threshold value of α. High confinement values produce a different behavior that will be discussed later.

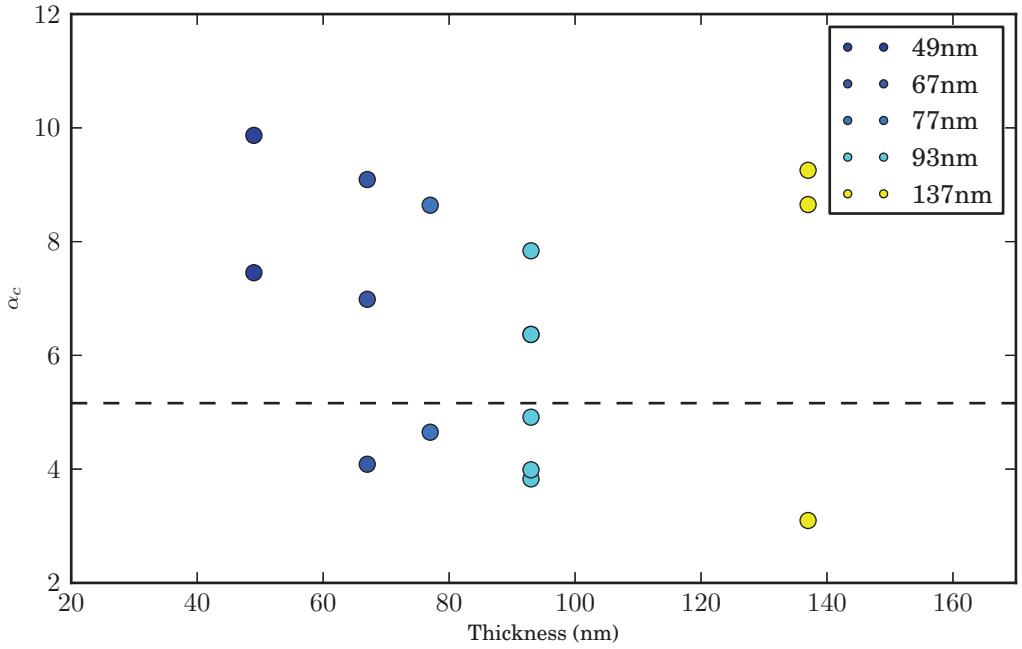

Figure 2.17. Critical confinement from the intercept of best fit power law with $L/W = 1$ as a function of sheet thickness. The values are scattered around the FFT predicted value (for infinite bendability) $\bar{\alpha_c} \approx 5.16$. Any thickness dependence of the critical value is possibly obscured by the effect of irreproducibility between data sets of the same thickness.

The pattern growth is reversible, with the exception of particularly thin ($t < 60nm$) sheets which form folds through self-adhesion at high confinement. Data for each individual sheet was obtained over a cycle of inflation from flat to moderate wrinkling, deflation to flat, then inflation to very high confinement. Hysteresis over this cycle seemed negligible with respect to our length measurement, so data from inward and outward progression was plotted together, as in Fig. 2.16.

For a given data set like that in Fig. 2.16, we identified the portion of $L/W(\alpha)$ which appeared to follow a power law, and performed a least squares fit. The intercept of the fit with 1 ($L/W(\alpha_c) = 1$) gave a value of α_c, as well as the best fit exponent for the set, γ, displayed in Figs. 2.17, 2.18, respectively. From similar plots of L/W for other sheets, we obtained values of α_c that varies from sample to sample, in the

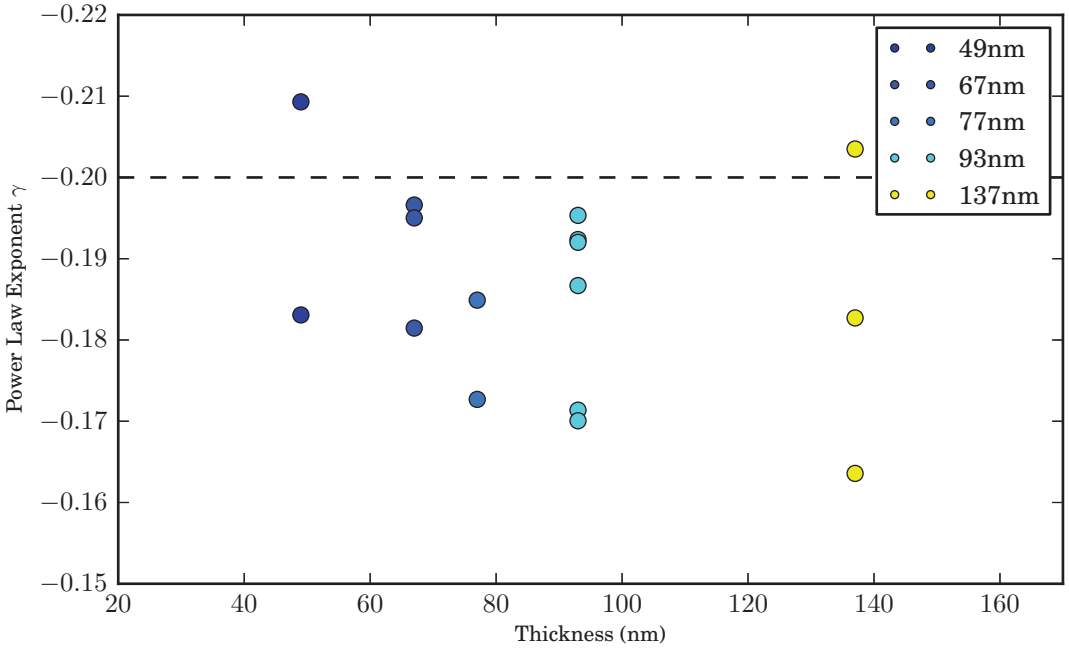

Figure 2.18. Fitted power law exponent $(L/W)^{\gamma}$ to data sets of different thicknesses shows a weak relationship between exponent and thickness. The values are scattered near the FFT predicted value $\gamma = -1/5$ (dashed line).

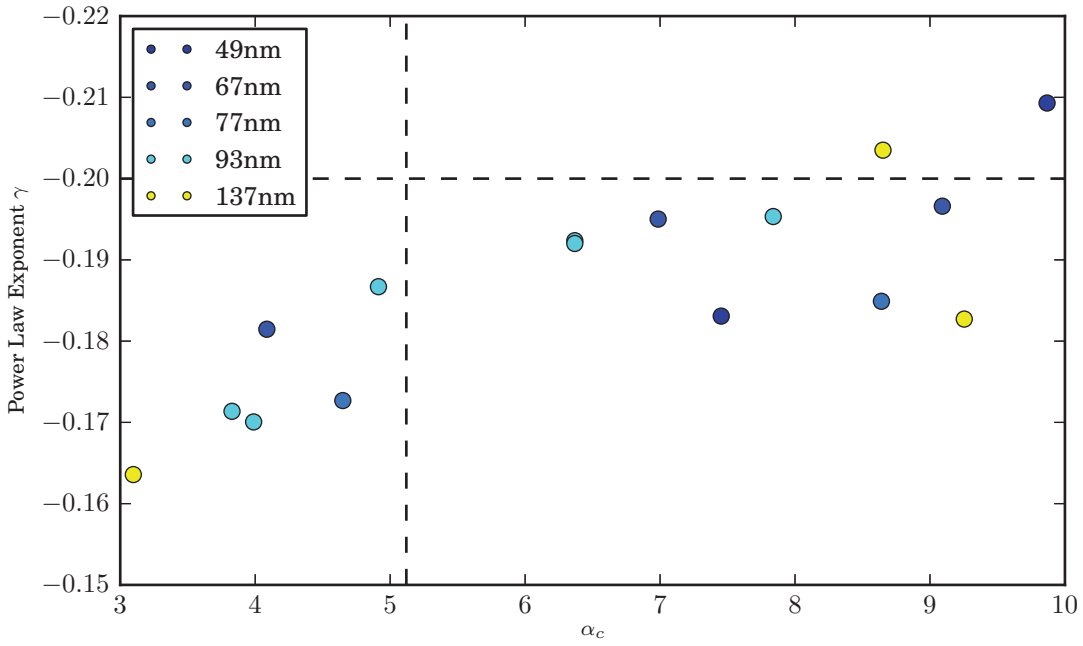

Figure 2.19. Fitted power law exponent $(L/W)^{\gamma}$ now plotted as a function of α_c, shows a visible systematic dependence, though not mediated by the thickness

range of 3 to 10. This range includes the predicted value $\alpha_c \approx 5.16$ and there is no systematic dependence of the measured α_c on t and W. There does appear to be, however, a relationship between α_c and the fitted exponent γ, as shown in Fig. 2.19. The cause of this dependence is not yet understood.

In the upper panel of Figure 2.20, we once again show the extent of the unwrinkled zone, but for a number of sheets of varying thickness and size, now plotted against the scaled confinement parameter α/α_c, where α_c is the measured value at the wrinkling threshold. The data appears to fall away from the power law at large confinement, where crumpled structures like that shown in the inset become pronounced (to be discussed in the next chapter). The data for all thicknesses collapse very well throughout the 'wrinkle regime' described well by the power law, indicating that the length of the wrinkles is independent of the bendability ϵ^{-1}. If there is any regime of α in which the NT behaviour (indicated in Figure 2.20 by a dashed line) is seen, it is in a narrow

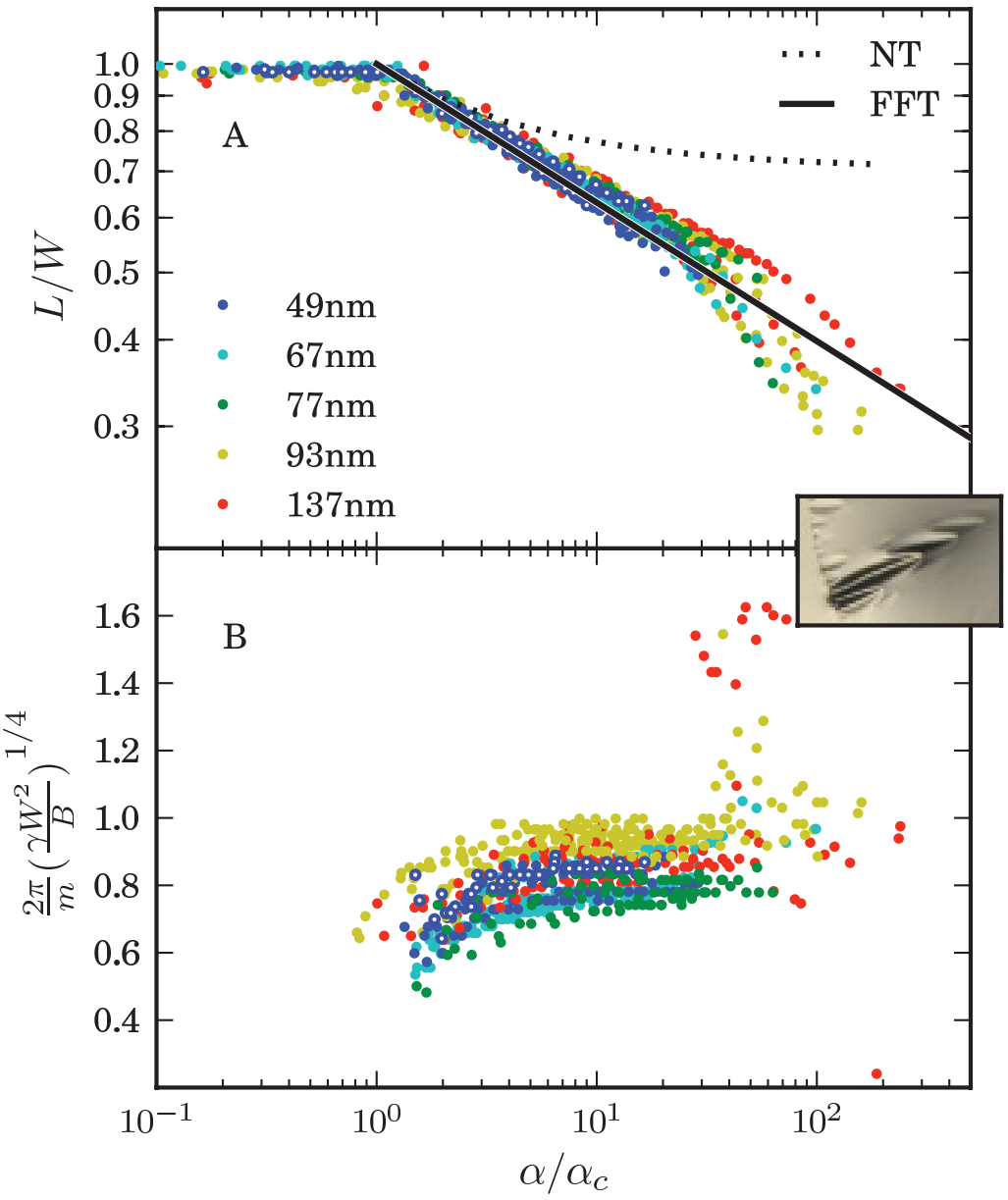

Figure 2.20. (A) Radius of the unwrinkled region, scaled by the radius of the sheet L/W, and (B) scaled wrinkle angle $2\pi/m(W^2/B)^{1/4}$ are shown for a range of thicknesses $(49 - 137nm)$ and two radii $(0.75 - 1.5mm)$. Both are plotted versus the confinement parameter α/α_c, scaled for each sheet to its measured value at the wrinkling threshold. The upper graph shows that the wrinkle size agrees well with the FFT prediction (solid line) over a factor of about 30 in α; the NT prediction (dashed line) departs from the data almost immediately beyond threshold. Crumpled structures at large α as shown in close-up on the right will be discussed in the next chapter. The FFT scaling of the wrinkle number $m \sim t^{1/4}$ reasonably collapses the data.

enough window in near the onset that it is difficult to distinguish from the FFT behavior. This is consistent with the high bendability values of $\epsilon^{-1} \in (2x10^{-7}, 5x10^{-6})$ for the sheets used here. One could argue that local regions (especially toward the tips of the wrinkles), where compressive stress and wrinkle amplitude is very small, should be better characterized by a near-threshold description, but the data gives no indication of this.

The lower panel of Figure 2.20 shows a plot of the wrinkle separation angle $2\pi/m$ scaled by the anticipated FFT dependence of $\epsilon^{-1/4}$, Eq. (2.15). The bendability ϵ^{-1} thus affects the scaling of the wavelengths of the wrinkling pattern [6, 16], while being irrelevant to the stretching energies that control the wrinkle extent [8]. The inset of Fig. 2.20 shows that the predicted NT scaling, $m \sim \epsilon^{-3/8}$. The FFT scaling collapses these angles to within the scatter in the data, while the NT scaling still leaves a systematic thickness dependence in the scaled data. The wrinkle number m appears to vary very little with α. The upward trend at small α likely reflects the method of measuring at $L = 1/2$: as the small wrinkles experience more edge effects, which decreases the wavelength [15].

2.7 Comparison with the Drop on a Sheet

Before we looked into the 'sheet on a drop', a similar experimental [15] and theoretical [37] study was done on a slightly different system: the 'drop on a sheet'. The researchers floated large round sheet of ultra-thin polystyrene film (similar to those referred to in the previous section) on a flat surface of water. In the center, a small drop of water was deposited. The drop applies a downward Laplace pressure on their shared surface, and an upward line tension on the contact line, similar to the situation depicted in Fig. 1.15. The sheet responds by pulling material inward with some axisymmetric, radial tension T, which is greater than the radial tension γ pulling on the outer edge of the film, as illustrated in Fig. 2.21. This tensile mismatch causes

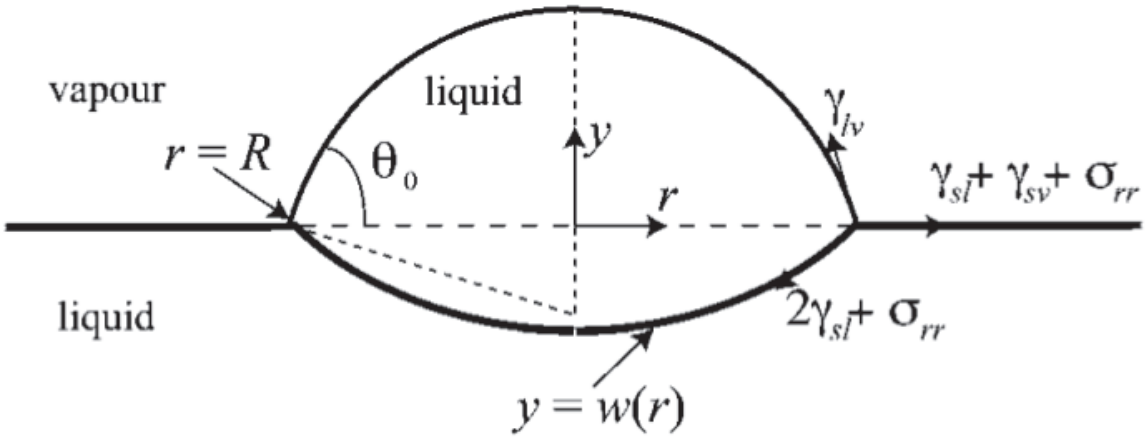

Figure 2.21. Schematic of a drop on a sheet.[37]

a compressive hoop stress around the droplet which can induce buckling [16]. (The region outside the drop is qualitatively equivalent to the planar 'Lamé problem', in which wrinkling is induced in a sheet cut in an annulus because of unequal inner and outer applied tensions [8].) The resulting wrinkle pattern can be seen from above in Fig. 2.22. Again, this pattern has a finite extent, indicating a compressive region in the hoop stress. Far away from the drop, influenced more by the air-water interface, it is reasonable to assume that stresses are tensile. Tension pulling inward at the contact line, however, stretches the sheet inward, inducing a compressive stress in the azimuthal direction. Knowing the inner and outer tensions, they solved for the stresses in an unbuckled state, and supposed that wrinkles extend to the point where the hoop stress of that state changes sign [37]. Their dimensionless number α quantified the confinement produced by the droplet very similar to that of the 'sheet on a drop':

$$\alpha = \frac{Etsin^2\theta}{\gamma}\left(\frac{\gamma}{\gamma'}\right)^3 \tag{2.17}$$

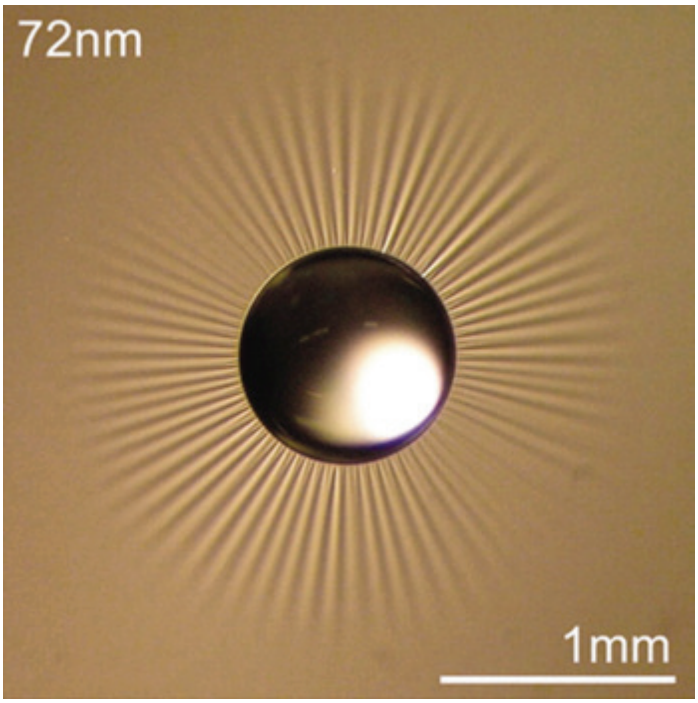

Figure 2.22. Compression on a floating film makes wrinkles.[16]

where γ' denotes the reduced surface tension by surfactant in the reservoir (not the drop). The results for this approach are displayed in Fig. 2.24. From the collapse in the data we see again that the stress profile can be successfully reduced to depend on one dimensionless parameter α. From the disagreement between the data and prediction of the length of the wrinkles, L_w, however, we can see the failure of the near-threshold prediction.

An obvious advancement between the 'drop on a sheet' and 'sheet on a drop' was the application of the new FFT theory, which better described our experimental results. Though it hasn't yet been applied, we expect the method to fix the agreement with the data in the 'drop on a sheet', as they should belong to the high bendability regime. Another comparative advantage of the 'sheet on a drop' setup was the ability to explore the scaling of wrinkle length for values confinement much larger than the threshold value. Experimental limitations confine the study of tensional wrinkling

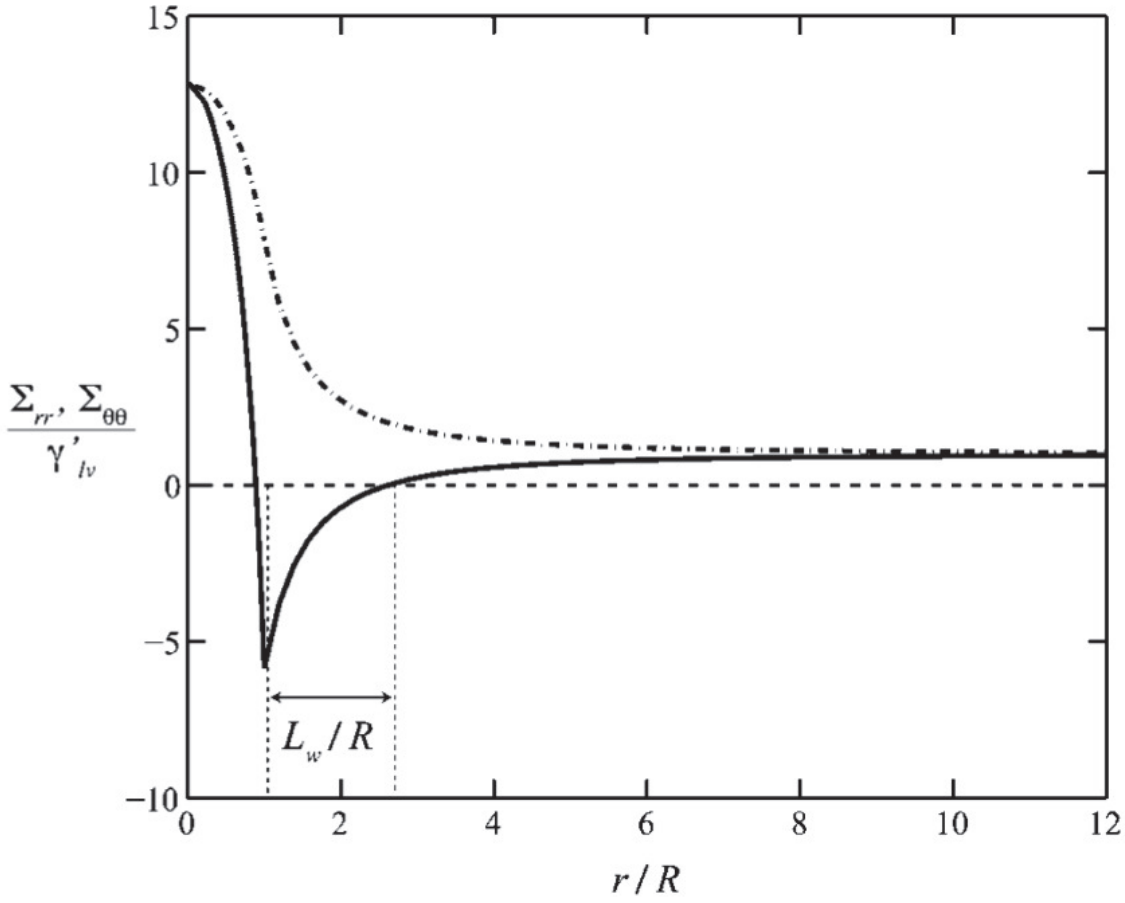

Figure 2.23. Near threshold prediction for the radial (Σ_{rr}) and azimuthal ($\Sigma_{\theta\theta}$) stresses as function of distance from the center of the drop on a sheet.[37]

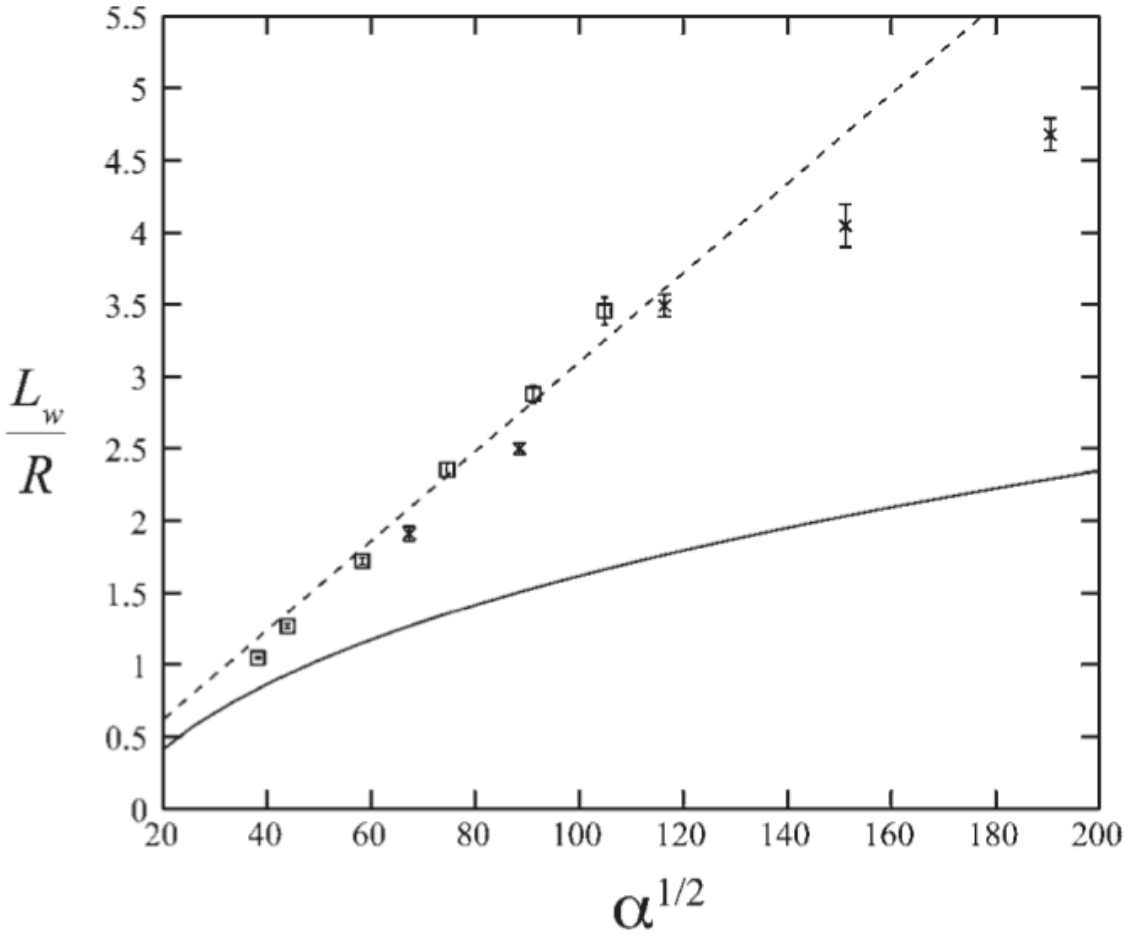

Figure 2.24. Perturbative calculation for wrinkle length. Solid line is theoretical prediction. Points are experimental data.[37]

here, and in the planar, Lamé geometry, to no more than a few times the threshold value [12, 16, 8], whereas we can obtain up to $\alpha/\alpha_c \approx 100$ with the sheet on a drop.

2.8 Summary

In confining it on a frustrating spherical liquid drop of increasing curvature, we allow a circular sheet to choose the onset, extent, and wave number of its broken-symmetry wrinkle pattern. The relevant dimensionless measure of confinement, $\alpha = \frac{Y}{2\gamma}\left(\frac{W}{R}\right)^2$, effectively collapses the measurements of wrinkle extent, which emphatically agrees over a range of 2 decades in the confinement pattern with the far-from-threshold prediction, which applies to the limit of high bendability ($\epsilon = BW^2/\gamma \to 0$) and assumes stress axisymmetry. The observed values for onset of wrinkling are found near the asymptotic critical value corresponding to zero thickness, $\alpha_c \approx \bar{\alpha}_c$. Applicability of the near-threshold prediction is presumably valid in a range so close to the critical value that it cannot be distinguished in the data. Our observations and analysis suggest the schematic phase diagram plotted in Fig. 2.25.

Our results emphasize the importance of the correct application of FFT behaviour to the many modern applications that use sheets of nanoscopic dimensions as mechanical elements. Our experimental and theoretical treatment of the sheet on a drop builds on understanding of previous studies of similar systems and leads to a more complete picture. The wrinkle extent data from the drop on a sheet experiment were properly collapsed by the dimensionless confinement parameter like the one we used, and our findings strongly suggest that FFT analysis for that system is the missing piece necessary for the correct prediction. Similarly, we now have more reason to expect agreement with FFT predictions for the Lamé geometry [8] as soon as the experimental data is available.

It is worth reemphasizing that while the FFT solution for the wrinkled state allowed for a broken symmetry in the deformation field, it continued to assume stress

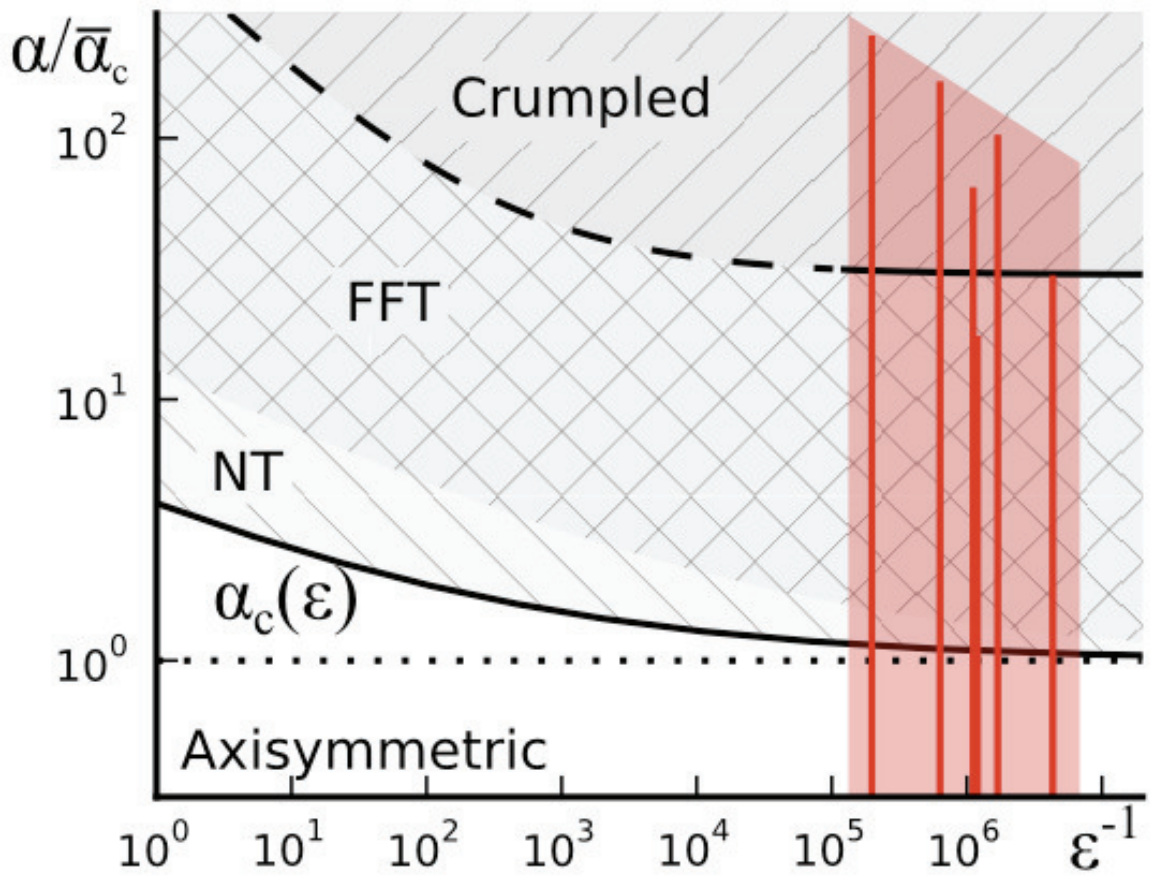

Figure 2.25. A schematic phase diagram for the morphology of an ultrathin sheet on a drop, spanned by the confinement (α) and bendability (ϵ^{-1}) parameters. Similarly to the Lamé set-up (a planar, axisymmetric stretching [8]), the axisymmetric state becomes unstable to wrinkling above a critical confinement $\alpha_c(\epsilon)$ (solid line) that approaches $\bar{\alpha}_c$ as $\epsilon \to 0$. A FFT theory describes the wrinkling pattern for confinement values that become very close to $\alpha_c(\epsilon)$ in the high bendability limit $\epsilon \to 0$. In contrast to the Lamé set-up, the FFT wrinkling pattern transforms into a crumpled shape for sufficiently large confinements $\alpha > \alpha_{crumple}$. The shaded area corresponds to the experimentally probed regime. Individual data sets of various fixed ϵ crossed phases in vertical paths, represented by red lines.

axisymmetry. That the wrinkling transition preserves stress symmetry is perhaps an unexpected result, and it will be important when considering the failure of the wrinkled solution at large confinement.

The other important difference between our system and either of the planar geometries is the existence of an additional morphological transition, indicated in the upper right corner of the phase diagram in Fig. 2.25. This apparently crumpled state will be the subject of the next chapter.

CHAPTER 3

CRUMPLING OF A SHEET ON A DROP

3.1 Introduction

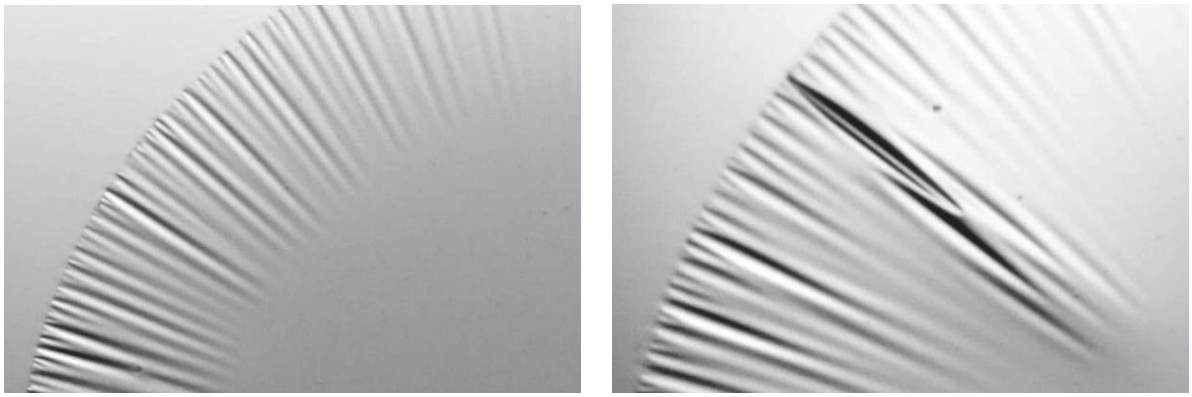

Figure 3.1. Zoomed optical images of a wrinkle pattern (left) and a crumpled feature that emerges from it (right).

In Sec. 1.1.4, we showed that one generic way for a sheet to respond to confinement is by focusing stress into the tips of sharp d-cones. Given the similarities in geometry between Fig. 1.10, in which a d-cone was induced in a sheet by a pencil and cup, and our setup, we could have naively expected the sheet on the drop to fold along seams as its first non-axisymmetric response to the applied curvature. Instead, as discussed in detail in the previous chapter, it first adopts a uniform pattern of wrinkles with tips that smoothly disappear into the featureless region, as depicted on the left of Fig. 3.1. Upon increasing the drop curvature further, however, out of that wrinkle pattern emerges a different type of feature, like the one shown on the right. Here, we see a pronounced valley between two wrinkles end sharply in a cusp-like

shape reminiscent of a d-cone, with some other buckled shapes on either side. These crumpled features further decrease the symmetry of the sheet's shape, as they are distributed less densely around the perimeter. The lower symmetry and presence of pronounced conical shapes qualitatively distinguish the picture on the right from the one on the left, and suggest that the system experiences a wrinkle-to-crumple phase transition. The transformation is not sudden, however, and it is difficult to clearly identify by visual inspection where it occurs.

Because crumpling is a stress-focusing phenomenon [40], we expect to see signs of it in two places: in the failure of the FFT prediction, because it assumes stress axisymmetry, and in other indicators of stress redistribution. In this chapter, we experimentally explore the crumpling transition, attempting to identify a parameter that drives it and an order parameter that characterizes the crumpled state. To this end we first look at a deviation in the trend in the wrinkle length data from the previous chapter. Next, we analyze height maps obtained through optical profilometry, to track the spatial distribution of gaussian curvature, which as we know is geometrically coupled to the stress.

3.2 From Wrinkle Length Data

At high values of α, a deviation is seen from the power law scaling of the length in Fig. 2.20. The onset of this deviation is accompanied by the increasing prominence of crumpled features. We also see that the measurement of the wrinkle length becomes ambiguous because the pattern is characterized by more than one length scale. In Fig. 3.2, we reproduced the data from Fig. 2.16, including an enlarged image of the most crumpled sheet in that run. The middle two images show a wrinkle pattern with one well-defined length. For all the data until the deviation at $\alpha \approx 300$, the automated method of length measurement described in Sec. 2.4.3 obtained values in clear agreement with eye estimates. After that point, however, it becomes increasingly

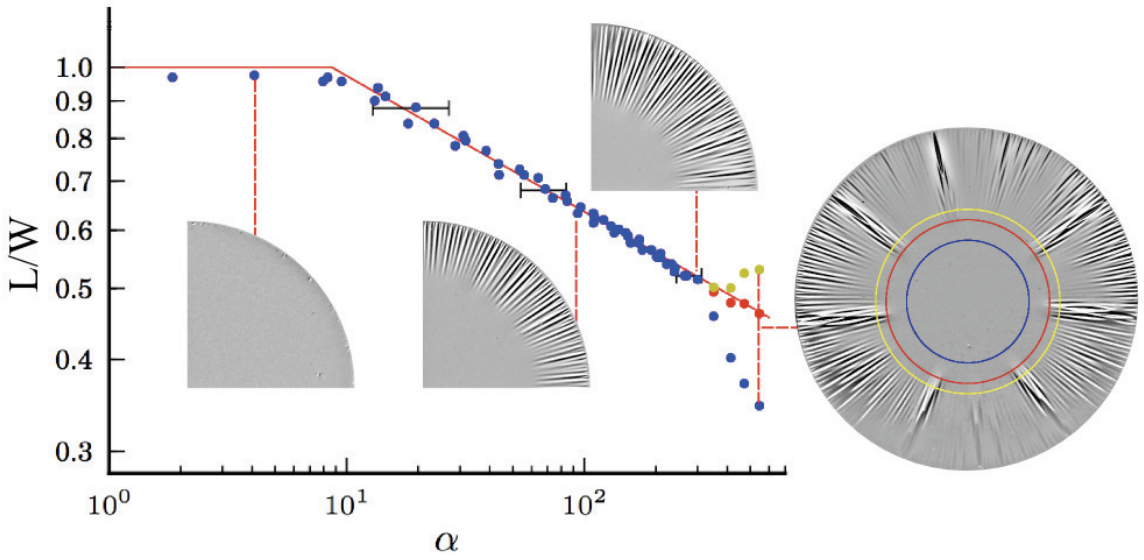

Figure 3.2. Radius of the unwrinkled region, scaled by the radius of the sheet L/W for a sheet of thickness $t = 77nm$ and radius $W = 1.5mm$ (Data same as that of Fig. 2.16). Consecutive data points are taken by increasing and decreasing the curvature R^{-1} of the drop and the $x-$axis is plotted in terms of α. A top view of the sheet is shown at several representative values of α. For moderate values of $\alpha > \alpha_c$, wrinkles of a consistent length extend inward from the edge. Beyond another threshold value of α, sharp cusps extend inward (red), intermediate wrinkles recede outward (yellow), and the value obtained through image analysis described in Sec. 2.4.3 becomes incompatible with a visual estimate (blue).

unclear which length characterizes the pattern. The image of the most crumpled shape on the far right shows three plausible choices of a characteristic length for the pattern:

(*i*) First, we could track the most uniformly wrinkled portion of the no-longer-uniform shape, as the yellow line has attempted to do. This is a little ambiguous here, even though this sample is more symmetric than average, but the behavior of these wrinkles is interesting, as they seem to recede as the crumpled features dominate.

(*ii*) Second, we could measure to the tip of the longest visible feature. From this method, for this sample, the trend appears to progress unchanged. This choice is labeled in red.

(*iii*) Third, we could apply the algorithm from Sec. 2.4.3, from which we obtained all the previous data points for the uniform wrinkle pattern. This option is labeled

in blue, and it clearly disagrees with a visual estimate of the length of the wrinkled features. The algorithm still operates as designed: it looks for the radius at which the deviation in intensity around the circle falls below the threshold value. The difference is that that radius is now determined by the end of a more subtly varying, less visible structure, and not the end of visible wrinkle tips.

The simple fact that these three methods agree until a point, then disagree, is an indication that the state has changed. Because of asymmetries due to common imperfections in the samples, method (*i*) was difficult. Instead, we located the point at which (*ii*) and (*iii*) start to disagree. These are plotted as large circles on the length data in the top of Fig. 3.3. At the bottom are the lengths and values of α at which the transition, measured in this way, occurs. The points are spread over a range of α (and α/α_c), but more tightly centered around a length of approximately half the sheet's radius. Fig. 3.4 shows a weak thickness dependence for these points, as well as significant variation between samples of the same thickness.

According to the prediction for wrinkle length, $L = L(\alpha)$, so it is unclear why the transition should occur for a given L but not α, though the spread in slopes was apparent in Fig. 2.18. Whatever the cause of this variation, the sheet apparently waits for the appropriate length, rather than value of confinement, before crumpling. Recall that α, in determining the stress profile of the axisymmetric state in the membrane limit, is set by both geometric (W/R) and mechanical (Y/γ) considerations. For the onset of crumpling to occur at a particular length suggests that geometry plays a more direct role than it had in the smooth-to-wrinkle transition. To better understand the transition, however, we would like to have a clear measure of the parameter which drives it, as α might not serve this purpose any more. Also, as the wrinkle extent, L/W, served for the wrinkled state, we would like to have a measurable order parameter to quantify the transition into the crumpled state.

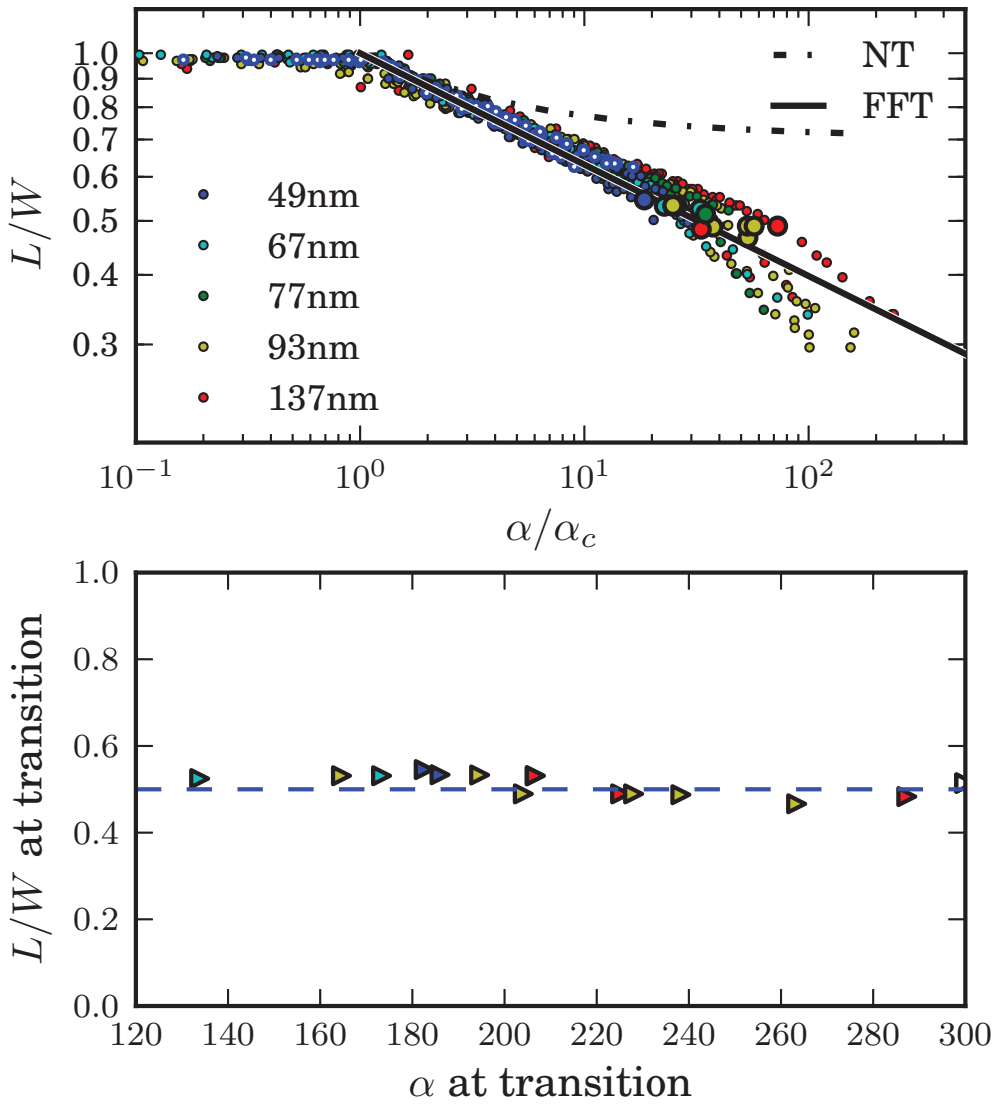

Figure 3.3. (Top) Radius of the unwrinkled region, scaled by the radius of the sheet L/W for a sheets of various thickness. Beginning of the transition labeled by large circles. (Bottom) Transition points plotted linearly against α. Transition covers a significant range in α independent of thickness but is centered around $L \approx W/2$

The smooth-to-wrinkle transition was characterized by a breaking of an axisymmetric shape and, notably, preservation of an axisymmetric stress field. As crumpling is most fundamentally a stress focusing phenomenon [40], we supposed that the crum-

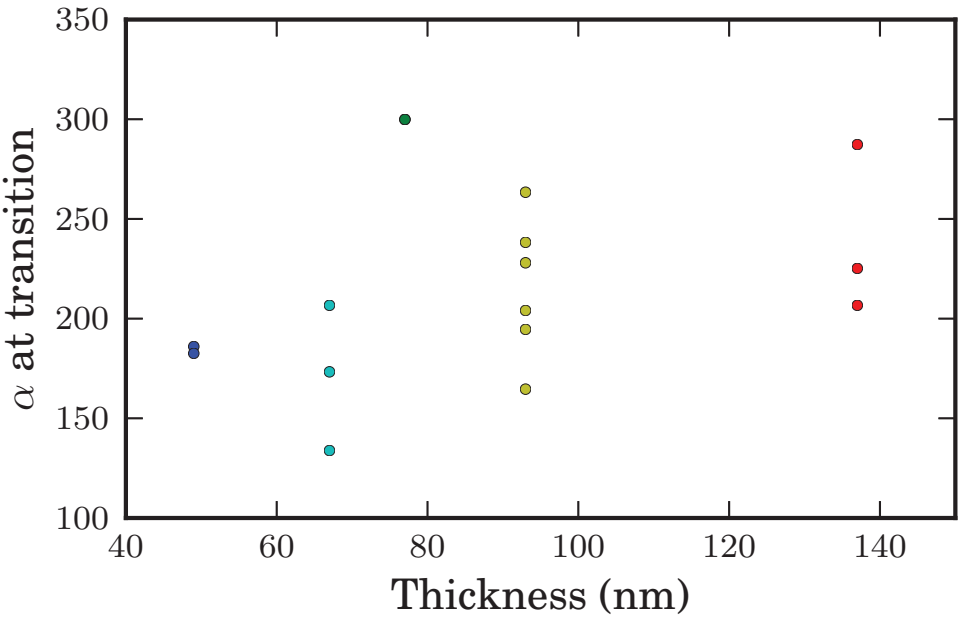

Figure 3.4. α at the transition point, measured by the appearance of new length scales, as a function of sheet thickness, for different samples.

pling transition is a primary symmetry breaking of the stress field (as opposed to a secondary symmetry breaking of shape alone), preferred at large curvature to relax elastic energy. In the next section, we will try to more directly verify this hypothesis.

3.3 Crumpling via Curvature Measurements

First of all, we don't have direct access to stress in the sheet. However, in Sec. 1.1.2, we discussed how gaussian curvature necessarily creates in-plane strain, and therefore stress in the sheet. Although the gaussian curvature only accounts for one contribution to in-plane strain, we remember that it is the primary cause of any stress in the sheet, beyond the initial planar stretching from surface tension. We will now look at the gaussian curvature distribution on the sheet as a proxy for tracking the stress distribution.

3.3.1 Measurement and Analysis

Fig. 3.5 shows the modification of our experimental setup to obtain height maps of the central portion of the sheet on a drop. We used glycerol instead of water to create the curved meniscus in order to damp surface vibrations that strongly affect the sensitive height measurements[1]. The setup from the previous chapter was simply placed under a Zygo NewView 7300 optical prolometer with 10x and 50x Mirau objectives, which replaced the top-view optical imaging.

The profilometer sends white light through a beam splitter. A portion of the light is sent through the objective, reflected off the sample surface back into the objective, and recombined with the reference portion to form an image. Any variation in optical path length results in a fringe pattern in the recombined image. For better lateral resolution and depth, a sequence of such images are taken as the whole optical setup is slowly vertically moved. The images are pieced together and from them is extracted a complete height map of the sample. Because the measurement depends on light reflecting back into the objective from the sample, data at points of local slope beyond a maximum value are lost, and they can be seen as white pixels in the maps below. Looking at the maximum values of slope magnitude for our data, this cutoff appears to be $\approx 9°$. The lateral resolution for the 10x objective we used was 2.2 μm and the field of view was 1.1x1.4mm. The specifications for the device claim vertical resolution of $< 0.1nm$.

Even using glycerol, vibrations were problematic. Data collection at night proved more successful, as either ventilation or footfalls in the building are decreased. Even in the cleanest data, evidence of surface vibration could be seen, at least in the higher order calculations, such as gaussian curvature.

---

[1]Switching to glycerol created some issues with the pressure measurement that are discussed in Appendix A

Individual height maps were saved as text files in an array of 480x640 elements for further analysis offline by our own code written in Python.

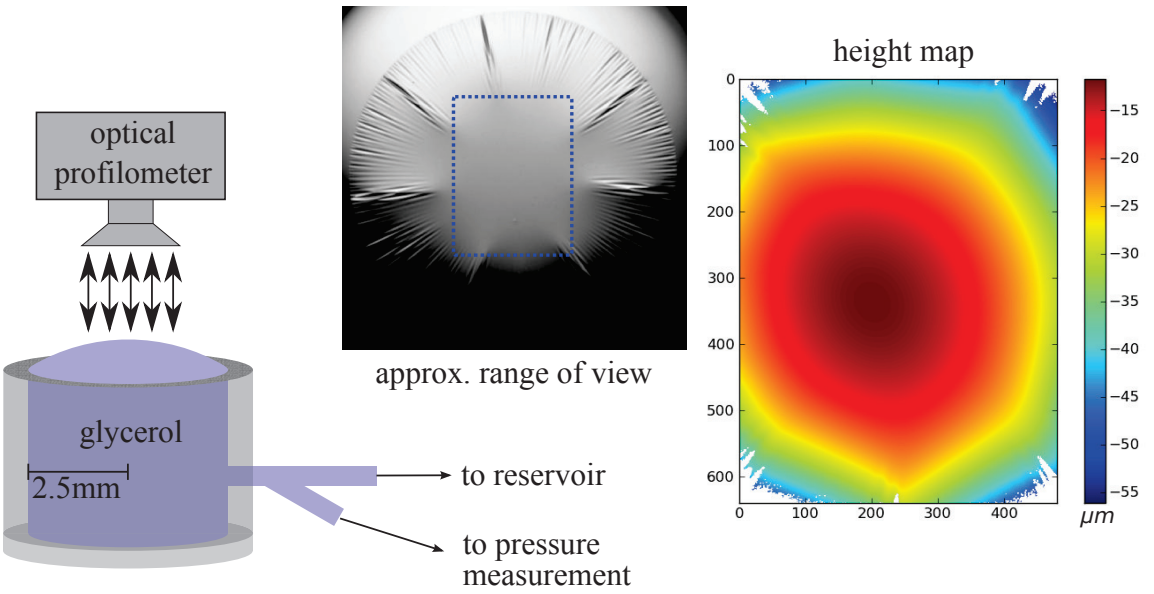

Figure 3.5. (Left) Sheet on a drop setup with optical profilometer to measure height maps of the sheet. (Middle) Approximate lateral range of view under the profilometer, shown on a sample optical image of a crumpled sheet. (Right) Sample height data taken of the center of a crumpled sheet. White points indicate slopes beyond which the reflected light does not return to the profilometer's objective lens.

Sample preparation: spin-coating, cutting, and sheet transferring largely followed the methods described in Sec. 2.4. Glycerol alone could not be used to float the sheet from the substrate, so a small layer of water was poured over a cup of glycerol before dipping the slide with the cut sheet. The liquid transfered with the sheet to the tube, then, was not pure glycerol, which created some uncertainty in the surface tension, discussed in Appendix A.

Irregularities in the reflectivity of the surface occasionally produced spikes in the data. These were removed by high-pass filtering the maps and removing points beyond a threshold value. The data were then smoothed with a gaussian filter. Profiles of the surface were compared before and after this procedure to ensure that the shape was negligibly affected.

One direct method of obtaining a local value of gaussian curvature from the height map is to fit circles to vertical slices of the surface at different angles. The maximum and minimum values, $1/R_1, 1/R_2$ are the principle curvatures which, multiplied, give the gaussian curvature $\kappa_G = \frac{1}{R_1 R_2}$. This method is computationally very expensive.

An alternative method makes use of the tensor form of the curvature C, as we saw in Eq. 1.16 in Sec. 1.1.2, whose determinant was defined as the gaussian curvature. Its elements are derivatives of the surface $\mathbf{R}$ in orthogonal material coordinates s_x and s_y, but we need to express them in terms of the height map $h(x, y)$ in its own vertical and horizontal directions. As long as the sheet is mostly horizontal such that its slope is finite everywhere, the derivatives can be rescaled:

$$\frac{d\mathbf{R}}{ds_x} = \frac{1}{\sqrt{1 + \left(\frac{dh}{dx}\right)^2}} \frac{dh}{dx}, \tag{3.1}$$

so that the curvature becomes:

$$C = \begin{pmatrix} \frac{d^2\mathbf{R}}{ds_x^2} & \frac{d^2\mathbf{R}}{ds_y ds_x} \\ \frac{d^2\mathbf{R}}{ds_y ds_x} & \frac{d^2\mathbf{R}}{ds_y^2} \end{pmatrix} = \begin{pmatrix} \frac{1}{1+\left(\frac{dh}{dx}\right)^2} \frac{d^2h}{dx^2} & \frac{1}{\sqrt{1+\left(\frac{dh}{dx}\right)^2}} \frac{1}{\sqrt{1+\left(\frac{dh}{dy}\right)^2}} \frac{d^2h}{dydx} \\ \frac{1}{\sqrt{1+\left(\frac{dh}{dx}\right)^2}} \frac{1}{\sqrt{1+\left(\frac{dh}{dy}\right)^2}} \frac{d^2h}{dydx} & \frac{1}{1+\left(\frac{dh}{dy}\right)^2} \frac{d^2h}{dy^2} \end{pmatrix} \tag{3.2}$$

Now, given the derivatives at a location x, y, we can calculate the gaussian and mean curvature by taking the determinant and trace of the matrix, respectively. The real benefit of this method is that we can take advantage of the fast array manipulation in Python. Instead of computing the derivatives and assembling the tensor components for each x, y element of the MxN height map, we can perform the operations on entire maps at once. To put together the curvature tensor then, we need an MxN map for each of the derivatives of h. The analogous fast alternative of computing the derivative maps is to convolve with a derivative kernel. We used a 3x3

'Scharr' kernel for each direction[2][32]:

$$\frac{dh}{dx}(x,y) = \frac{1}{32}\begin{bmatrix} -3 & 0 & 3 \\ -10 & 0 & 10 \\ -3 & 0 & 3 \end{bmatrix} * h(x,y), \tag{3.3}$$

$$\frac{dh}{dy}(x,y) = \frac{1}{32}\begin{bmatrix} 3 & 10 & 3 \\ 0 & 0 & 0 \\ -3 & -10 & -3 \end{bmatrix} * h(x,y) \tag{3.4}$$

The second derivatives were obtained by convolving the result with the appropriate kernel again. Then we put the components of Eq. 3.2 together.

3.3.2 Results

A representative map of gaussian curvature for a highly crumpled sheet can be seen in the bottom right of Fig. 3.6. Above it is an optical image of a similar sheet of the same thickness and confinement, taken from the previous chapter. The dashed blue box indicates roughly the range of view of the height maps, which are restricted by the lowest available magnification of the optical profilometer. On its left is an 'optical' image from the same profilometer data that produced the curvature map. Its calculation is based on the refracting mechanism by which we see intensity variation in the top-view images of the wrinkles: that the decrease in intensity is proportional to the slope of the surface (relative to the angle of incident light, which is tilted). By comparing the curvature map with the optical image, we see that structures in the gaussian curvature map extend farther inward than the longest visible feature in the optical images. This is already an important observation because the FFT analysis of

[2]A more standard 'Sobel' kernel would have worked just as well for calculating derivatives; the 'Scharr' kernel was chosen for improved rotational symmetry, a detail which turned out to be small enough not to be noticed in our results

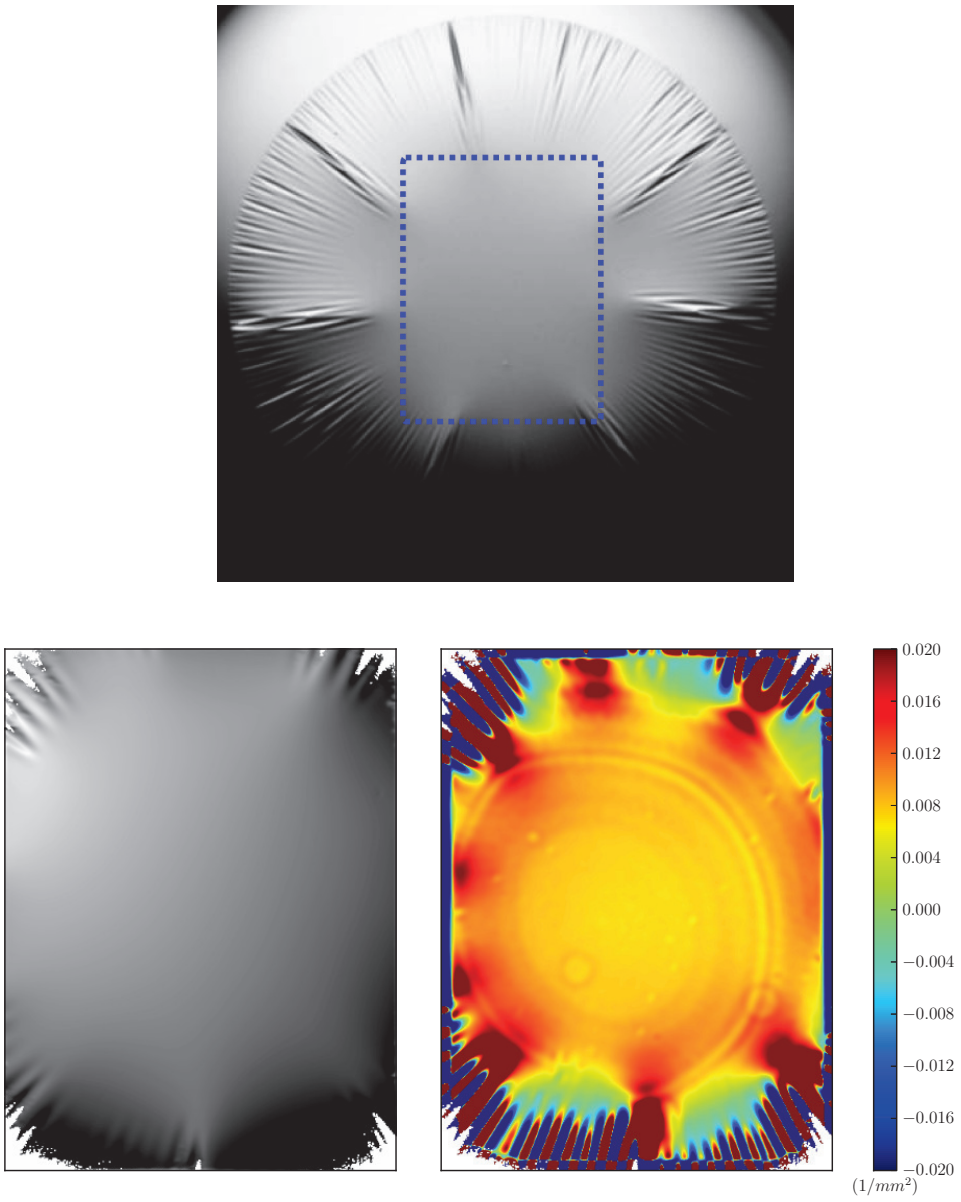

Figure 3.6. (Top) Top-view of a crumpled sheet on a droplet, from camera setup described in chapter 2. The dashed rectangle indicates the range and view of the profilometer data. (Bottom) Two manipulations of one height map of a similarly crumpled sheet: (Right) Gaussian curvature map. (Left) Simulated 'optical' image calculated from total slope of the surface. Structures in the (higher order) gaussian curvature map extend inward where nothing is visible in the optical images.

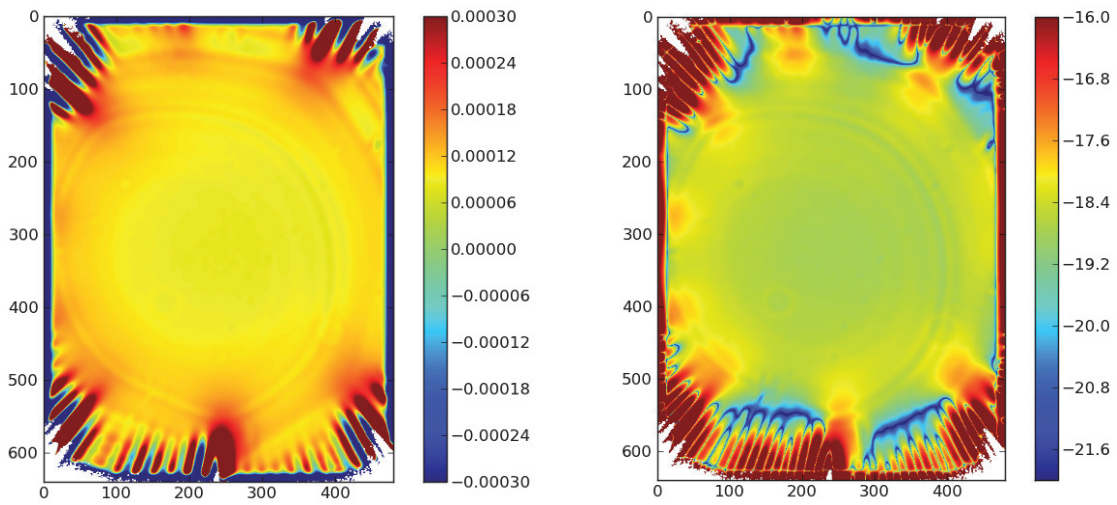

Figure 3.7. Two alternative displays of curvature: Mean curvature of the sheet in Fig. 3.6 (Left), and the gaussian curvature of that sheet plotted with a log scale (Right).

the wrinkled state assumed axisymmetry in all quantities within the wrinkle length $r < L$.

Another important qualitative observation is that the symmetry in the curvature is strongly broken near the pronounced crumpled features. This was suggested by the images, but to the extent that the gaussian curvature represents the stress, it more directly reinforces our hypothesis that stress focusing is responsible for the failure of the FFT prediction across a crumpling transition. The gradual increase in asymmetry is apparent in the sequence of increasing curvature in Fig. 3.8. Again, the smoothness of the transition can be seen as the number of focused sites gradually decreases and individual spots become more pronounced.

Given the observations so far, it would be reasonable to suppose the transition is caused by the formation of individual stress-focusing d-cones. The optical images didn't allow a direct measure of the shape, though we could see in them the appearance of cusp-like features, sometimes within the range of moderate confinement where the

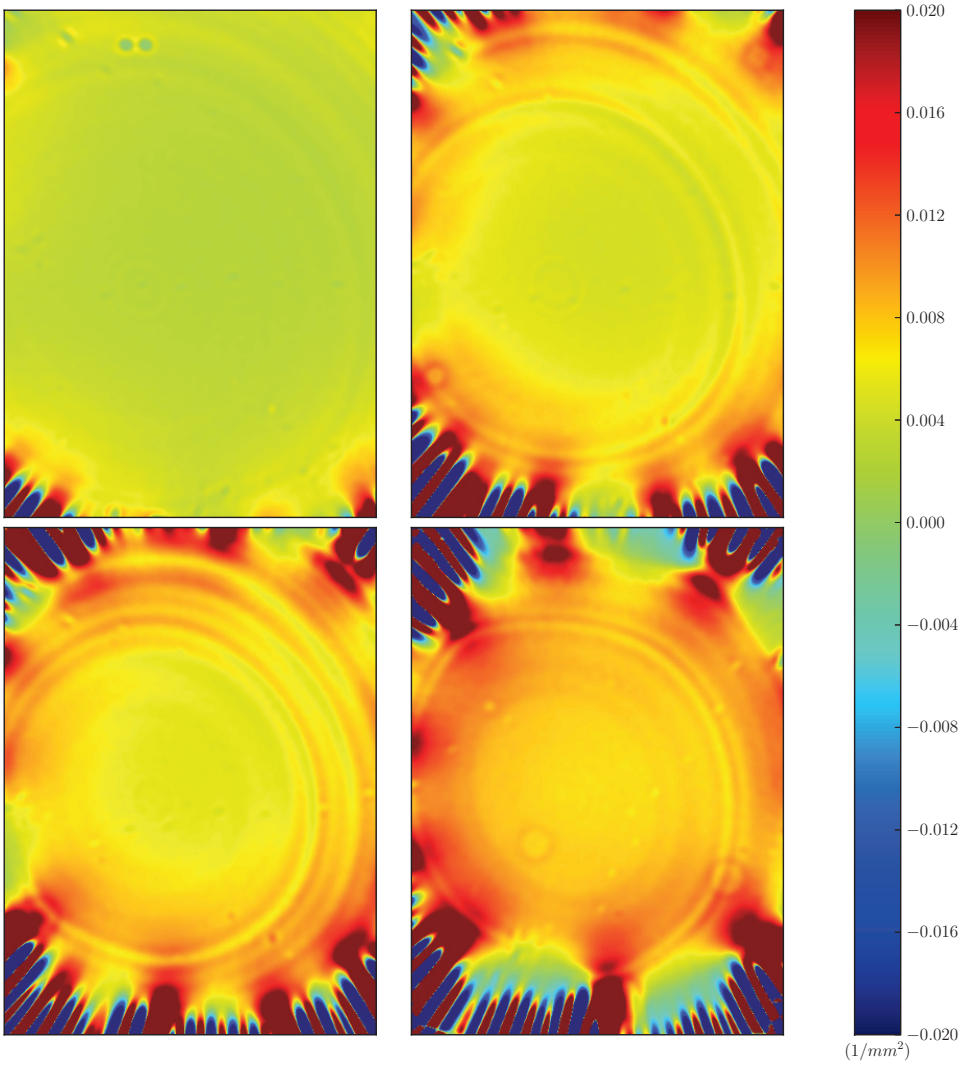

Figure 3.8. Gaussian curvature distribution near the center of a $138nm$ sheet, for values of $\alpha \approx 140, 350, 470, 710$

wrinkle length was accurately predicted. With the profilometer, we can measure how a wrinkled shape evolves into a cusped shape. A cusp can be identified by the its large positive gaussian curvature on one side and large negative gaussian curvature on the other, in contrast with a wrinkle tip, whose large positive or negative value monotonically decays on the side facing toward the center. All such cusps we have witnessed in the sheet point in the same direction, with the positive (sharp peak) side inward and negative (sharp valley) pointing outward from the center. In a gaussian curvature map, this looks like a large negative finger turning into a large positive finger before gradually dropping off as we follow it inward from the edge of the sheet. This can be distinguished from a smooth wrinkle valley, which starts very negative and gradually increases toward to the background value of the sheet center.

The local process of creating cusps is observed in maps zoomed in on wrinkle tips while slightly varying the pressure, as in Fig. 3.9. Positive tips (peaks) and negative tips (valleys) initially lengthen inward together. In front of two neighboring peaks, the positive curvature extends beyond the end of the valley between them, eventually joining the two peaks, when the valley is pushed outward. From the insets of the figure, we can see that, toward the beginning of the process, the curvature along the valley changed nearly monotonically from slightly positive to negative moving away from the center, whereas at the end, the curvature reaches a positive maximum before dropping negative sharply over the tip of the cusp.

The cusps we see here are qualitatively the same shape as d-cones. According to our description in Sec. 1.1.4, however, as a developable shape, a d-cone should have zero gaussian curvature everywhere but the tip, where the positive and negative curvature-dipole is focused into a region of the order of the sheet thickness. Fig. 3.10 displays the same sequence, but on a logarithmic scale to more clearly see the magnitudes of gaussian curvature. Throughout the sequence, we see the curvature is only slightly more pronounced near the cusps, and not particularly at their tips. This sug-

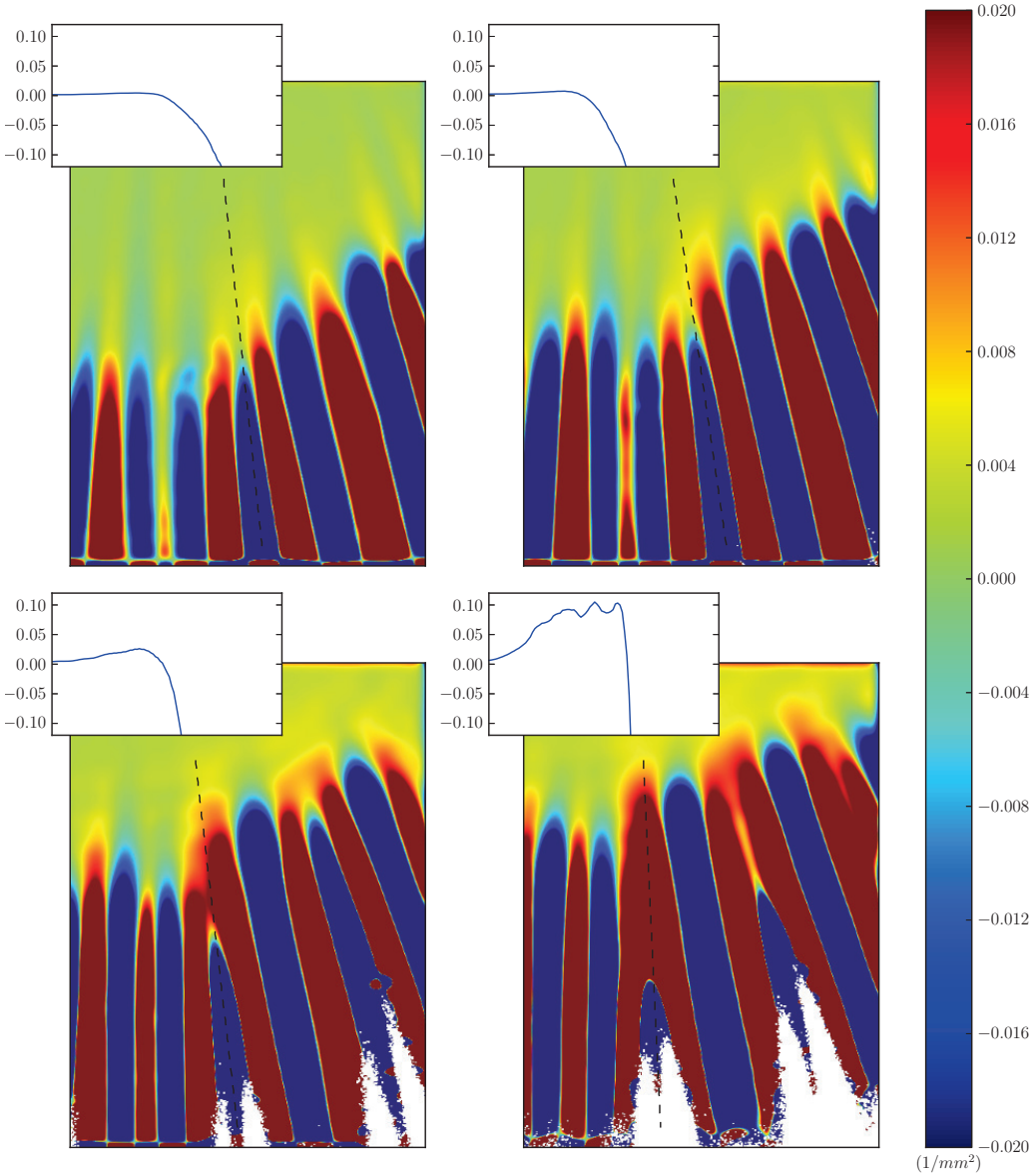

Figure 3.9. Neighboring wrinkles near the edge of a 138nm thick sheet merge to form cusps. Displayed is the local gaussian curvature, displayed with linear scale. The insets show the gaussian curvature values along cuts (dashed lines), moving outward from the center of the sheet. Large positive and negative regions are saturated to emphasize the qualitative shape of the features, and make visible the finer variation at the tips. The horizontal extent of the images is 5.3mm and $\alpha = 50, 80, 130, 180$. From the wrinkle length measurements, the transition for this thickness occurred at $200 < \alpha < 290$.

gests that, though the roughly conical shape emerges from the joining of neighboring wrinkles, stresses are not focusing at the same time. Tension likely plays a significant role here in smoothing sharply curved features, as has been studied in Ref. [33].

Another important observation is that this emergence of d-cone-like shapes occurs entirely within the wrinkle regime ($50 < \alpha < 180$), where wrinkle length predictions were still accurate for this thickness, and where the pattern is still characterized by a single length[3]. Formation of visible cusps within the wrinkle regime was also qualitatively observed in the previous optical measurements. This emphasizes that the appearance of conical features does not necessarily indicate significant stress focusing or a transition to a global crumpled state.

The sequence in Fig. 3.8 shows a different process by which the positive curvature from large *distant* crumples join, such that the entire wrinkle pattern between them is pushed away, much like the single valley did between neighboring wrinkle tips. Between the large cones is a region of significantly less positive gaussian curvature. This is reminiscent of a 'ridge': the stretched, saddle-like region between two d-cones in a free sheet. In a true ridge, negative gaussian curvature is a consequence of relaxing the bending energy along the crease between the d-cones [40, 25]. Despite the resemblance, the function of the low curvature regions is probably different, considering that bending energy has proven negligible compared to stretching and capillarity in determining the shape so far.

If stresses redistribute upon crumpling, one might expect that its magnitude changes even far away from the focused regions. It seemed plausible that focusing positive gaussian curvature in small regions would relax the stress elsewhere, allowing the sheet to flatten there. The notion that the the overall progression was from from

[3]These individual values of α have a significant uncertainty, as discussed in Appendix A, but represent the upper bound according to their corresponding pressure calibration measurement, like the one shown in Fig. A.1.

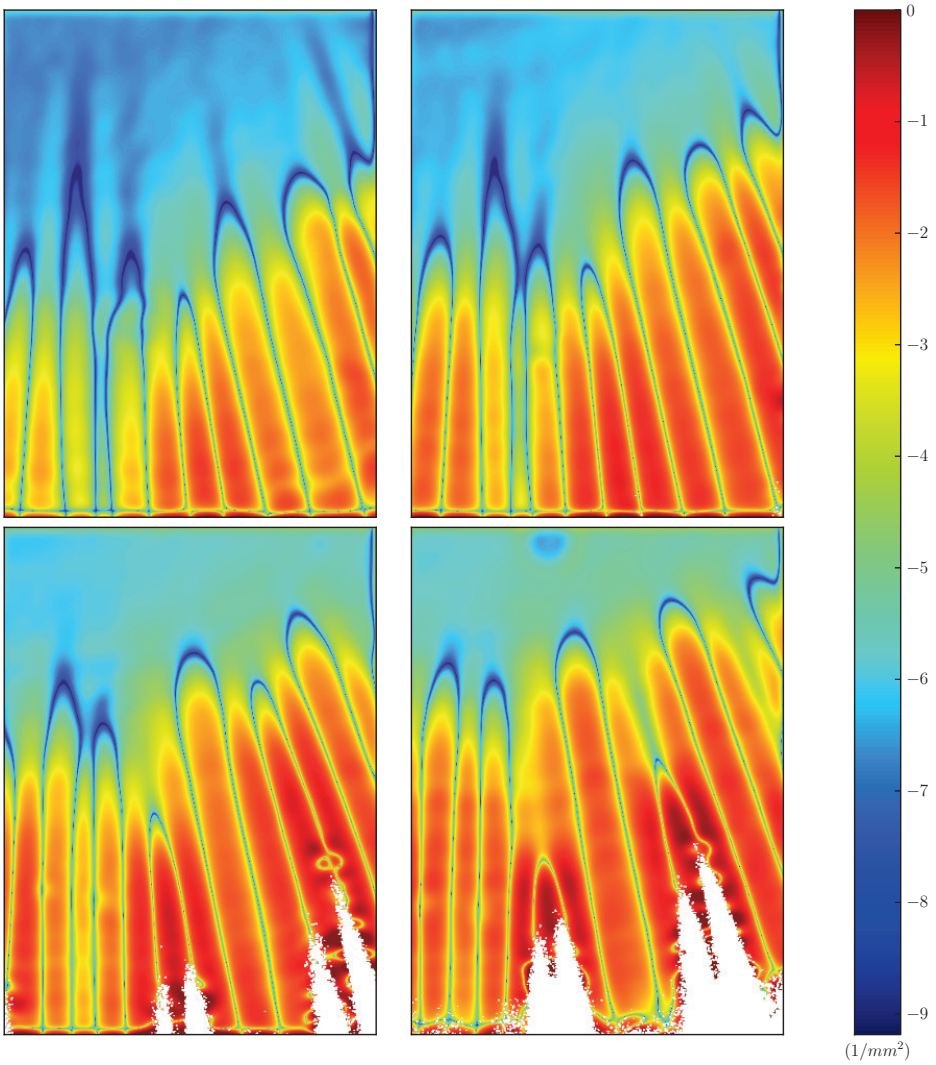

Figure 3.10. The same sequence from Fig. 3.9 of cusp formation. The absolute value of gaussian curvature is displayed with a logarithmic scale to see the relative magnitude of curvature in the wrinkles vs. the cusps. In the last image of a well-defined cusp, gaussian curvature is only slightly focused in a region around the tip. The little ribbon of small curvature at some tips are where the value crosses from negative to positive.

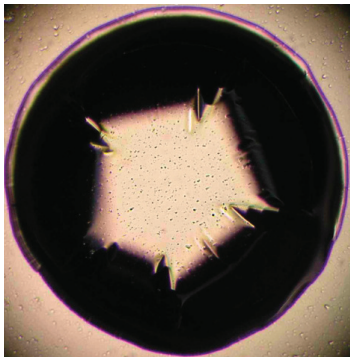

Figure 3.11. Sharp slope contrast image of crumpled sheet appears to be flat on top, with folds around sharp corners.

flat disk to round cap to 'table-top', resembling the sheet depicted in Fig. 3.11 would imply that the curvature near the middle increased for some range of confinement, then decreased. Such a change in direction of a simple geometric quantity would certainly be a compelling indicator for a global state transition.

As we did near the wrinkle tip, for several thicknesses, we measured the curvature in the central, unwrinkled region as a function of pressure. In all runs, the pressure was increased and then decreased. Fig. 3.12 shows the gaussian curvature averaged over a small region (radius = 20 pixels = 44 μm) in the center of the sheet for different thicknesses as a function of applied pressure. Clearly, the observation based on images such as in Fig. 3.11 is misleading. That is, the curvature in the middle continues to increase monotonically as pressure is increased.

A change in the trend in the gaussian curvature at the center of the sheet with increasing confinement could be an alternative indicator that a global change has occurred, and that a new solution is preferred over the wrinkled state. In Fig. 3.13 and Fig. 3.14, we compare the data with a FFT prediction, on linear and log scales. The curvature is now scaled by the radius of the drop (γ/P), and the confinement also non-dimensionalized as α. Dashed lines are power law fits to individual runs. Here, the downward trend shows that, although the curvature of the sheet is increasing, it

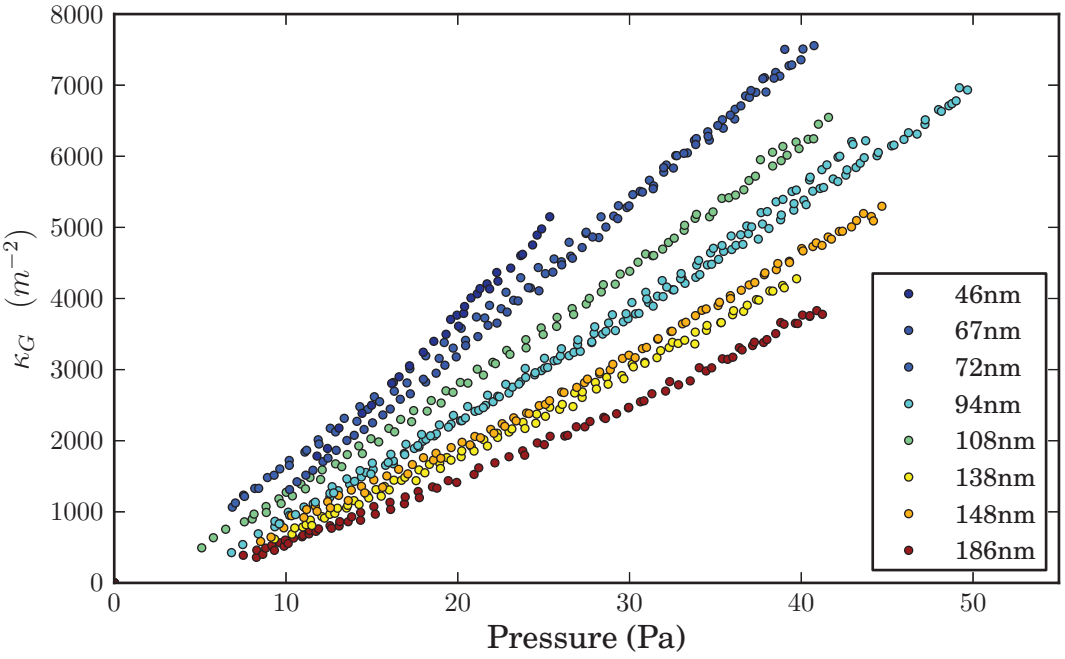

Figure 3.12. Gaussian curvature κ_G averaged a small region at the center as a function of pressure under the drop (circles)

is increasing more slowly than the curvature of the drop. This trend probably gave a false impression that the top of the sheet was flattening.

The prediction is based on FFT results and therefore treats the sheet again as an axisymmetric cap of radius L, surrounded by an annulus with zero compressive stress. Using the boundary condition at the outer edge of the sheet, $\sigma_{rr}(W) = \gamma$ and force balance inside the annulus ($r < L$), we find the radial tension: $\sigma_{rr}(r) = \gamma W/r$. Now we can consider the cap as a sheet of radius L, some effective curvature R_{eff} (approximately constant under the sheet), subject to a surface tension $\gamma W/L$. Because the wrinkle tips at $r = L$ are critically confined by definition, α_c can be expressed:

$$\alpha_c = \frac{Y}{\gamma'}\left(\frac{L}{R_{eff}}\right)^2 = \frac{Y}{\gamma}\frac{L}{W}\left(\frac{L}{R_{eff}}\right)^2 \tag{3.5}$$

Now, introducing α and recognizing the wrinkle length power law $L/W = \left(\frac{\alpha}{\alpha_c}\right)^{-1/5}$:

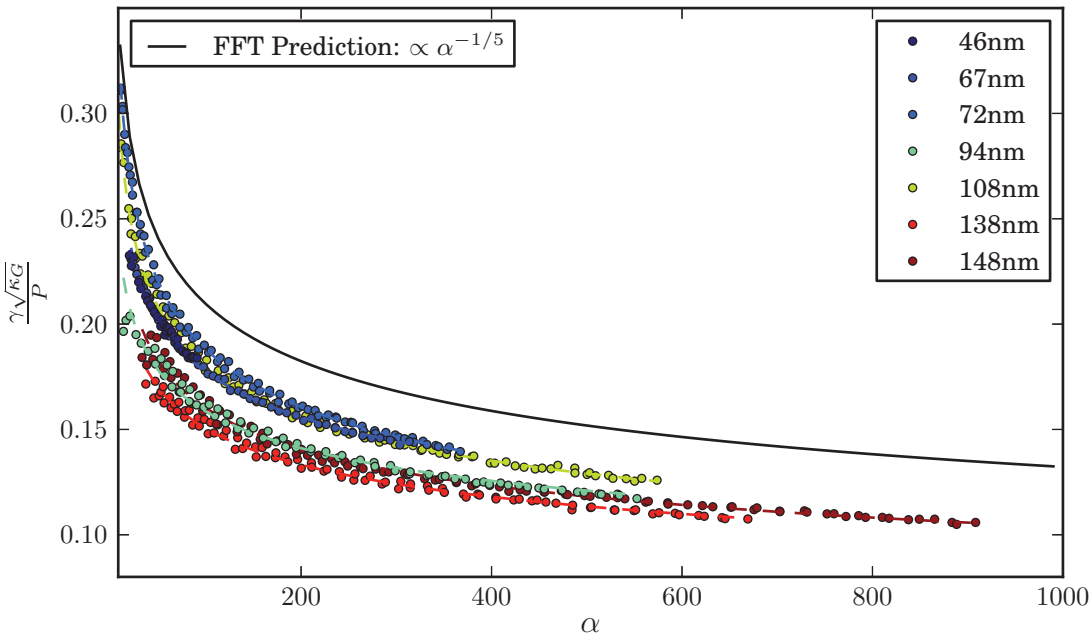

Figure 3.13. Scaled curvature $\gamma\sqrt{\kappa_G}/P$ at center as a function of confinement α (circles), linear fits (dashed), FFT prediction $\propto \alpha^{-1/5}$ (black line).

$$\frac{\alpha}{\alpha_c} = \frac{W}{L}\left(\frac{L}{R_{eff}}\right)^2\left(\frac{W}{R}\right)^2 = \left(\frac{R_{eff}}{R}\right)^2\left(\frac{\alpha}{\alpha_c}\right)^{3/5}$$
$$\rightarrow \frac{R}{R_{eff}} = \left(\frac{\alpha}{\alpha_c}\right)^{-1/5} \tag{3.6}$$

The left hand side of the last line can be expressed in terms of measured quantities: $1/R_{eff} \approx \sqrt{\kappa_G}$, $R = P/\gamma$:

$$\frac{\gamma\sqrt{\kappa_G}}{P} \approx \left(\frac{\alpha}{\alpha_c}\right)^{-1/5} \tag{3.7}$$

Data from individual runs appears to follow their fit power laws throughout the large range in confinement. The fitting exponent values for the 9 samples measured: -0.19 ± 0.02 include the -1/5 predicted by the FFT solution. The individual fit parameters are shown in Table 3.1. A constant offset in the pressure measurements for any sample shifts the curve and changes its slope. Fig. 3.15 shows the same data with pressures shifted such that the fitted exponent $\delta = -0.2$. The shift of the pressure

Table 3.1. Results from fit: $\gamma\sqrt{\kappa_G}/P = A\alpha^{\delta}$

Thickness:	δ	A
46nm	-0.162	-0.961
67nm	-0.186	-0.872
72nm	-0.227	-0.625
94nm	-0.187	-0.981
94nm	-0.168	-1.068
108nm	-0.207	-0.758
138nm	-0.175	-1.087
148nm	-0.189	-0.960

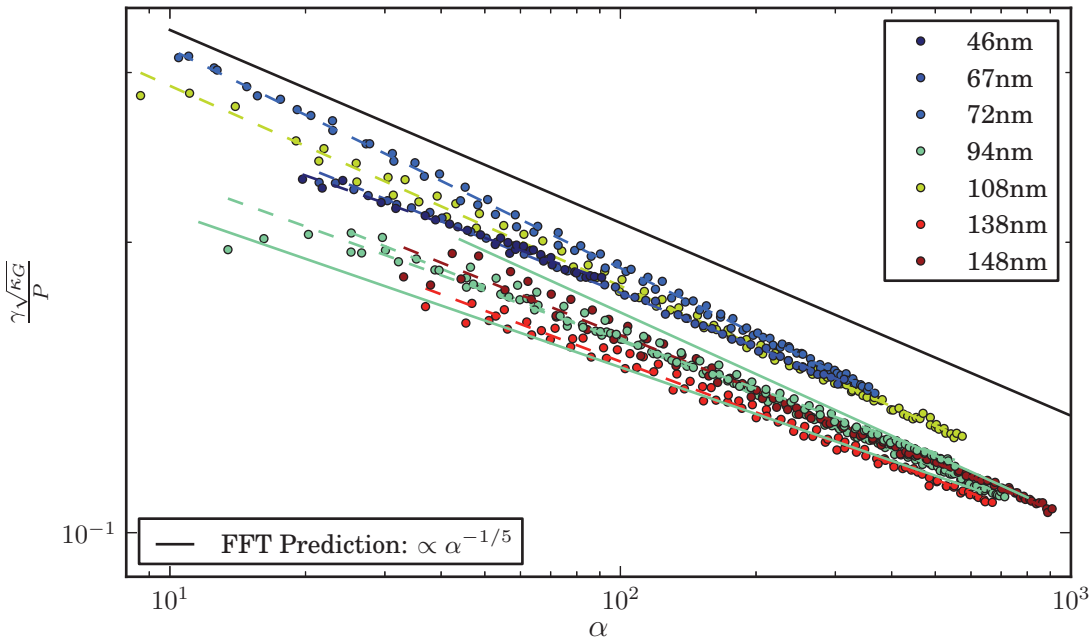

Figure 3.14. Scaled curvature $\gamma\sqrt{\kappa_G}/P$ at center as a function of confinement α (circles), linear fits (dashed), FFT prediction $\propto \alpha^{-1/5}$ (black line). Solid lines around the 94nm sample provide an estimate of uncertainty in slope due to possible systematic error (± 3 Pa) in the pressure measurement, which is likely to vary from sample to sample.

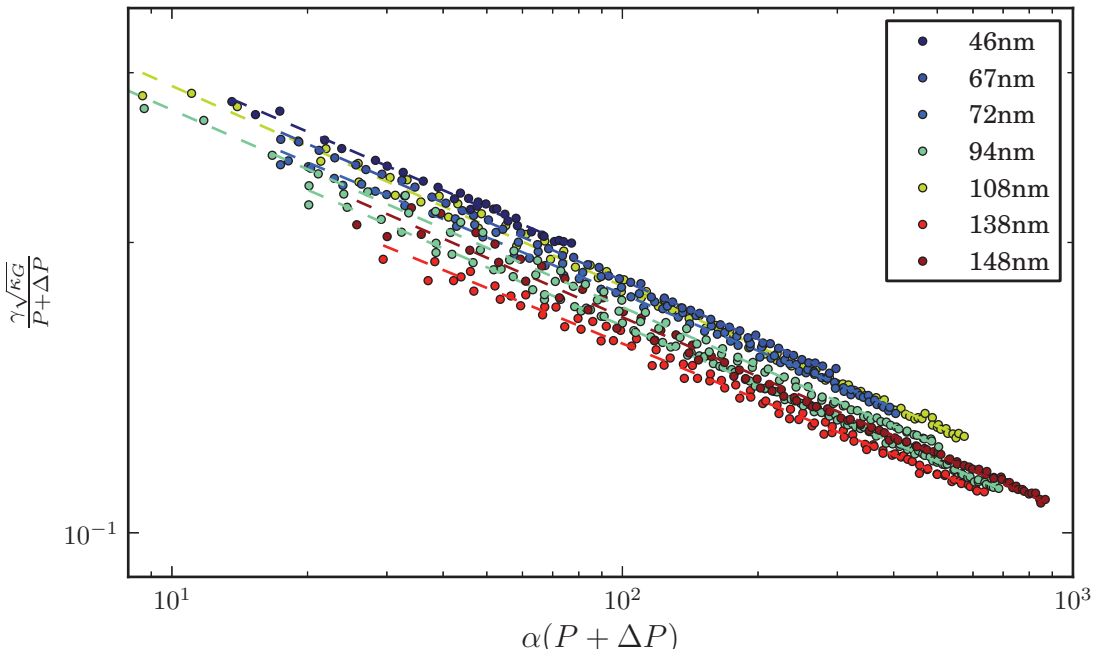

Figure 3.15. Scaled curvature as a function of alpha like Fig. 3.14, with pressure values shifted until the fitted exponent = -0.2. The maximum necessary shift was 2 Pa, within the uncertainty of the pressure measurement. The data for different thicknesses collapses slightly better with this adjustment.

origin within the known systematic error leads to slightly improved data collapse and slopes in agreement with the prediction. However, even when this freedom to adjust pressure is employed, perfect data collpse is not achieved as there is a spread in the intercept (pre-factor of the power law). The prefactor does not have a systematic thickness dependence. Thus this may only reflect sample-to-sample reproducibility.

That the curvature at the sheet's center seems to follow the same power law throughout the large range of confinement shows that this particular quantity does not function as a sensitive order parameter for the crumpling transition. We had looked for this parameter far away from the crumpling features specifically to have evidence that a global change had occurred. Not finding it, however, could simply mean that the mechanics at this particular location is indifferent to the transition. Next, we turn to the full radial distribution of curvature values.

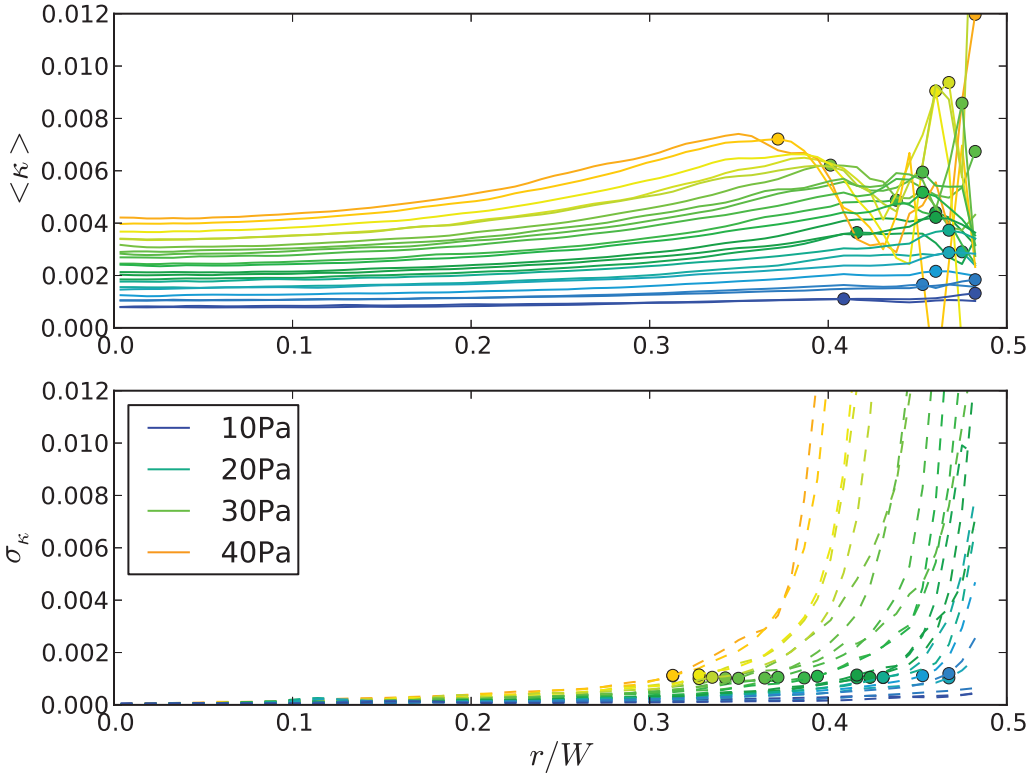

Figure 3.16. (Top) Radial dependence of gaussian curvature, averaged over thin annuli, plotted for different values of pressure, indicated by the color. Circles show the location of maxima. (Bottom) Standard deviation of curvature values in the annuli increases dramatically beyond some point. Here, circles identify the position at which the deviation crosses a threshold value of 0.001, chosen by eye. The peak in the gaussian curvature becomes more pronounced with increasing confinement, and moves toward the center ahead of its variance.

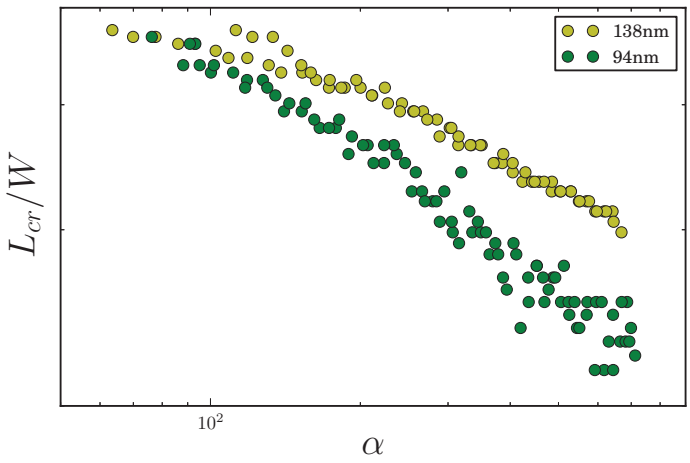

Figure 3.17. Radial extent of region with small azimuthal variation in gaussian curvature, calculated from the standard deviation of curvature values in annuli of varying radial distances from the center (circles in lower panel of Fig. 3.16). Due to the sensitivity of this calculation to imperfections, this data is presently only available for two data sets.

To characterize the radial distribution of stress, the average and standard deviation of curvature within slender ($\Delta r = 5$ pixel) annuli at varying distances from the center was calculated for different drop sizes, and are shown for a sample sheet in the top of Fig. 3.16. A peak in the gaussian curvature, far away from the center, but within the region with large azimuthal variation in curvature, becomes more pronounced with increasing confinement.

Recalling the method of measuring wrinkle length, in which we found the radius at which the standard deviation of light intensity crossed a threshold value as it began to rapidly grow, we label circles where the deviation in curvature crosses a threshold (here, $0.001m^{-2}$) as it begins to rapidly increase toward the edge of the sheet. The radii at which this happens is notably smaller than the smallest wrinkle length L that we've seen, further demonstrating that the azimuthal asymmetry in the gaussian curvature extends into the visibly featureless region where the FFT calculation assumes stress symmetry.

Fig. 3.17 shows this 'uncrumpled region' L_{cr} for two samples, calculated with the method described in Sec. 2.4.3, except here the deviation in concentric circles of the curvature is used in place of that of the light intensity. The radial location where the deviation crossed a small threshold fixed a length for a given map (circles in lower panel of Fig. 3.16). The data follows what could be a meaningful trend, but due to the sensitivity of the method to small imperfections in the curvature maps, the calculation was obtained only for two samples so far. By comparing with Fig. 2.20, we see again that the asymmetry in curvature extends to very small radii compared with the longest measured visible features.

One more quantity which is sensitive to subtle (especially asymmetric) changes in shape is the difference between principle curvature values. For instance, if frustration at large confinement caused the sheet to preferentially bend in one direction more than the other, it wouldn't necessarily be directly noticeable from the gaussian curvature data. Such a symmetry-breaking event would, however, be conspicuous in the difference between principle curvatures. Using the values of mean and gaussian curvature, we can construct this quantity even though we don't know κ_1 and κ_2 individually:

$$\frac{|\kappa_1 - \kappa_2|}{\kappa_1 + \kappa_2} = |\frac{\sqrt{\kappa^2 - \kappa_G}}{\kappa}| \tag{3.8}$$

where κ and κ_G are still the mean and gaussian curvatures, respectively. Fig. 3.18, shows a sequence of maps of this anisotropy between the principle curvatures, with decreasing drop size. The larger values are confined to the edges where we previously saw large variations in the gaussian and mean curvature. There is no obvious asymmetric structures appearing at the center, even at large confinement.

We can similarly calculate the radial distribution of the difference between principle curvatures, as we did for the gaussian curvature. Fig. 3.19 shows the radial dependence of the quantity, averaged around concentric annuli, in the top panel, and its deviation over those annuli in the bottom. Until the beginning of the large de-

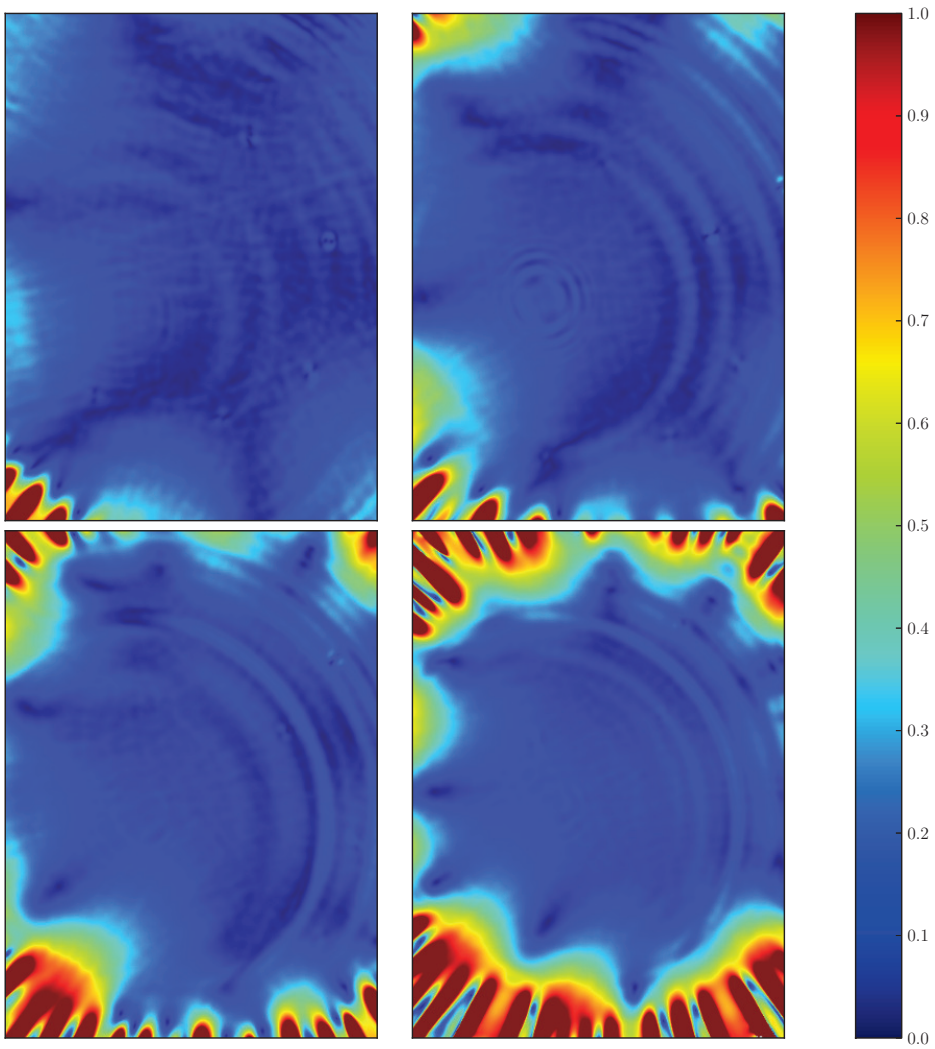

Figure 3.18. Scaled difference between principle curvatures, $\frac{|\kappa_1-\kappa_2|}{\kappa_1+\kappa_2}$ across a 138nm sheet for $\alpha = 100, 210, 370, 670$. The difference is predictably large at the edges where we previously saw variation in gaussian and mean curvature. Small values toward the center give no clear indication of a symmetry-breaking event there at large confinement.

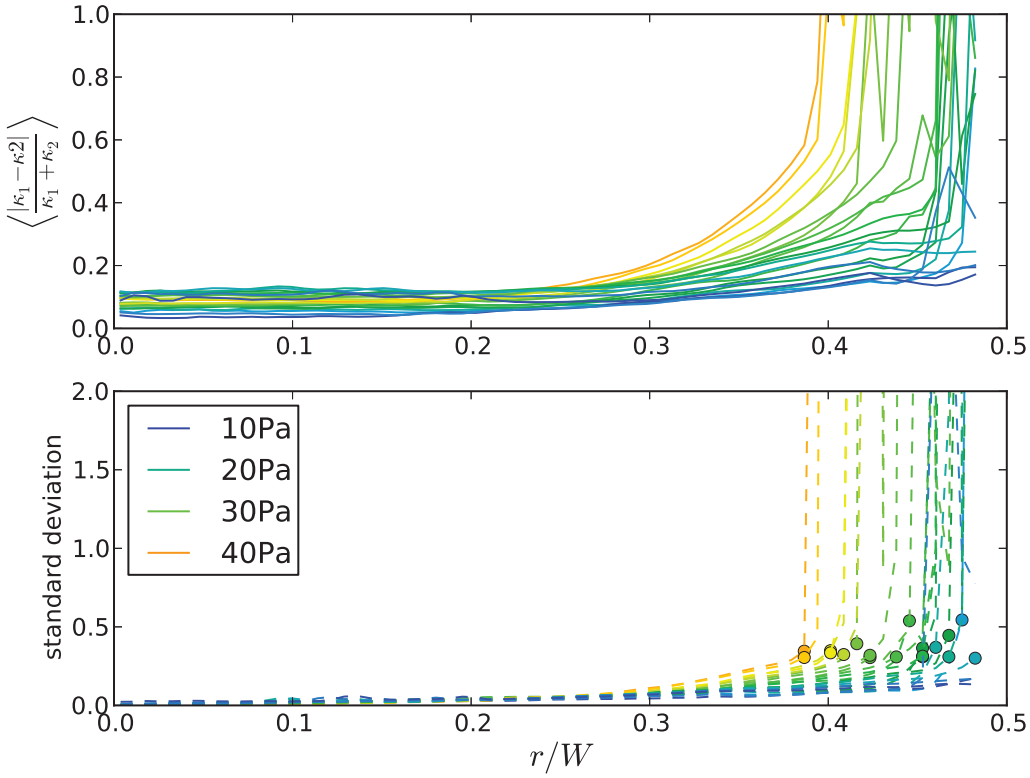

Figure 3.19. (Top) Radial dependence of the difference between principle curvatures, averaged over thin annuli, plotted for different values of pressure, indicated by the color. (Bottom) Standard deviation of curvature values in the annuli increases dramatically beyond some point. Circles identify the position at which the deviation crosses a threshold value of 0.3.

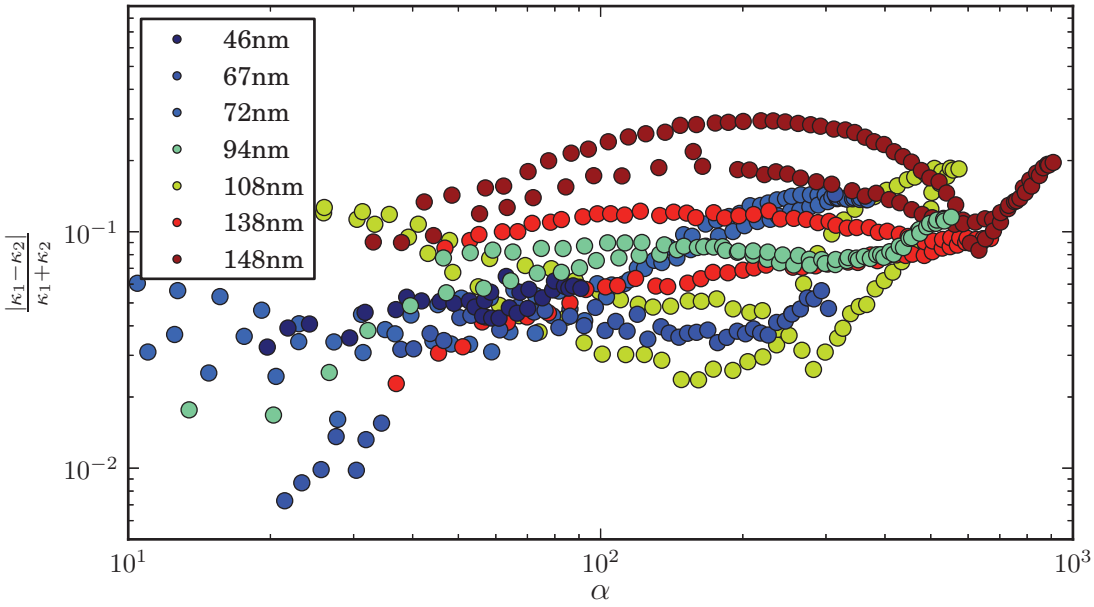

Figure 3.20. Scaled difference between principle curvatures, averaged in a small region at the center as a function of confinement α (circles).

viations in curvature, it appears the asymmetry in principle curvatures is relatively constant in the middle. This is consistent with the notion of the 'axisymmetric cap' which is assumed in FFT analysis.

Though there wasn't any apparent trend from Fig. 3.19, we are tempted to see clearly how this new quantity changes at the center while the sheet crumples. In Fig. 3.20, the value averaged over a small range (radius=20 pixels) at the center is plotted as a function of alpha for samples of different thicknesses. The collapse is poor, and though the curves generally trend upward toward large confinement (but not about the same value), they seem to be sensitive to other unknown, possibly tiny factors, such as imperfections in the sheet, which slowly pass by the field of view as the sheet rotates.

3.4 Comparison with Folding, Period Doubling

That a regular wrinkle pattern can give way to additional symmetry breaking events with increasing confinement has been documented before. Previous studies have shown how further instabilities lead to new shapes. One example, illustrated on

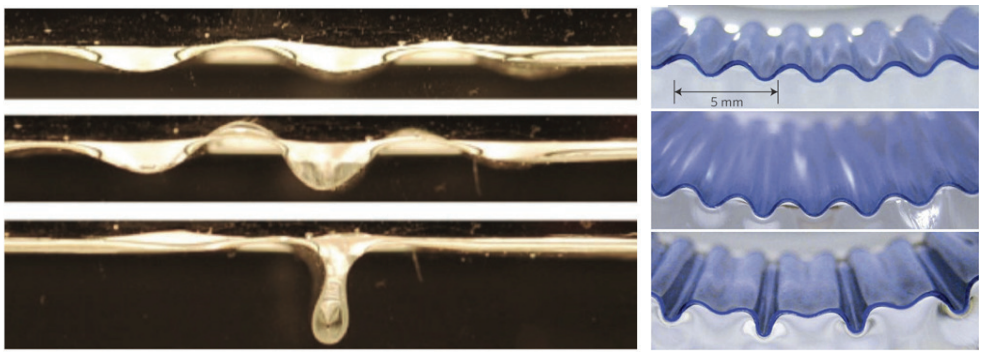

Figure 3.21. With increasing compression downward: (left) a wrinkle in a fluid suported film turns into a fold[28]; (right) the wrinkle pattern on a soft substrate supported film experiences 'period doubling'.[3]

the left in Fig. 3.21 is a folding transition, in which one wrinkle in a polyester film on water becomes more pronounced and swallows the excess amplitude from the surrounding pattern [28]. In a 'period doubling'[3] and 'period n-pling' [11] transitions, the wrinkling symmetry is broken by modes of smaller wavelength. The image on the right of Fig. 3.21 shows this happening to a the hardened skin of a soft PDMS foundation.

The important difference between our wrinkle-to-crumple transition and these cases is that, despite additional symmetry breaking of shape and localization of bending, the (in-plane) stress field is thought to maintain its original symmetry and remain unfocused.

3.5 Summary

In this chapter we have experimentally probed the second wrinkle-to-crumple transition, intent on determining the parameter which drives the transition, and an

order parameter which characterizes the crumpled state. We didn't find a definitive answer for either, but made some relevant observations.

By observing wrinkle length data at high confinement values from the procedure of the previous chapter, we found that the wrinkling to crumpling transition is associated with the emergence of multiple length scales as the wrinkle extent crosses half the system size ($W/2$).

By measuring the gaussian curvature over the surface of the sheet using optical profilometry, we observed that crumpling is associated with increasing azimuthal asymmetry and focused distribution of gaussian curvature. This suggests that in-plane stress is also becoming less symmetric and more focused. This redistribution of stress near the crumpled features had no apparent affect on the gaussian curvature at the center, and its dependence on α remained consistent with the FFT prediction throughout the probed range $10 < \alpha < 1000$. Measurement of the asymmetry between the two principle curvatures further indicated that the center of the sheet remains featureless and axisymmetric even as the sheet crumples.

We observed the formation of cusps by the merging of neighboring positively curved wrinkle tips. This was found at low confinement compared to the other indications of crumpling. Though the shape of the cusps is similar to that of d-cones, in that they display a reversal of the sign of gaussian curvature in the radial direction, stress does not appear to strongly localize at their tips as soon as they are formed. Radial tension likely suppresses that behavior and smoothes the stresses to a larger area. Though direct measurement of the process was impossible due to the high slopes involved, it is likely that these structures become sharper and gradually relieve frustration in the surrounding material as more curvature is applied.

CHAPTER 4

CONCLUSIONS AND FURTHER DIRECTION

Casual observation of everyday phenomena can lead a curious person to wonder about underlying principles. That the shape of a drawn curtain, wadded shirt, ball of newspaper, or skin of rotting fruit and elderly faces share certain motifs should tell us that perhaps a deeper issue is being resolved by nature in slightly different circumstances. The issue here is the choice of morphology of thin sheets, and it depends on two intimately connected, fundamental questions. One needs to be answered by *geometry*: what constraints does a 2D object have to obey in occupying 3D? The other by *mechanics*: what is the response of a sheet, as a physical object, to forces at boundaries and geometric constraints?

Some fundamental answers to these questions are known, but don't completely satisfy curiosity when it comes to interesting phenomena. Gauss' 'theorema egregium', which geometrically couples curvature with strain, and the Föppl–von Kármán (FvK) equations, which express force balance in thin sheets, have been around for over a century, but that doesn't necessarily mean we can effectively use them predict or understand the behavior in the everyday examples above. One problem is that the FvK equations are notoriously difficult to solve for anything but trivial cases. The added complexity from the mechanics of one additional ingredient in the problem, such as a soft substrate, is often enough to make intuitive predictions difficult or unreliable. In the case of a crumpled paper ball, the complicated shape alone obscures hope of meaningfully applying the basic theory we believe describes it.

To understand and predict such phenomena, we rely both on larger conceptual building blocks and on theoretical tools for appropriately simplifying the math. Wrinkling, as expressed in Ref. [6], defines a class of deformations by a simple mechanism and predictable, material-dependent wavelength. In this way it reduces the amount of complexity we have to consider. Similarly, the identification of d-cones and ridges as basic stress focusing elements, as reviewed in Ref. [40], gives direction to an otherwise hopeless analysis of a densely crumpled sheet. Together, the two paradigms of wrinkling and crumpling are useful in framing a wide range of thin sheet morphologies, and have been individually studied experimentally and theoretically.

In our experimental study of the sheet on a drop, we intended to build on these concepts, addressing the question: how much of which type of phenomena should we expect, given a quantified amount of confinement? In the process, we verified the applicability of a new theoretical tool for distinguishing between and choosing the applicable limiting behavior of the FvK equations, and shed some light on the previously unobserved transition between wrinkled and crumpled states.

4.1 Significance of the Sheet on a Drop

4.1.1 FFT verification

When wrinkling is induced in a sheet, a wavelength characterizes the buckled pattern and tells us about relevant material properties. If only a portion of the sheet is wrinkled, we might assume that the sheet was compressed in that region and not others. This could be valuable information about the applied stress field. The problem with extrapolating it from a buckled shape is that it requires an assumption about how much the buckling itself changed the stress field. This could be anywhere from 'completely relaxed' to 'unchanged', depending on materials and geometry. These are the limits of 'far from threshold' (FFT) and 'near threshold' (NT) behavior, respectively, and the material and geometric dependence is quantified by the 'bendability'.

The applicability of FFT or NT is estimated by the bendability parameter, which compares bending response of the sheet to compressive forces that characterize on the particular problem. Though the assumption of FFT theory has been used before [35, 26] and has been called 'tension field theory', the systematic method of distinguishing the FFT from NT regimes via bendability parameter is new[8] and was, previous to our experiment, untested.

Verification of the theory required applying a controlled compressive stress that varied across the sheet and measuring the extent of the resulting pattern. This also had to be done in a geometry that allowed for theoretical predictions. These issues can be addressed by using uniform capillary forces for confinement and axisymmetric geometry. This suggested three candidates: the 'Lamé problem', the 'drop on a sheet', and the 'sheet on a drop'. The FFT calculation for wrinkle extent in the Lamé problem is available [8], but experiments are still in progress, so data has not yet been presented for comparison. Experimental data is available for the drop on a sheet [16], which clearly disagrees with the NT prediction [37], but a FFT prediction is still in progress. The relatively wide range of confinement available to the sheet on a drop, however, still make it a more valuable system for comparison with theory.

For the sheet on a drop, we were able to compare experimental data for wrinkle extent with the NT and FFT predictions. It agreed strongly with the latter, consistent with the high bendability we measured for our system, and encouraging to the prospect of effectively using the theory in a wide range of applications.

4.1.2 Wrinkling-to-Crumpling

The Lamé problem and drop on a sheet possess stress profiles and wrinkle patterns qualitatively similar to those of the sheet on a drop. They differ in that the confinement of the sheet on a drop is dependent on curvature, whereas the other two are planar. In experiment, they also differ in their behavior at large confinement: the

sheet on a drop gradually displays distinctive crumpling traits, where the other two do not[1]. We think that, beyond producing a compressive hoop stress, the curvature of the sheet on a drop is fundamentally related to the process of crumpling.

The emergence of crumpling from an already buckled (wrinkled) state has, as far as we know, not been seen before. From our measurements of the gaussian curvature distributions, we indirectly see that azimuthal anisotropy in stress is associated with the crumpled state, whereas the FFT analysis of the wrinkled state depended on its axisymmetry. We concluded that while the wrinkling transition broke axisymmetry in its deformation field and preserved it in its stress field, the crumpling process is characterized by the primary breaking of stress axisymmetry.

The transition is continuous (or absent) in all the parameters we have measured, but it is possible that there is a right order parameter that we haven't measured. Despite the striking difference between the clearly wrinkled and clearly crumpled states, like those in Fig. 3.1, pinpointing the image in a sequence where the transition 'occurred' is infuriatingly difficult.

We have observed the increasing asymmetry, increasingly inward from the nearest visible feature, in the gaussian curvature while the sheet crumples. We have also observed the local mechanism of creating cusps, which resemble d-cones, but do not immediately focus stress, out of adjacent wrinkle tips.

We have looked for a measurable order parameter to indicate the occurrence of a global transition in a number of quantities. The deviation in the wrinkle length trend is perhaps the most apparent indicator of a changed behavior, but it is not ideal as an order parameter in that it convolutes the lengths of potentially different things: the compressive stress region and some sharply or smoothly varying features

[1]In the Lamé experiment at large confinement, folds cross the entire annulus radially, which do not focus stresses and can be distinguished from crumples in that they are only localized in one direction.

appearing in the light intensity. One powerful sign that the sheet discards one type of solution for a distinctly different one in the transition would have been a change in shape, or change in behavior of the shape of the sheet far away from the edges. Our measurement of the gaussian curvature at the center does not give such an indication. The scaled curvature appears to agree very well with the FFT prediction well into the high confinement range where the sheet would be considered very crumpled. Our measurement of the difference between principle curvatures also suggests that the center of the sheet, far away from the large deformations, maintains a largely symmetric shape; is unaware that somewhere wrinkles are being replaced by crumples.

We haven't yet identified a clear driving parameter for the transition, and this leaves room for more than one explanation of the whole phenomenon. One is that α still characterizes the system, but that it responds differently to large α, by gradually accepting a different solution. This scenario could be inferred from the dashed line between wrinkled and crumpled phases in Fig. 2.25, but that part of the diagram simply reflects our experimental observation, not any prediction. Because α acts on the sheet by determining the in-plane stress profile, this scenario would ignore any special role of curvature in the problem and would suggest that crumpling should also occur in the planar geometries, and it doesn't.

In another possible scenario wrinkling and crumpling are not completely exclusive solutions: Two parameters which increase with two different powers of pressure induce wrinkling and crumpling, α and β. At small pressures, both parameters are small. At a pressure which depends on sheet thickness, α passes α_c and wrinkles are induced, but β remains small, and so we see only wrinkles. At greater pressure, β grows larger (possibly crossing a critical β_c) and stresses begin to focus, but not so much that the stress field near the wrinkle tips is significantly affected. The first signs of the onset of crumpling are largely obscured by the more dominant wrinkle pattern. At some point, the crumpled features are well developed and begin to affect the

stress field and wrinkle pattern. Now, at this value of pressure which depends on both α and β, the measurement of a wrinkle length is ambiguous. Somehow, this combination necessarily happens when $L \approx W/2$, possibly well after the onset of crumpling, possibly when a deviation in the stress field that had also been progressing inward from the edge caught up with the wrinkle pattern. It seems likely that β also depends on the same quantities as α (though not necessarily with the same power: Y/γ because a stretched sheet doesn't crumple, and W/R because curvature distinguishes our crumpled case with the non-crumpled planar geometries.

Further insight into a phenomenon can come from studying a radically different situation that seems to share some core elements. For this reason, we will look briefly in the next section at another system, similar in spirit but not in material, in which stress focusing is induced by geometric frustration.

4.2 Particle-laden Fluid Interfaces

For two examples, we will consider the mechanics of truly 2D surfaces. These are interfaces between two fluids, like those in Sec. 1.2, with the same energetic considerations, except that these have spherical particles adsorbed to them. In the first example, we will discuss the formation of defects in a 2D crystal of such particles on a curved interface, for the insight it can lend our understanding of crumpling of the sheet on a drop. In the second, a wrinkle pattern is observed in a compressed raft of particles which, when viewed in the context of thin sheet mechanics, presents an interesting mystery.

4.2.1 Defects in 2D crystals and Crumpling

In this case, the surface tension is greater than any other energy, so the interface negligibly deviates from the relaxed shape of the drop. The adsorption energy is very high, such that no particles are expected to leave the surface. The adsorbed

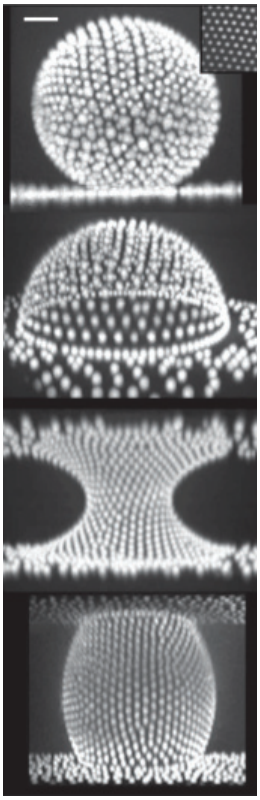

Figure 4.1. Repulsive particles adsorbed to surfaces of various shapes[19].

spheres are of like charge, and therefore repel each other. In doing so, they fall into a hexagonally ordered 2D crystalline structure. In this structure, particles have reference positions with respect to their neighbors, like a metric. Changing positions relative to this metric amounts to strain, with associated stress and, in this case, electrostatic energy. When curvature is imposed, the flat metric is frustrated, causing global stretching strains. At some critical strain, defects form, in which particles switch positions and adopt a new relaxed metric. The new metric including the defects has a relaxed configuration with some curvature. The defects can be identified by the number of neighbors. A five-fold disclination is a place where a particle has 5 neighbors instead of the original 6. It carries a topological charge which represents a certain amount of gaussian curvature. The relaxed shape of a crystal near a five-fold

disclination is conical. The local stress near a defect is great, so that the total stress can be small. In this sense, making a defect is an act of stress focusing.

It is worth noting that for a closed sphere, the total defect charge is fixed, as a topological invariant. When there is a boundary, however, the system can introduce defects from it in order to minimize the energy. This way the choice is made both by geometry *and* mechanics.

Comparing and contrasting the crystal with the sheet: The nature of the strain, as a continuous metric or discrete lattice, and its connection to the geometric frustration of applied gaussian curvature is the same. Both d-cones and disclinations are conical, with focused strain, though the disclinations are discrete. There is no reason to expect discrete charge on a d-cone. The defects seem to travel inward from the boundaries in both cases (see Fig. 4.2).

The elements of a continuous sheet are forbidden from crossing each other. Therefore, in order to make a real disclination, it would be necessary to cut out a section and reattach the edges. By pinching together an arc on the circumference, the sheet seems to 'pretend' to accomplish this (see the right of Fig. 3.1), but still benefits with relaxed stresses.

Probably the biggest obstacle in putting this analogy to use is in describing the in-plane rearrangement of discrete elements in the same terms as out-of-plane deflection of the continuous sheet. A big benefit from the analogy is that it would virtually

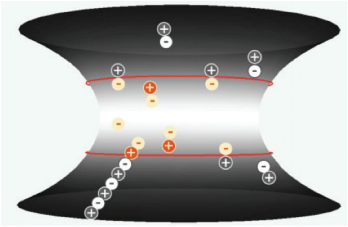

Figure 4.2. Stress relieving disclination transported from the boundary[19].

separate the process of crumpling from the process of wrinkling, giving us a clear view of stress focusing without the prebuckled shape.

In general, to the extent that we are interested in a fundamental mechanism, it should be a good strategy to find the most diverse systems that share it, and not many other peripheral details that can get in the way of its identification.

4.2.2 Particle Rafts and Wrinkling

The second example is interesting because it connects the most basic ideas of capillarity and wrinkling in an unexpected way. The experiment is identical to the

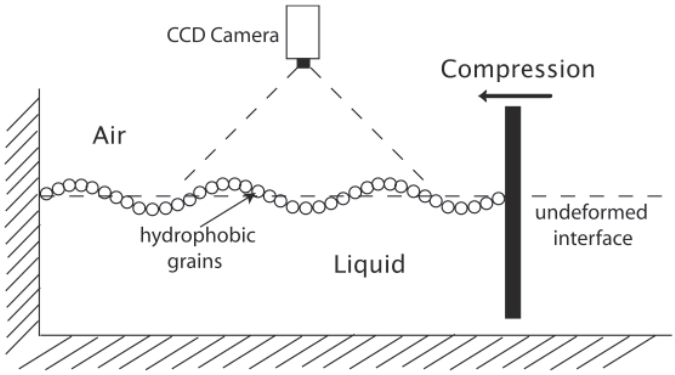

Figure 4.3. Uniaxial compression of a 'particle raft' produces wrinkles, suggestive of a bending modulus.[38]

uniaxial compression of a liquid supported film in Fig. 1.6, except that the film has been replaced with a disordered monolayer of hydrophobic particles, or 'particle raft'[38], illustrated in Fig. 4.3.

Particles are able to rearrange as the raft compresses in-plane until a point when they cannot compact further. Then, the raft is forced to buckle out of plane. It produces uniform wrinkles perpendicular to the compression, as does the thin sheet. Especially in the context of this work, the existence of such a pattern immediately suggests that a bending energy is involved: the wavelength should be chosen by

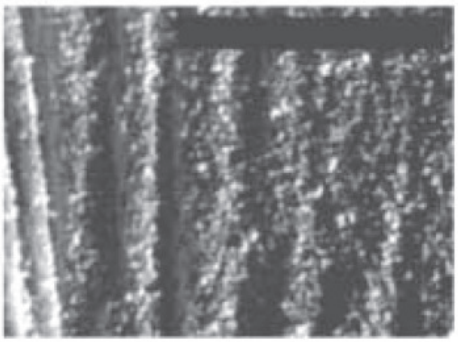

Figure 4.4. Top view of a wrinkled particle raft. The scale bar represents 5mm.[38]

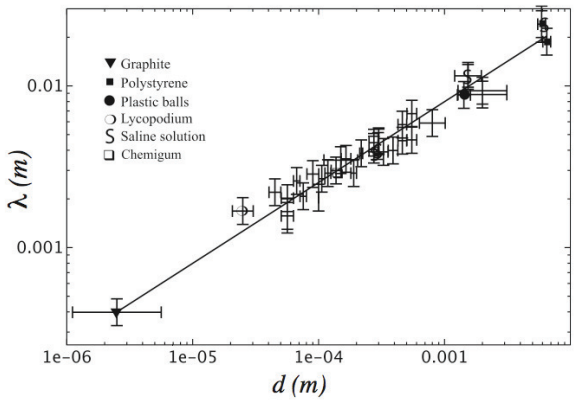

Figure 4.5. The solid line comes from a calculation of the thin sheet modulus $B = \frac{Et^3}{12(1-\nu^2)}$, but with E of capillary origin, ultimately giving a d^2 dependence[38].

competition between gravity, which prefers small amplitude, and the raft's bending modulus, which prefers the largest wavelength.

The immediate question should be: what is the physical origin of the bending modulus? In Fig. 1.2 we saw how it came from tension and compression within the thickness of the continuous elastic sheet. This argument cannot apply to the particle raft, in which elements interact with each other only at their points of contact. Without a thickness in which to store compressive and tensional stresses, the inherently two dimensional raft shouldn't have a bending modulus, at least not for the same

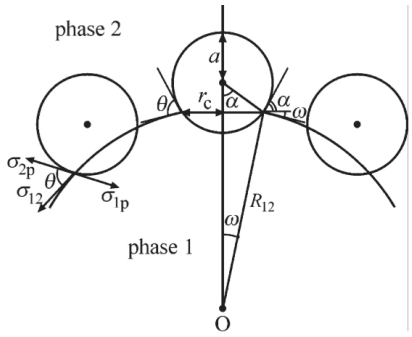

Figure 4.6. Particles adsorbed to a fluid interface interact with curvature by adjusting their depth [23].

reason. Because interfacial energy dominates the lives of such small particles on the surface, it makes sense to look for a capillary origin.

One means of deriving a bending modulus from capillarity assumes no deformation of the surface due to gravity, and no interparticle interactions: If the surface is deformed, the particles adjust their heights to satisfy the contact angle boundary condition. In doing so, they occupy a different portion of the surface area. This increases the total interfacial energy, and the increase is proportional to the curvature squared, so the coefficient can be considered a bending modulus[2]:

$$B = \frac{3}{32}\gamma\phi d^2 sin^4(\theta) \tag{4.1}$$

where ϕ is the particle area fraction, d is the particle diameter, and θ the contact angle. This calculated bending modulus has the particle diameter dependence and approximate magnitude consistent with the experimental data, seen in Fig. 4.5. A variation of the calculation was applied to explain the effect of a particle raft on the dispersion of surface waves [27].

[2]The calculation was done considering particles on a portion of a sphere, where both radii are equal. The result should be somewhat different when the raft bends only in one direction, and the particles deform the interface around them.

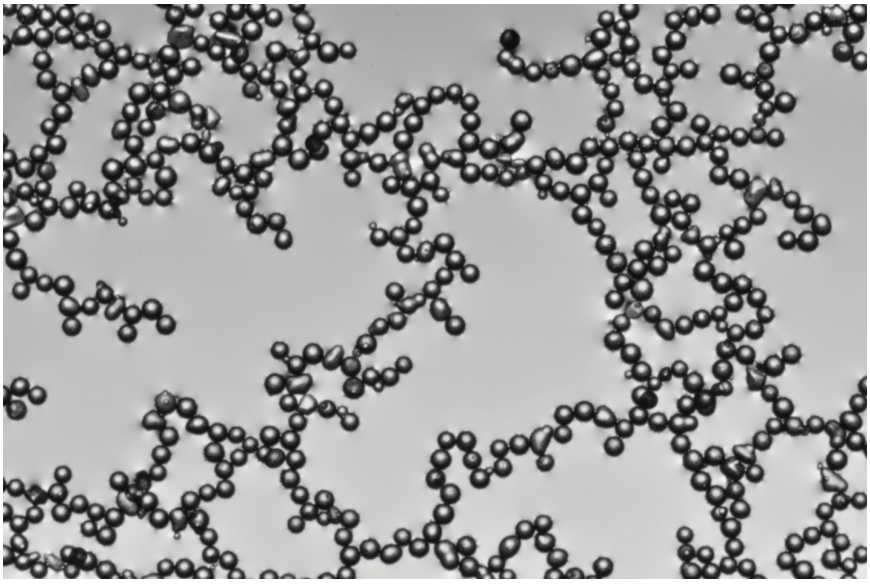

Figure 4.7. Stringy structures in the dilute raft suggest the importance of particle-particle interactions.

4.3 Continuing and Future Work

4.3.1 Holography of a Fluid Interface

The above treatment of the role of particles seems plausible, but it makes assumptions about the system that are difficult to justify, especially for macroscopic spheres. Assuming wetting with no hysteresis or pinning and no gravitational effects means that interparticle interactions are not important for the mechanical properties of the raft (except, perhaps by way of occupied area fraction). These assumptions are not consistent with some microscopic studies of particles adsorbing to interfaces [21], or with the appearance of a sample raft of large spheres, as shown in Fig. 4.7.

We have made some steps toward measuring the deformations on a surface due to adsorbed spheres with the intent to quantify the effect of wetting anisotropy from pinning, contact angle hysteresis, etc., on the shape of the interface, to see if and when they should be neglected. We built a holographic device to view a wide lateral range ($\approx cm$) with high resolution height sensitivity, based on the apparatus of Ref. [14],

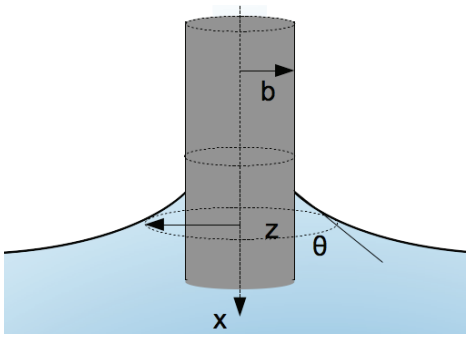

Figure 4.8. The deformation from a wetted cylinder is indistinguishable from an adsorbed buoyant particle.

and works in the following way. A laser is broadened and split into two beams with a beamsplitter. One beam is directed from below through a chamber holding a fluid with the sample interface. After passing through the top surface it enters another beamsplitter and recombines with the other beam which was simply redirected around the sample. The combined beam is projected on a screen where their interference pattern is measured. Because the beams took two separate paths, they are out of overall phase by many wavelengths, which isn't important. The important part is that the overall path of different portions of the beam travelled different optical paths. The optical path of the beam that passed through the sample was effectively shortened by the distance it spent in the more dense liquid of the sample. The variation in the phase across the surface is then related to the height variation across the surface [3]:

$$\Psi(x,y) = \frac{2\pi}{\lambda_0}\left(n_1 - n_0\right) z(x,y) \tag{4.2}$$

where n_1 and n_0 are the indices of refraction of the two fluids in the sample and λ is the wavelength of the laser. The maxima in the fringe pattern are found

[3]The principle of the device is basically the same as the optical profilometer, except it relies on refracted, rather than reflected light.

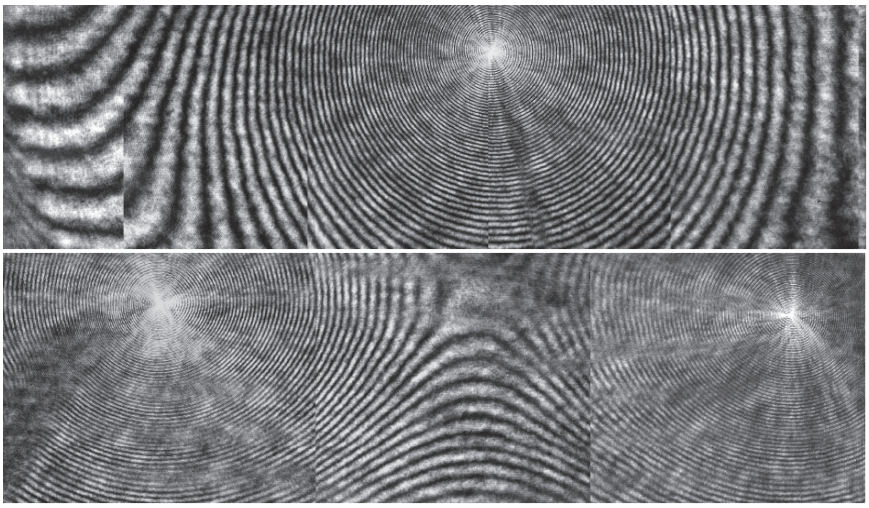

Figure 4.9. Fringe pattern from the surface deformation caused by one (top) and two (bottom) wetting optical fibers.

along the contour lines where $\Psi = 2m\pi$. The height difference between fringes is $\Delta z = \lambda/2(n_1 - n_0)$. We see that this vertical resolution can be increased by increasing the contrast in indices of refraction and decreasing the wavelength of laser. For our blue ($\lambda = 442nm$) laser and castor oil - water interface, the vertical resolution was $1.5\mu m$.

As an initial test, we used an optical fiber to deform the interface, as shown in Fig. 4.8. The fringe pattern shown in Fig. 4.9 was produced directly on a distant CCD sensor after the laser passed through a filter to decrease the intensity. A sample analysis of the fringe pattern from one fiber started at a point (at the fiber) and identified peaks and troughs in the intensity as a function of distance, as shown in the top of Fig. 4.10. Knowing the height resolution between adjacent fringes allowed us to extract the height profile, as shown in the bottom of Fig. 4.9. Large slopes and an additional interference pattern from diffraction around the fiber make analysis of the surface difficult near the center, but the broader shape is captured easily.

This system can already be used as a controlled testing ground for viewing the effects of local wetting details on the longer-range surface shape. By choice of density

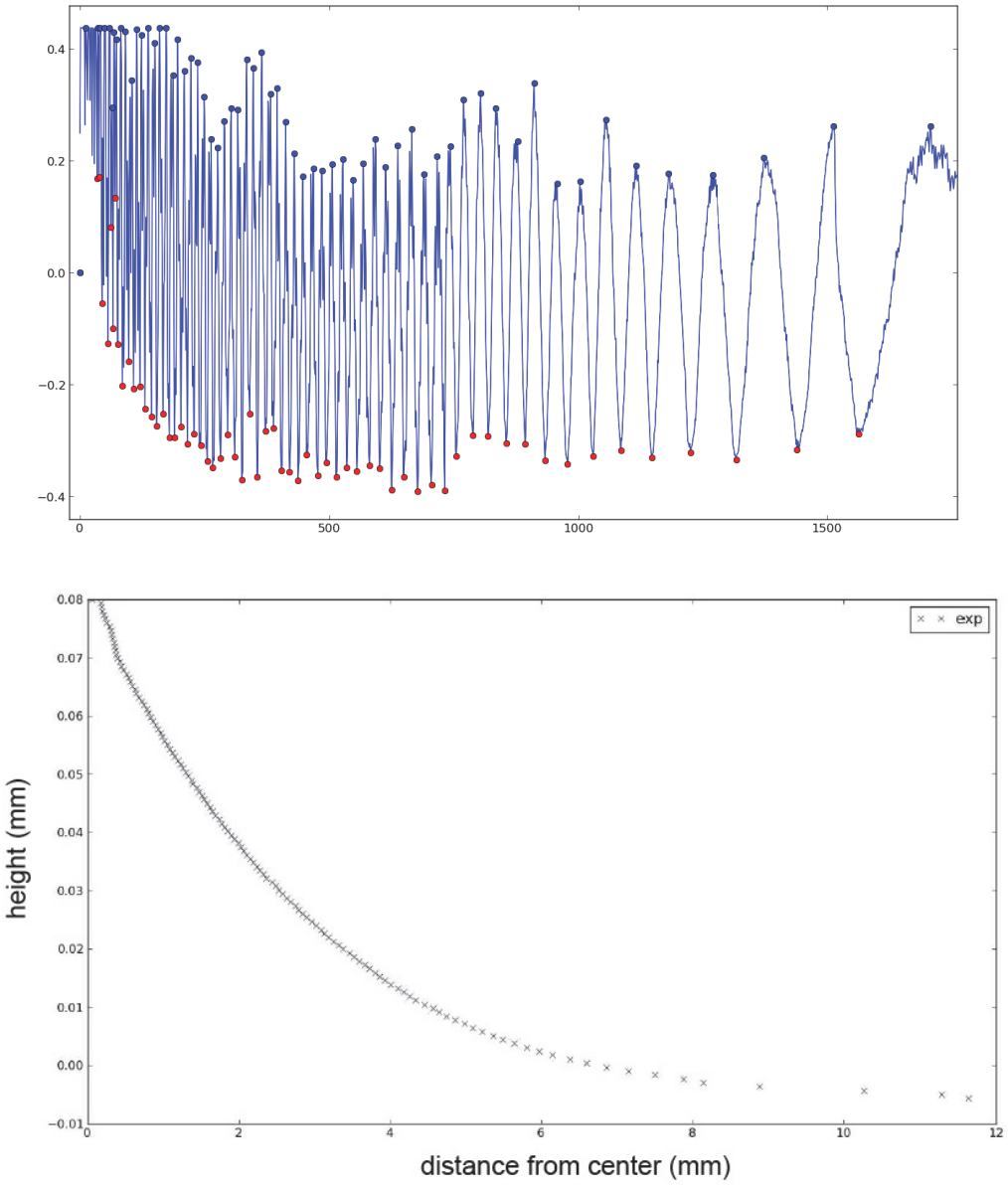

Figure 4.10. Peak determination from a radial intensity profile away from the fiber (top) and the resulting height profile (bottom).

and chemistry of the two immiscible fluids, the capillary length (see Appendix B), the important length scale for the meniscus, can be dramatically changed, allowing for the possibility to study effectively microscopic or macroscopic phenomena within the field of view.

4.3.2 Negative Curvature

So far, we have considered only the case where a sheet tries to accept positive gaussian curvature. One might expect that negative curvature should invert the problem so that the circumference of the sheet stretches, while the inside experiences compressive stresses. Using capillarity, we have prepared a prototype negative gaussian

Figure 4.11. Contact line pinning at the edges of a curved hole can be used to make a negative curvature interface.

curvature surface on which to measure negative curvature induced wrinkling. This time, the curvature comes from the boundaries rather than the applied pressure, the opposite of the positive curvature solution. We bent a thin sheet of metal along one direction into a smooth arc, as shown in Fig. 4.11. The boundaries of the hole in the sheet then follow a curve that has two sets of extrema: two opposing maxima and minima.

We can convince ourselves that this boundary will create negative gaussian curvature in a minimal surface, like a soap bubble, in the following way. If we draw a

Figure 4.12. A negative gaussian curvature surface meets boundaries like those we have chosen[41].

surface with curvatures $1/R$ and $-1/R$, like the one in Fig. 4.12, and imagine just its outer boundary, we see it has the basic shape of our bent hole. Now, because it is unreasonable for there to be more than one minimal surface solution for this geometry, we can guarantee that, upon pinning a contact line along the inside of the hole, a minimal surface will also have negative gaussian curvature.

The brass plate we have made hydrophobic on one side and dipped, that side down, into a flat surface of water, shown in Fig. 4.13. By pushing too deeply or by

Figure 4.13. Negative curvature surface created by deforming the boundaries of a zero mean curvature surface.

pulling the water upward, the affect of gravity is balanced by the Laplace pressure,

and therefore introduces finite mean curvature, which changes the argument above and eventually also changes the sign of the gaussian curvature. In the preliminary test of this setup, we made sure we were looking at negative curvature by slowly varying the height of the boundary. We saw wrinkles form, as in Fig. 4.14 at a particular range of heights, on either side of which they disappeared. The wrinkles, faintly seen here

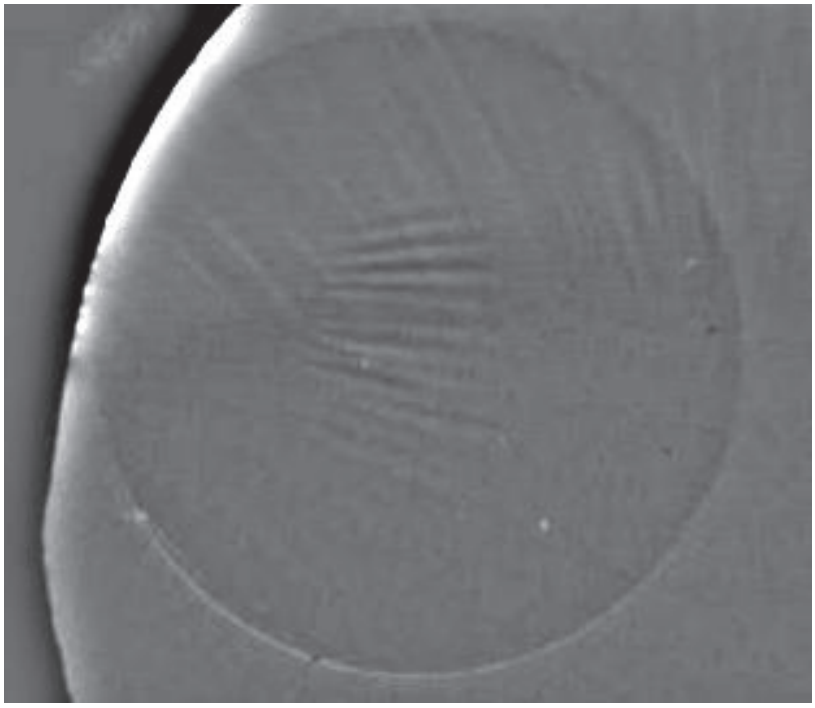

Figure 4.14. Top view of a wrinkled sheet on a negative curvature surface.

extending horizontally, are confined to the middle of the sheet. The boundaries point upward at the right and left, according to the image, and downward on the top and bottom. The sheet sits near one of the higher corners of the hole. This means that compression in the sheet points along its upward curved axis. We think that, where Laplace pressure was directly responsible in wrinkling the sheet on a drop, and gravity could be neglected, gravity is playing the analogous role here, where Laplace pressure is avoided. Without gravity, the stress would be tensile throughout the sheet. The sheet could stretch somewhat into the shape of Fig. 4.12, or mostly bend in along one of the axes (in negative curvature geometries, the symmetry is automatically broken).

Upon increasing gravity, the sheet begins to sag, and this induces compression in one direction, causing wrinkling.

Ideally, we would like to see a continuous change in applied gaussian curvature. Here, this could be done using a thin, elastic plate, perhaps of very thin spring steel, that could be continuously buckled into a known arc, as its height, level with the surface of the flat meniscus, remained constant.

APPENDIX A

SYMMETRY OF UNCOVERED DROP

Switching to glycerol had the unpleasant consequence of decreasing the precision of the pressure measurement, indicated by the disagreement in predicted values from the different menisci. A sample set of pressure measurements with no sheet, used to calibrate the measurement, is shown in Fig. A.1. Now instead of averaging the values from the two side tubes, we choose the one which agrees more with the large tube in the calibration set. In this example, the $5mm$ values are used.

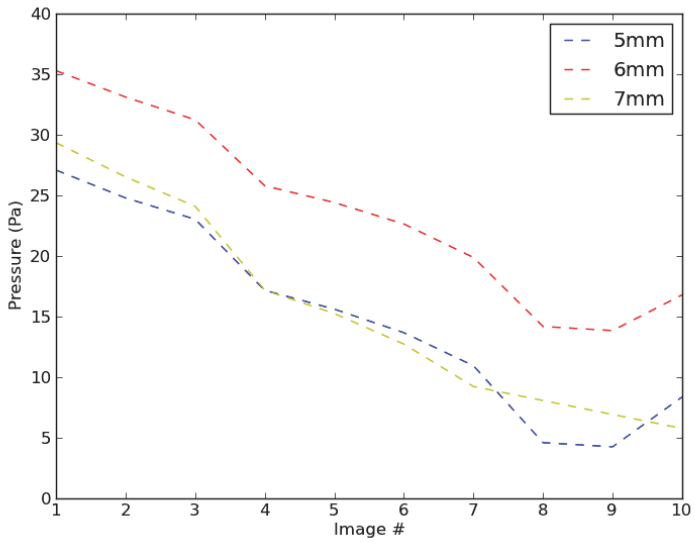

Figure A.1. Pressure measurement from three tubes using glycerol shows larger disagreement (compare with Fig. 2.12), likely due to slightly non-uniform wetting.

One new source of error is that a small amount of water is transferred with the sheet to the center meniscus, changing its surface tension relative to the other two. All

calculations are made assuming pure glycerol values: $\gamma = 0.065 N/m$, $\rho = 1260 kg/m^3$. The other significant error comes from the fact that the contact lines around the tubes are less controlled. When transferring the sheet, for instance, the hydrophobic surface of the tube was somewhat wetted. While the water contact line quickly retreated to the inside corner of the tube, glycerol appeared to be more hesitant (due to viscosity and slightly smaller surface tension) and more susceptible to imperfections in the silanized tube surface. This was barely perceptible by eye, but due to the necessary sensitivity in the pressure measurement, a reason for concern. A consequence of such irregular wetting is an asymmetric drop. Fortunately, using the profilometer we were able to measure this affect on the sheetless droplet.

Upon measuring the height maps of the exposed drop, we ran the computationally expensive code referred to in Sec. 3.3.1, by which verticle circles were fit to slices of the surface. Their curvature is plotted as a function of the angle at which the cut was made, for one small and one large drop. For a perfectly symmetric drop, these plots should be horizontal lines. The variation here, typical of our drops, represents only $\approx 2\%$ of the value of the radius.

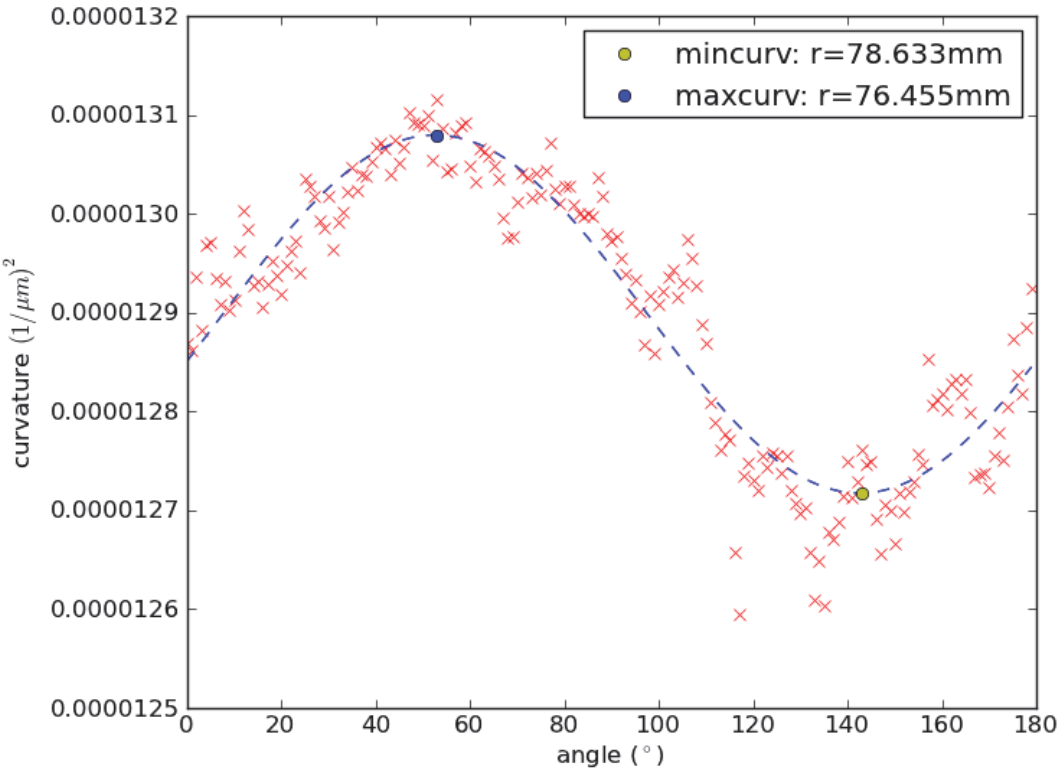

Figure A.2. Curvature as a function of angle for a drop without a sheet. Maximum and minimum curvatures are found with a sinusoidal fit.

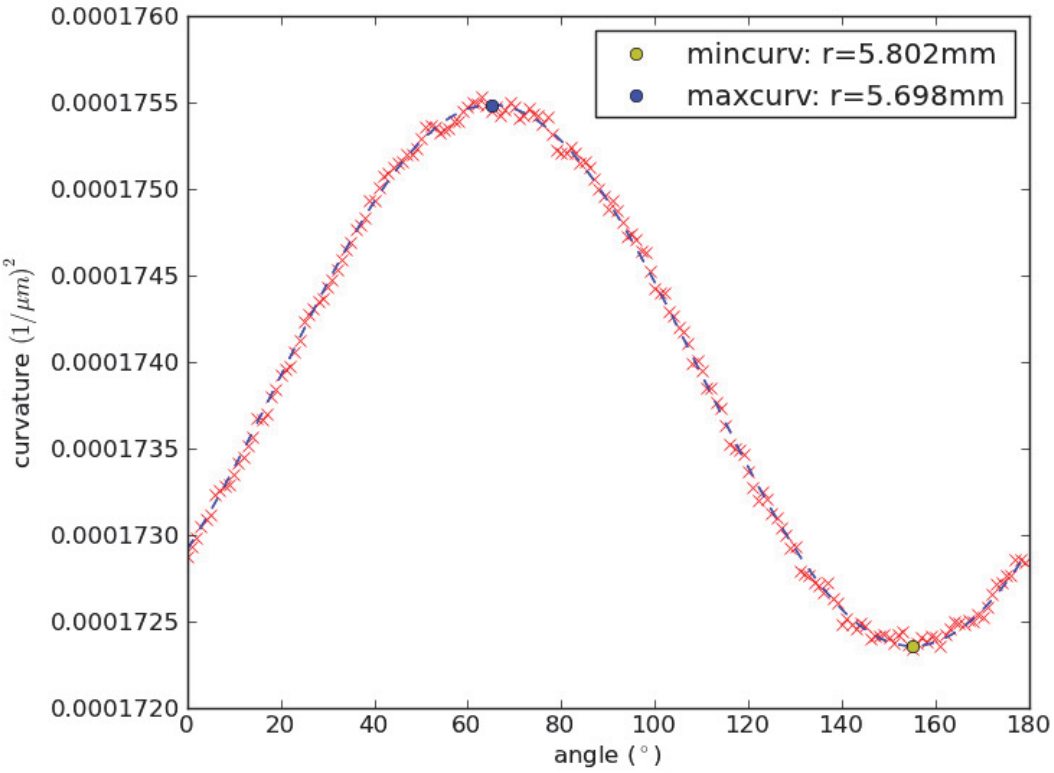

Figure A.3. Curvature as a function of angle for a larger exposed drop.

APPENDIX B

SINGLE PARTICLE ADSORPTION TO AN INTERFACE

In order to minimize interfacial energies between each medium, it can be preferable for a sphere occupy a portion of the fluid-fluid interface, its depth dependent on the three interfacial energies (see Fig. B.1). Ignoring gravity or other forces, the particle will adsorb without deforming the surface, as long as the surface is flat or has the same curvature in all directions. The result of energy minimization for all surfaces is the same as requiring that the three-phase contact angle is met around the contact line. If another force perpendicular to the surface acts on the particle (e.g. gravity), the same requirement causes the surface nearby to deform (see Fig. B.2). If the particle is pushed vertically, the interface will deform upward with it. The deformation has an energetic cost because of the increase in area. It might seem that the contact angle could compensate, but it is determined by local force balance on the surface of the particle, making it a permanent boundary condition. In Fig. B.2, gravity pulls a hydrophobic sphere into the denser fluid.

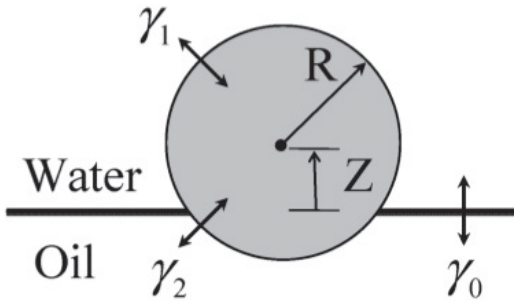

Figure B.1. A sphere adsorbed to a flat interface causes no deformation.[10]

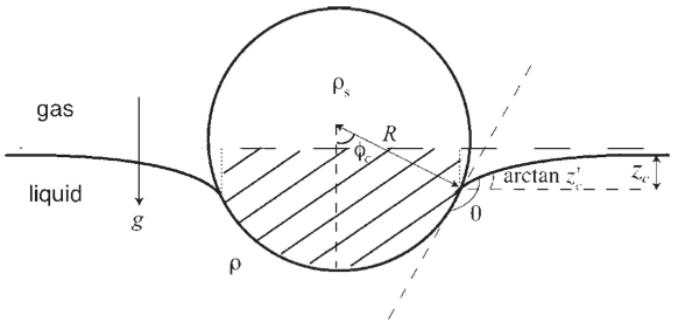

Figure B.2. Other forces on an adsorbed particle will cause the surface to locally deform[39]

Earlier, the Laplace pressure across a surface was calculated for a sphere. The more general expression relates this pressure to the mean curvature:

$$P_L = \kappa\gamma = \frac{\gamma}{2}\left(\frac{1}{R_1} + \frac{1}{R_2}\right) \tag{B.1}$$

The shape of the interface is then dependent on the pressure across the interface, by way of its mean curvature. A static fluid will have uniform hydrostatic pressure, unless a body force, such as gravity, is acting upon it, in which case the pressure varies only with height. The shape of the deformation depends on how much the particle deflected the surface at its contact, and on properties of the fluid (i.e. relative density ρ, and γ), characterized by the capillary length:

$$l_c = \sqrt{\frac{\gamma}{\rho g}} \tag{B.2}$$

APPENDIX C

WRINKLING UNDER UNIAXIAL COMPRESSION

Fig. C.1 shows a thin polystyrene sheet floating on a flat surface of water, compressed on either side by flat walls, like that in Fig. 1.6 in Sec. 1.1.3. The expected wavelength of the resulting wrinkle pattern was calculated from the competition between gravitational energy and bending energy. This argument applies and agrees well with the measured value in the middle of the sheet. Near the free edges where the sheet meets the water-air interface, however, the wavelength continuously decreases (as can be seen at the bottom of Fig. 1.6 and left of Fig. C.1).

Unlike the interior region, surface tension plays a role in the shape of the pattern near the boundary. In minimizing deformation of the meniscus near the sheet, it competes with bending resistance by further restricting the amplitude at the boundary. Following a similar argument as that in Sec. 1.1.3, this leads to a different edge wavelength $\lambda_e \propto \sqrt{\gamma/B}$. The pattern must switch from this to the bulk wavelength: $\lambda_0 \propto (\rho g/B)^{1/4}$. The distance over which this transition occurs should depend on the relative magnitudes of gravity and surface tension, namely the capillary length: $l_c = \sqrt{\gamma/\rho g}$[15].

Some interesting questions concern the extent of this boundary layer of small wavelength wrinkling: What happens when the width (perpendicular to compression direction) becomes small enough for the two opposing edge patterns to communicate? Does the bulk wavelength completely disappear? At what thickness would this occur?

For one summer, visiting teachers, Nick Harrison and Jonathan Kennedy, as part of the MRSEC RET program, performed the uniaxial compression experiment for

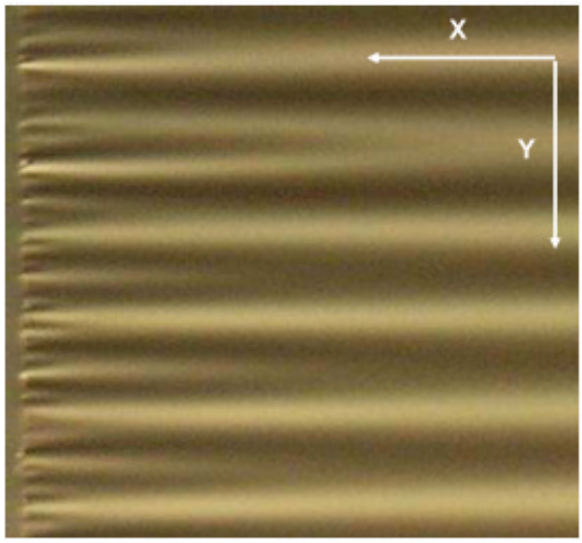

Figure C.1. Gradually decreasing wrinkle wavelength is seen near the edge (on the left) of a uniaxially compressed sheet floating on water, as surface tension works to minimize the amplitude of the pattern at the boundary with the water-air interface.[15]

a wide range of sheet widths and 3 thicknesses. They measured the wavelength at the center of the sheet from top view images and thicknesses using the white light interferometer. Some results from these experiments are displayed in Fig. C.2. The top panel shows the wavelength, scaled by the bulk wavelength prediction vs. the width of the sheet, scaled by the capillary length. Data properly described by one or the other prediction should be collapsed for the range of thicknesses, at some vertical value reflecting a multiplicative factor in the prediction which has been ignored.

The wavelengths are better collapsed by the bulk wavelength, as seen in the top panel, for most of the range in width. The edge scaling appears to get better at small widths (consistent with the prediction), though the smallest measured width is still larger than the capillary length. The approach appears gradual with decreasing width, but there is still significant noise. These results give a rough impression of how the boundary layer of the capillary dominated wrinkle pattern extends across the bulk.

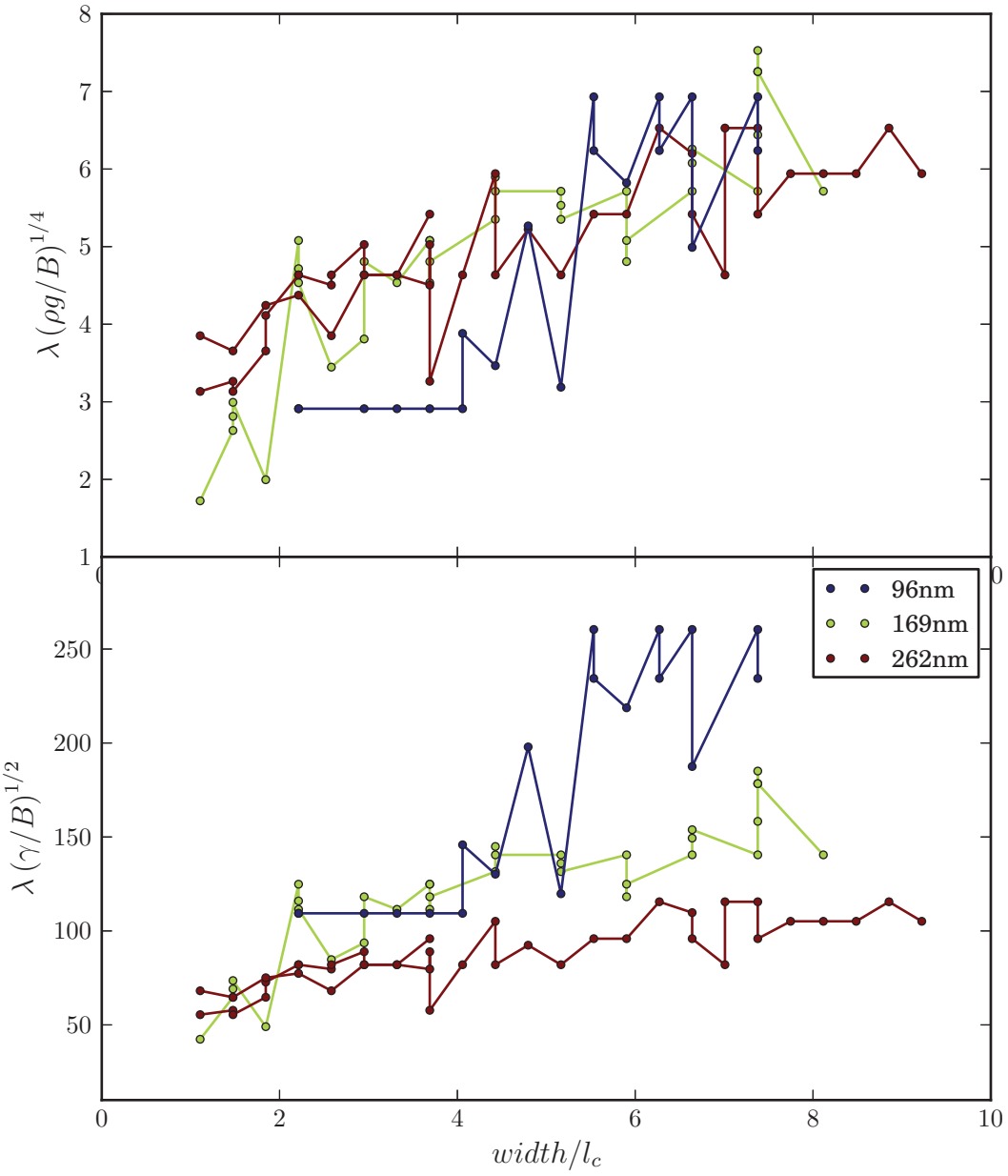

Figure C.2. Wrinkle wavelengths for uniaxially compressed sheets of varying widths and thicknesses. The top panel y-axis is scaled by the predicted bulk wavelength, predicted edge wavelength in the bottom panel. Widths are scaled by the capillary length. Data collapse is better for the bulk scaling above, but improves for the edge scaling at small widths.

APPENDIX D

TWO OTHER SHAPES

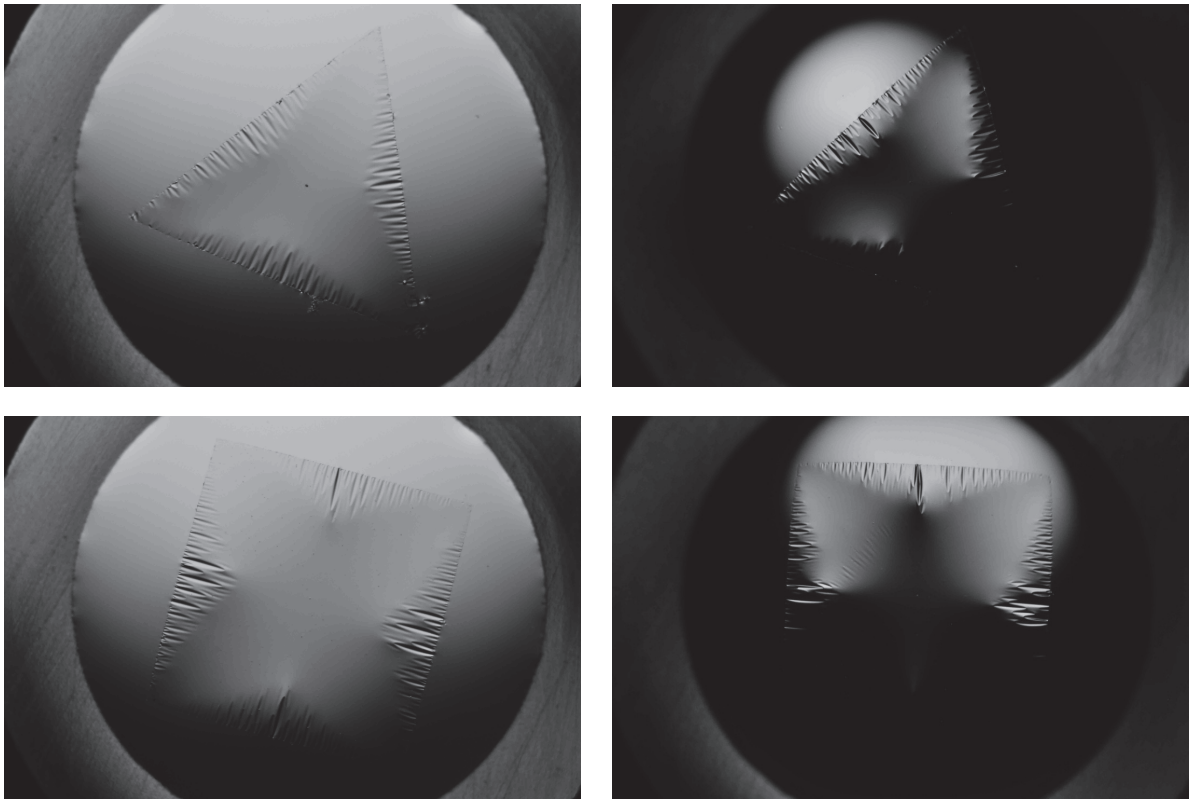

Figure D.1. Wrinkles and crumples in a triangular and a square sheet, just for kicks.

BIBLIOGRAPHY

[1] Abramoff, M. D., Magelhaes, P. J., and Ram, S. J. Image processing with ImageJ. *Biophotonics Int 11*, 7 (2004), 36–42.

[2] Ben Amar, M., and Pomeau, Y. Crumpled paper. *Proceedings of the Royal Society of London. Series A: Mathematical, Physical and Engineering Sciences 453*, 1959 (1997), 729–755.

[3] Brau, Fabien, Vandeparre, Hughes, Sabbah, Abbas, Poulard, Christophe- and Boudaoud, Arezki, and Damman, Pascal. Multiple-length-scale elastic instability mimics parametric resonance of nonlinear oscillators. *Nat Phys 7* (2011).

[4] Cambou, Dominique. image.

[5] Cerda, E., and Mahadevan, L. Conical surfaces and crescent singularities in crumpled sheets. *Phys. Rev. Lett. 80* (Mar 1998), 2358–2361.

[6] Cerda, E., and Mahadevan, L. Geometry and physics of wrinkling. *Phys. Rev. Lett. 90* (Feb 2003), 074302.

[7] Das, Siddhartha, Marchand, Antonin, Andreotti, Bruno, and Snoeijer, Jacco H. Elastic deformation due to tangential capillary forces. *Physics of Fluids 23*, 7 (2011), 072006.

[8] Davidovitch, Benny, Schroll, Robert D., Vella, Dominic, Adda-Bedia, Mokhtar, and Cerda, Enrique A. Prototypical model for tensional wrinkling in thin sheets. *Proceedings of the National Academy of Sciences 108*, 45 (2011), 18227–18232.

[9] De Gennes, Pierre-Gilles, Brochard-Wyart, Franoise, and Qur, David. *Capillarity and Wetting Phenomena: Drops, Bubbles, Pearls, Waves*. Springer, 2004.

[10] Du, Kan, Glogowski, Elizabeth, Emrick, Todd, Russell, Thomas P., and Dinsmore, Anthony D. Adsorption energy of nano- and microparticles at liquidliquid interfaces. *Langmuir 26*, 15 (2010), 12518–12522.

[11] Efimenko, Kirill, Rackaitis, Mindaugas, Manias, Evangelos, Vaziri, Ashkan, Mahadevan, L., and Genzer, Jan. Nested self-similar wrinkling patterns in skins. *Nat Mater 4*, 4 (2005), 293–297.

[12] Geminard, J.-C., Bernal, R., and Melo, F. Wrinkle formations in axi-symmetrically stretched membranes. *The European Physical Journal E: Soft Matter and Biological Physics 15* (2004), 117–126. 10.1140/epje/i2004-10041-1.

[13] Hall, David B., Underhill, Patrick, and Torkelson, John M. Spin coating of thin and ultrathin polymer films. *Polymer Engineering and Science 38*, 12 (1998), 2039–2045.

[14] Hinsch, K. Holographic study of liquid surface deformations produced by floating particles. *Journal of Colloid and Interface Science 92*, 1 (1983), 243 – 255.

[15] Huang, Jiangshui, Davidovitch, Benny, Santangelo, Christian D., Russell, Thomas P., and Menon, Narayanan. Smooth cascade of wrinkles at the edge of a floating elastic film. *Phys. Rev. Lett. 105* (Jul 2010), 038302.

[16] Huang, Jiangshui, Juszkiewicz, Megan, de Jeu, Wim H., Cerda, Enrique, Emrick, Todd, Menon, Narayanan, and Russell, Thomas P. Capillary wrinkling of floating thin polymer films. *Science 317*, 5838 (2007), 650–653.

[17] Hure, Jérémy, Roman, Benoˆ, and Bico, José. Wrapping an adhesive sphere with an elastic sheet. *Phys. Rev. Lett. 106* (Apr 2011), 174301.

[18] Hure, Jérémy, Roman, Benoˆ, and Bico, José. Stamping and wrinkling of elastic plates. *Phys. Rev. Lett. 109* (Aug 2012), 054302.

[19] Irvine, William T. M., Vitelli, Vincenzo, and Chaikin, Paul M. Pleats in crystals on curved surfaces. *Nature 468*, 7326 (2010), 947–951.

[20] Jerison, Elizabeth R., Xu, Ye, Wilen, Larry A., and Dufresne, Eric R. Deformation of an elastic substrate by a three-phase contact line. *Phys. Rev. Lett. 106* (May 2011), 186103.

[21] Kaz, David M., McGorty, Ryan, Mani, Madhav, Brenner, Michael P., and Manoharan, Vinothan N. Physical ageing of the contact line on colloidal particles at liquid interfaces. *Nat Mater 11*, 2 (2012), 138–142.

[22] King, Hunter, Schroll, Robert D., Davidovitch, Benny, and Menon, Narayanan. Elastic sheet on a liquid drop reveals wrinkling and crumpling as distinct symmetry-breaking instabilities. *Proceedings of the National Academy of Sciences 109*, 25 (2012), 9716–9720.

[23] Kralchevsky, P. A., Ivanov, I. B., Ananthapadmanabhan, K. P., and Lips, A. On the thermodynamics of particle-stabilized emulsions: curvature effects and catastrophic phase inversion. *Langmuir 21*, 1 (2005), 50–63. PMID: 15620284.

[24] Landau, L. D., and Lifshitz, E. M. *Theory of elasticity / by L. D. Landau and E. M. Lifshitz ; translated from the Russian by J. B. Sykes and W. H. Reid.* Pergamon, London :, 1959.

[25] Lobkovsky, Alexander E., and Witten, T. A. Properties of ridges in elastic membranes. *Phys. Rev. E* (1996).

[26] Mansfield, Eric Harold. *The bending and stretching of plates / E.H. Mansfield*, 2nd ed. ed. Cambridge University Press, Cambridge [England] ; New York :, 1989.

[27] Planchette, Carole, Lorenceau, Elise, and Biance, Anne-Laure. Surface wave on a particle raft. *Soft Matter 8* (2012), 2444–2451.

[28] Pocivavsek, Luka, Dellsy, Robert, Kern, Andrew, Johnson, Sebastian, Lin, Binhua, Lee, Ka Yee C., and Cerda, Enrique. Stress and fold localization in thin elastic membranes. *Science 320*, 5878 (2008), 912–916.

[29] Pressley, A.N. *Elementary Differential Geometry*. Springer Undergraduate Mathematics Series. Springer, 2010.

[30] Py, Charlotte, Reverdy, Paul, Doppler, Lionel, Bico, José, Roman, Benoˆ, and Baroud, Charles N. Capillary origami: Spontaneous wrapping of a droplet with an elastic sheet. *Phys. Rev. Lett. 98* (Apr 2007), 156103.

[31] 2005.

[32] Scharr, Hanno. *Optimale Operatoren in der Digitalen Bildverarbeitung*. PhD thesis, Universitt Heidelberg, 2000.

[33] Schroll, Robert D., Katifori, Eleni, and Davidovitch, Benny. Elastic building blocks for confined sheets. *Phys. Rev. Lett. 106* (Feb 2011), 074301.

[34] Shanahan, M E R. The spreading dynamics of a liquid drop on a viscoelastic solid. *Journal of Physics D: Applied Physics 21*, 6 (1988), 981.

[35] Stein, M., Hedgepeth, J.M., Aeronautics, United States. National, and Administration, Space. *Analysis of partly wrinkled membranes*. NASA technical note. National Aeronautics and Space Administration, 1961.

[36] Timoshenko, S., and Goodier, J.N. *Theory of Elasticity*. McGraw-Hill, New York, 1970.

[37] Vella, D., Adda-Bedia, M., and Cerda, E. Capillary wrinkling of elastic membranes. *Soft Matter 6* (2010), 5778–5782.

[38] Vella, D., Aussillous, P., and Mahadevan, L. Elasticity of an interfacial particle raft. *EPL (Europhysics Letters) 68*, 2 (2004), 212.

[39] Vella, Dominic, and Mahadevan, L. The "cheerios effect". *American Journal of Physics 73*, 9 (2005), 817–825.

[40] Witten, T. A. Stress focusing in elastic sheets. *Rev. Mod. Phys. 79* (Apr 2007), 643–675.

[41] Yao, Zhenwei, Bowick, Mark, and Ma, Xu. Planar sheets meet negative curvature liquid interfaces. *arxiv: cond-mat.soft1204.5237* (2012).

[42] Zhang, Xiaohua, Yager, Kevin G., Kang, Shuhui, Fredin, Nathaniel J., Akgun, Bulent, Satija, Sushil, Douglas, Jack F., Karim, Alamgir, and Jones, Ronald L. Solvent retention in thin spin-coated polystyrene and poly(methyl methacrylate) homopolymer films studied by neutron reflectometry. *Macromolecules 43*, 2 (2010), 1117–1123.